

University of Louisville

ThinkIR: The University of Louisville's Institutional Repository

Electronic Theses and Dissertations

5-2005

Design and development of a MEMS-based capacitive bending strain sensor and a biocompatible housing for a telemetric strain monitoring system.

Julia Marie Weyer Aebersold 1969-
University of Louisville

Follow this and additional works at: <https://ir.library.louisville.edu/etd>



Part of the [Mechanical Engineering Commons](#)

Recommended Citation

Aebersold, Julia Marie Weyer 1969-, "Design and development of a MEMS-based capacitive bending strain sensor and a biocompatible housing for a telemetric strain monitoring system." (2005). *Electronic Theses and Dissertations*. Paper 16.

<https://doi.org/10.18297/etd/16>

This Doctoral Dissertation is brought to you for free and open access by ThinkIR: The University of Louisville's Institutional Repository. It has been accepted for inclusion in Electronic Theses and Dissertations by an authorized administrator of ThinkIR: The University of Louisville's Institutional Repository. This title appears here courtesy of the author, who has retained all other copyrights. For more information, please contact thinkir@louisville.edu.

DESIGN AND DEVELOPMENT OF A MEMS-BASED CAPACITIVE BENDING
STRAIN SENSOR AND A BIOCOMPATIBLE HOUSING FOR A TELEMETRIC
STRAIN MONITORING SYSTEM

By
Julia Marie Weyer Aebersold
B.S.E.S, University of Louisville, 1992
M. Eng., University of Louisville, 1994

A Dissertation
Submitted to the Faculty of the
Graduate School of the University of Louisville
in Partial Fulfillment of the Requirements
for the Degree of

Doctor of Philosophy

Department of Mechanical Engineering
Speed School of Engineering
University of Louisville
May 2005

DESIGN AND DEVELOPMENT OF A MEMS-BASED CAPACITIVE BENDING
STRAIN SENSOR AND A BIOCOMPATIBLE HOUSING FOR A TELEMETRIC
STRAIN MONITORING SYSTEM

By

Julia Marie Weyer Aebersold
B.S.E.S., University of Louisville, 1992
M.Eng., University of Louisville, 1994

A Dissertation Approved on

April 12, 2005

By the following Dissertation Committee:

Dissertation Director – William P. Hnat

Kevin M. Walsh

Michael J. Voor

John F. Naber

Robert S. Keynton

DEDICATION

This dissertation is dedicated to my son

Alexander Michael Aebersold

who has given me the courage and conviction to pursue my dreams.

ACKNOWLEDGEMENTS

The accomplishment of this project has not been my effort alone. There are many others that have been pivotal in my success. I would like to express my appreciation and gratitude to my advisor, Dr. William Hnat, for his input and guidance during this time of achievement. In addition I would like to extend appreciation to the members of my committee Dr. Kevin Walsh, Dr. Michael Voor, Dr. John Naber and Dr. Robert Keynton for their guidance and support. Their continuous help and answers to my endless questions have made this project successful.

I would also like to express thanks to the people who instructed me on various pieces of equipment, gave guiding input and expertise or performed tasks that I could not complete myself. They are Ji-Tzuoh Lin, Doug Jackson, Mark Crain, Michael Martin, Rekha Pai, Josph Lake, Tommy Roussell, Usha Gowrishetty and John Jones. In addition I would like to thank the Mechanical Engineering Department of the Speed School of Engineering at the University of Louisville, especially Dr. Glen Prater, Sue Jones and Diane Jenne.

My family has also been extremely supportive, patient and understanding while I transitioned from an industrial career to academia. In particular, my son was an inspiration for me since he was born. I wished the best of all opportunities for him and realized that I should strive for the same aspirations. Also, many thanks go to my

husband, mother, father, sister, in-laws and extended family for their continuous support and encouragement. Financial support from the National Science Foundation grant #0097521 is also gratefully acknowledged.

Finally, I wish to thank Christ for guiding me to abide His will. His gentle way has always guided my path. It was only for me to listen.

ABSTRACT

DESIGN AND DEVELOPMENT OF A MEMS-BASED CAPACITIVE BENDING STRAIN SENSOR AND A BIOCOMPATIBLE HOUSING FOR A TELEMETRIC STRAIN MONITORING SYSTEM

Julia M. W. Aebersold

May 14, 2005

Lumbar arthrodesis or spinal fusion is usually performed to relieve back pain and regain functionality from ruptured discs, disc degenerative disease, trauma or scoliosis. Metal rods are often fixed to the spine with screws or hooks, while fusion develops on the affected vertebrae. Fusion is determined by visual examination of radiographic images (X-ray), computed tomography (CT) scans or magnetic resonance imaging (MRI), yet these inspection procedures are subjective methods of review. They do not objectively confirm the presence of spinal fusion, which can lead to exploratory surgery to determine if fusion has occurred.

Therefore, a need has arisen to develop an objective method that will offer unbiased information for the determination of fusion. Discussed herein is a housing and sensor designed to be used in conjunction with telemetric circuitry that will attach to the spinal instrumentation rods. The housing will transmit strain to an internal capacitive MEMS-based sensor that will relay strain magnitudes via telemetry. Observed reductions of bending strain will indicate a successful fusion. These objective assessments will

reduce the incidence of costly exploratory surgeries where fusion is in question.

The housing design was fabricated using Polyetheretherketone (PEEK) material, which was selected for its physical properties and its ability to be implanted for long durations. The housing was tested under cyclical, static and maximum strain transfer loading configurations in the Material Testing System (MTS). Results from these tests demonstrated that the housing transferred 102% of the bending strain and successfully met the design criteria.

Additionally, a MEMS-based sensor was developed to change capacitance with detected alterations in bending strain transmitted through the housing. Sensors were fabricated using microfabrication techniques and highly doped boron silicon wafers to create a transverse comb drive or an interdigitated finger array. The sensor was tested using similar methods that were used for the housing. Results from cyclical testing demonstrated the sensor's response needed to be increased 50% and it did not exhibit any capacitance drift.

TABLE OF CONTENTS

ACKNOWLEDGMENTS.....	iv
ABSTRACT.....	vi
LIST OF TABLES.....	xii
LIST OF FIGURES.....	xiii
1.0 INTRODUCTION.....	1
1.1 Spinal Fusion Background.....	3
1.2 Justification.....	5
1.2.1 Using Bending Strain to Objectively Detect the Presence of Spinal Fusion	6
1.2.2 Existing Spinal Fusion Detection Systems.....	9
1.2.3 Existing Implantable Strain Monitoring Systems.....	10
1.3 Strain Monitoring System Requirements.....	14
2.0 HOUSING.....	16
2.1 Housing Literature Search.....	17
2.2 Preliminary Housing Approach.....	21
2.2.1 Preliminary Housing Materials and Methods.....	21
2.2.1.1 Solid Edge Models and Rapid Prototyped Housings...22	
2.2.1.2 MTS Testing Configurations.....	26
2.2.1.3 Housing Material Selection	30
2.2.1.4 Housing Material Testing.....	31

2.2.2	Preliminary Housing Results.....	32
2.2.2.1	MTS Testing Results for Rapid Prototyped Models.....	32
2.2.2.2	MTS Testing Results for Preliminary Housings of Various Materials.....	36
2.2.3	Preliminary Housing Discussion.....	38
2.2.3.1	Discussion of the Rapid Prototyped Models.....	38
2.2.3.2	Discussion of the Preliminary Housings of Various Materials.....	40
2.2.4	Conclusions for Preliminary Housings.....	41
2.3	Final Housing Approach.....	41
2.3.1	Materials and Methods.....	42
2.3.1.1	ABAQUS Finite Element Modeling of the Final Housing.....	44
2.3.1.2	Fabrication, Fixturing and MTS Testing of the Final Housing.....	49
2.3.1.3	Water Tank Testing of the Final Housing.....	57
2.3.1.4	Cadaver Testing of the Final Housing.....	60
2.3.2	Results.....	61
2.3.2.1	ABAQUS Finite Element Modeling Results.....	62
2.3.2.2	MTS Testing Results of the Final Housing.....	67
2.3.2.3	Water Tank Testing Results of the Final Housing.....	69
2.3.2.3	Cadaver Testing Results of the Final Housing.....	71
2.3.3	Discussion.....	73
2.3.3.1	ABAQUS Finite Element Model Discussion of the Final Housing.....	73

	2.3.3.2 MTS Final Housing Design Discussion.....	75
	2.3.3.3 Water Tank Testing Discussion.....	76
	2.3.3.4 Cadaver Testing Discussion.....	76
3.0	MEMS-BASED CAPACITIVE BENDING STRAIN SENSOR.....	78
	3.1 Sensor Literature Search.....	79
	3.2 Preliminary Sensor Approach.....	80
	3.2.1 Preliminary Sensor Materials and Methods.....	80
	3.2.1.1 Sensor Change of Length Calculations and Capacitance Relationships.....	80
	3.2.1.2 Preliminary Sensor Designs.....	83
	3.2.1.2.1 CoventorWare Finite Element Modeling of Preliminary Sensors.....	85
	3.2.1.2.2 ABAQUS Finite Element Modeling of Preliminary Sensors.....	91
	3.2.1.3 Fabrication of Preliminary Sensors.....	95
	3.2.2 Preliminary Sensor Results.....	102
	3.2.3 Discussion of Preliminary Sensors.....	104
	3.2.4 Conclusions for Preliminary Sensors.....	104
	3.3 Final Sensor Approach.....	106
	3.3.1 Materials and Methods.....	107
	3.3.1.1 ABAQUS Finite Element Modeling of the Final Sensor.....	109
	3.3.1.2 Fabrication of the Final Sensor.....	115
	3.3.1.3 MTS Testing of the Final Sensor.....	120
	3.3.2 Results.....	127

3.3.2.1	ABAQUS Finite Element Modeling Results of the Final Sensor.....	127
3.3.2.2	MTS Testing Results of the Final Sensor.....	130
3.3.3	Discussion.....	144
3.3.3.1	Discussion of the ABAQUS Finite Element Modeling of the Final Sensor.....	145
3.3.3.2	Discussion of the MTS Testing Results of the Final Sensor.....	146
4.0	CONCLUSIONS AND RECCOMENDATIONS.....	149
5.0	REFERENCES.....	152
6.0	CURRICULUM VITAE.....	159

LIST OF TABLES

TABLE	PAGE
I. Percentage of strain transfer for each housing design modeled in ABAQUS.....	63
II. Strain transfer percentages from different levels of bending strain at 20 MPa of clamping pressure.....	67
III. Information collected from each of the ABAQUS models.....	129
IV. Initial and final conductance values from each of the sensors.....	139
V. Analytical and ABAQUS modeling results of Sensor-96.....	146

LIST OF FIGURES

FIGURE	PAGE
1. Illustration of harvested bone applied during spinal fusion surgery.....	4
2. Illustrations of spinal fusion instrumentation implemented on a demonstration model.....	5
3. Illustrations of implanted spinal fusion instrumentation	5
4. Graphical representation of the vertebrae and spinal fusion hardware as employed in a corpectomy model.....	7
5. Free body diagram of the forces and moments applied to the spinal rod due to loading of the vertebrae.....	8
6. Illustration of Southwest Research Institute's system to monitor spinal fusion....	9
7. Instrumented devices developed by Rohlmann.....	10
8. The instrumented device developed by Rohlmann implemented onto a spine demonstration model.....	11
9. The extensometer application developed by Perusek.....	12
10. This system was developed by Ledet to be implanted between the vertebral space of baboons.....	13
11. The instrumented femoral implant developed by Taylor.....	14
12. The BION™ muscular stimulation system used for patients who experience muscle or limb paralysis.....	17
13. An implantable telemetry device to measure intra-articular tibial forces.....	18
14. The AbioCor Implantable replacement heart system.....	19
15. The ferrite coupler from Pi Research.....	20

16. Front view of a housing designed to test a locking mechanism.....	23
17. Rear view of a housing designed to test a locking mechanism.....	23
18. This extensometer design was not shaded to demonstrate the thin outer shell to see if strain amplification could be attained on the surface of the housing.....	23
19. This sleeve tube design was used to determine if adequate strain transfer through the nylon, glass-reinforced material could be achieved.....	24
20. The hole in the side of the housing was to accommodate room for a foil strain gage to the inner surface.....	24
21. Housings from the rapid prototyping facility using nylon glass-reinforced material produced from the DTM Sinterstation 2000.....	25
22. Illustrations (a) and (b) show the top and bottom of the test rod 1 with housing design #1 affixed with hose clamps.....	26
23. Illustration (a) is test rod 2 with housing design #1 in the right and design #2 on the right and both affixed with safety wire. Illustration (b) has two examples of housing design #3 with the left housing affixed with safety wire and the right housing attached with hose clamps.....	27
24. MTS fixture to achieve continuous strain at the surface of the rod (a) MTS with a rod loaded in the test fixture (b) A graphic of the loads applied by the MTS and placement of the strain gages on the rod. (c) The moment diagram as a result of the four-point bending test fixture in the MTS.....	28
25. Wiring arrangement for the Wheatstone half-bridge.....	29
26. Illustration of the Delrin housing using the sleeve design and with a strain gage mounted the location where the strain sensor would reside.....	31
27. Housings fabricated using Lexan and PEEK.....	32
28. Graphical results of the two haves housing design with hose clamps.....	33
29. Graphical results of test rod 1 of strain versus load mounted to the bar with hose clamps corresponding to illustration 1.....	34
30. Graphical results of test rod 2 with strain versus load with the sleeve and extensometer housings designs mounted to the bar with safety wire.....	35
31. Results for the extensometer using two different clamping techniques.....	36

32. Graphical results of the Delrin housing.....	37
33. Graphical results of the PEEK and Polycarbonate materials compared to rod strain.....	37
34. Graphical results of the 30% Carbon Filled PEEK materials compared to rod strain.....	38
35. Illustrations of the Atlas Cable System manufactured by Medtronic Sofamor Danek. The spherical bearing head of the cable allows the end of the cable to pass thru it as seen in (b). The tool in this illustration allows the cable to be tightened around an object to a specified pressure.....	43
36. Initial housing designs with a (a) housing with a thin wall section next to the rod surface and a thin wire channel (b) housing with a thick wall section near the rod surface and a wide wire channel (c) extensometer design with a thin wall section that is elevated away from the rod surface.....	45
37. ABAQUS FEA model of the housing and rod.....	46
38. Loading of the bar in the ABAQUS model.....	47
39. Illustration of the meshed assembly.....	48
40. The housing manufactured from PEEK as one piece and with a single opening to accommodate clearance space for the spherical bearings of the Medtronic Sofamor Danek Atlas Cable System.....	49
41. Method of attaching the housing to the rod (a) The housing is snapped onto the rod and the cable is loaded in the tensioning tool. (b) The cable is applied to the cable guide of the housing and tightened to 50 lbs/in ² . (c) While the cable is held in tension the clamping device crimps the stem of the spherical bearing securing the cable in place. (d) The cable cutter cuts the excess cable. (e) The aforementioned steps are repeated on the second cable.....	50
42. The MTS fixture used to achieve continuous strain at the surface of the rod. (a) The rod in the MTS under loading. (b) Graphic of the loading applied by the MTS on the rod and placement of gages on the rod.....	51
43. The testing system with the rod loaded in the MTS.....	52
44. Oscilloscopes showing the strain gage signals and load data from the MTS.....	53
45. The front panel of the LabView program developed to collect data during housing testing.....	54

46. The diagram of the LabView virtual instrument used to collect data from the strain gages and MTS load cell	55
47. The diagram for the virtual instrument used to extract the maximum and minimum values from each cycle.....	56
48. Illustrations of the box cover for the telemetry system.....	57
49. An illustration of the strain monitoring system enclosed in the box cover.....	58
50. Illustrations of the (a) telemetry system mounted in the corpectomy model in the MTS and water. (b) A closer view of the same test fixture of the instrumented rod configured in the corpectomy model and MTS.....	59
51. The strain monitoring system secured in the pedicle screws placed in L2 and L5 vertebrae of the cadaver spine.....	60
52. ABAQUS longitudinal strain graphical results from the FEA model.....	62
53. Strain transfer values for each of the housing designs.....	63
54. Data revealing percentage strain levels across the longitudinal plane of the sensor surface showing the location of best amplification.....	64
55. Graphical data showing the optimal clamping pressure for the 0.5 mm shell housing design.....	65
56. Strain modeling results from ABAQUS for the housing clamped at 20 MPa.....	66
57. Strain modeling results from ABAQUS showing the percentage of strain transfer compared at different bending strain values.....	66
58. Manual MTS testing results from the bar before initiating cycle testing	67
59. Maximum strain values collected from each cycle during the MTS cycle test....	68
60. Static strain testing of the rod and housing	69
61. The calibration curve generated from cantilever bending of the telemetry system.....	70
62. Comparison of the foil strain gage measurements and converted frequency to strain values in the corpectomy model, while submerged in water tank.....	71
63. Cadaver testing showing longitudinal strain on both rods.....	72

64. Frequency data gathered from cadaver testing	69
65. A pictorial demonstrating the extensometer sensor surface undergoing longitudinal strain deformation. This deformation does not undergo bending strain or conform to the rod surface. The darkened area represents the cross-section of the upper half of the housing.....	74
66. Spinal rod undergoing bending.....	81
67. A parallel plate configuration	83
68. (a) Lever arm arrangement of the initial housing design. (b) Movement of the anchors and central lever arm, while undergoing bending strain.....	84
69. The displacement gradient of a model developed in CoventorWare utilizing change in overlapping area between plates.....	87
70. The mesh generated in CoventorWare for the second model using parabolic tetrahedrons.....	88
71. Magnitude of the displacement of the sensor after actuation in the (a) front and (b) isometric view.....	89
72. Results for each of the principal stress developed by manipulating movement of the anchors. (a) $\sigma_1 = 284.60$ MPa (b) $\sigma_2 = 89.60$ MPa (c) $\sigma_3 = 89.60$ MPa.....	90
73. Illustrations of the beam during loading with the left end constrained in all axial directions and a load couple applied to the right end of the beam (b) The resulting strain profile on the beam.....	92
74. A model developed in ABAQUS using (a) a spring to alleviate stress concentrations with the two anchor system. (b) Displacement of the same model.....	94
75. The second model developed in ABAQUS using (a) angled lever with the two anchor system. (b) Displacement of the same model.....	95
76. Photomasks created for processing the circular array of interdigitated fingers from the CoventorWare model. (a) The first mask was used to create stationary fingers etched from the bottom side of the wafer. (b) The second mask etched through the remaining wafer to create the final sensor with interdigitated fingers.....	97
77. The fabricated sensor from (a) an overall picture and (b) a detail photo of the interdigitated fingers (c) An illustration of the side of a finger demonstrating the etch profile from the DRIE process.....	99

78. An illustration of (a) the fabricated sensor with a (b) detailed view of the interdigitated fingers.....	101
79. Illustrations of material failure occurring in sensor 3.....	103
80. Illustration of a comb drive design with two independent anchors.....	107
81. Front view of the capacitive strain sensor actuated from the rod undergoing bending.....	108
82. FEA model illustrations from the ABAQUS FEA model before bending (a) Overall view of the sensor model attached to the rod. (b) Close up view of the end of the sensor demonstrating the fingers and anchor.....	110
83. Illustration of the meshed assembly from ABAQUS.....	111
84. Modeling results from ABAQUS (a) – (k) showing the maximum principal stress developed in each anchor design. Illustration (j) shows results from using a pad that was 500 μm tall rather than 300 μm considered for all other modeling results	115
85. Fabrication process of the capacitive bending strain sensor. (a) Oxidation (b) Wet etching the bottom of the wafer to form anchors (c) Anodic bonding glass pads to the anchors (d) Deep reactive ion etching the interdigitated fingers. (e) Application of the wire leads.....	118
86. Illustrations of the photomasks and the completed sensor (a) The first photomask was used to develop the anchors. (b) The second photomask formed the interdigitated fingers. (c) The completed sensor after fabrication.....	119
87. Four point bending in the (a) MTS fixture applying an equal strain magnitude across the surface of the beam. (b) Illustration of the loads applied by the MTS and placement of the sensors and strain gage on the bar.....	120
88. Illustration of the front panel for the LabView data collection program.....	122
89. Illustration of frame 1 from the LabView diagram used to collect data from the capacitance bending strain sensor and strain gages	123
90. Illustration of frame 2 from the LabView program used to collect data from the capacitance bending strain sensor and strain gages.....	124
91. Front panel of the LabView program that retrieved the maximum and minimum data values for each cycle.....	125

92. Diagram of the program used to retrieve the maximum and minimum values from each data cycle.....	126
93. Max principal stress of a single glass pad attached to the beam. Stress along the sidewall reduces from the beam to the top of the glass pad.....	128
94. Actuation of the sensor from the ABAQUS model Sensor-96 (a) transverse actuation of the model with a 10.6 μm final narrow gap (b) 12 μm vertical displacement of the sensor.....	130
95. A graphical illustration of the interdigitated fingers of the sensor (a) before bending strain is applied. (b) After bending strain is applied the spacing between the fingers has changed considerably. (c) & (d) Vertical actuation of the sensor.....	131
96. Graphical results of cyclical load testing for sensor 1.....	132
97. Graphical results of cyclical load testing for (a) sensor 2 and (b) sensor 3.....	133
98. Graphical results of cyclical load testing for sensor 4.....	134
99. Graphical results of static testing for (a) sensor 1 (b) and sensor 2	135
100. Graphical results of static testing for (a) sensor 3 and (b) sensor 4.....	136
101. Graphical results of the entire capacitance range for sensor 1.....	137
102. Graphical results of the entire capacitance range for (a) sensor 2 (c) and sensor 3.....	138
103. Graphical results of the entire capacitance range for sensor 4.....	139
104. Curve fit graphs generated for each sensor from the maximum capacitance test from the MTS. for sensor 1	140
105. Curve fit graphs generated for each sensor from the maximum capacitance test from the MTS. (a) sensor 2 (b) and sensor 3.....	141
106. Curve fit graphs generated for each sensor from the maximum capacitance test from the MTS. for sensor 4	142
107. Sensitivity for each sensor over the measured strain range.....	143
108. Sensitivity over the 0 to 1200 $\mu\epsilon$ range.....	143

1.0 INTRODUCTION

Back pain is the most frequent cause of limited activity in individuals who are less than forty-five years old and affects more than 10 million people [1]. It is also the second leading reason for physician visits in the United States. Approximately one percent of the population in the United States is chronically disabled because of low-back pain and an additional one percent is temporarily disabled. Each year, there are approximately 500,000 Workers' Compensation and personal-injury cases that process low-back pain claims. To help alleviate or remove the pain, lumbar arthrodesis or spinal fusion can be performed as a last resort when other therapies offer no solution. As a result of this technique's success more than 200,000 procedures are performed in the United States each year [1]. Additionally, the rate of lumbar arthrodesis procedures performed between 1979 and 1989 increased 200 percent [2].

After surgery orthopaedic surgeons evaluate fusion progress by using radiographic images (x-rays), computed tomography (CT) scans and magnetic resonance imaging (MRI). However, each of these methods are subjective and do not provide objective data that can conclusively determine the presence of fusion. Therefore, a specific need exists to objectively determine the presence of fusion.

It has been observed that bending strain induced on the implanted spinal rods will reduce with the occurrence of spinal fusion. Based upon this premise, an approach has

been developed to monitor bending strain in the instrumentation. Past efforts have been developed based upon these findings, but have not been successful primarily due to large size, sensitivity or installation procedures that are not conducive for the orthopaedic surgeon.

However, a system has been designed that is small in size and is easy to install onto pre-existing spinal fusion instrumentation. Primary components of the system include a microelectromechanical systems (MEMS) based capacitive bending strain sensor, telemetry circuitry and a housing. Herein are in depth descriptions of the housing and sensor designs including attempts that failed and the evolutionary changes implemented to achieve a successful design. The system measures bending strain and transmits the information wirelessly to assist orthopaedic surgeons with the assessment of lumbar arthrodesis if a reduction of bending strain is observed. A discontinuous change in bending strain would reveal either non-fusion or possible failure of the rods or pedicle screws and inform surgeons if additional surgery is required.

The function of the housing is to transmit strain developed on the rod to the internal strain sensor. Housing development was based upon design concepts that were retrieved from refereed journal publications and were implemented into three dimensional models. Rapid prototyped housings were developed from the models and tested in four-point bending to give results that were instrumental to determine which housing features would be used. Suitable materials were investigated for implantation and finite element models were constructed using the material characteristics. Once modeling was complete, the housing was fabricated and tested in four-point bending in a Material Testing System (MTS), which substantiated effectiveness of the housing design.

The housing was integrated with a cantilever bending strain sensor and radio frequency identification (RFID) telemetry circuitry to validate proof of concept.

The RFID telemetry system required the sensor to deliver a capacitive output that changed according to the observed strain on the rod. Geometry analysis of the rod undergoing bending directed sensor design to amplify the capacitive output of the sensor. Refereed publications gave input for a design that included a two anchors scheme that was modeled and fabricated, but testing results experienced material failure or no change of capacitance. A new sensor design was modeled using finite element analysis (FEA) that allowed independent movement of two anchors and was fabricated. The sensor was tested in four-point bending using the housing testing protocol.

Specifically, the intent of this project is to provide a system that will give objective strain information to orthopaedic surgeons. Observed reductions in bending strain may help determine the presence of spinal fusion and avoid costly exploratory surgeries where fusion is in question. In addition, the rates of fusion progression could be monitored to develop recovery regimens for patients of different backgrounds and circumstances for a more expeditious recovery. As a result, patients could return to normal activities more quickly, reduce lost work time, provide cost savings to employers and eliminate expensive follow-up CT scans.

1.1 Spinal Fusion Background

Lumbar arthrodesis or spinal fusion is a surgical procedure performed to immobilize affected lumbar vertebrae of the spine from deformity (i.e. scoliosis),

degenerative conditions (i.e. degenerative disc disease), trauma and tumors. During surgery, a bone graft, either synthetic or harvested from the patient's pelvis, is implanted between the spinal vertebrae or on the posterior side, as illustrated in Figure 1.

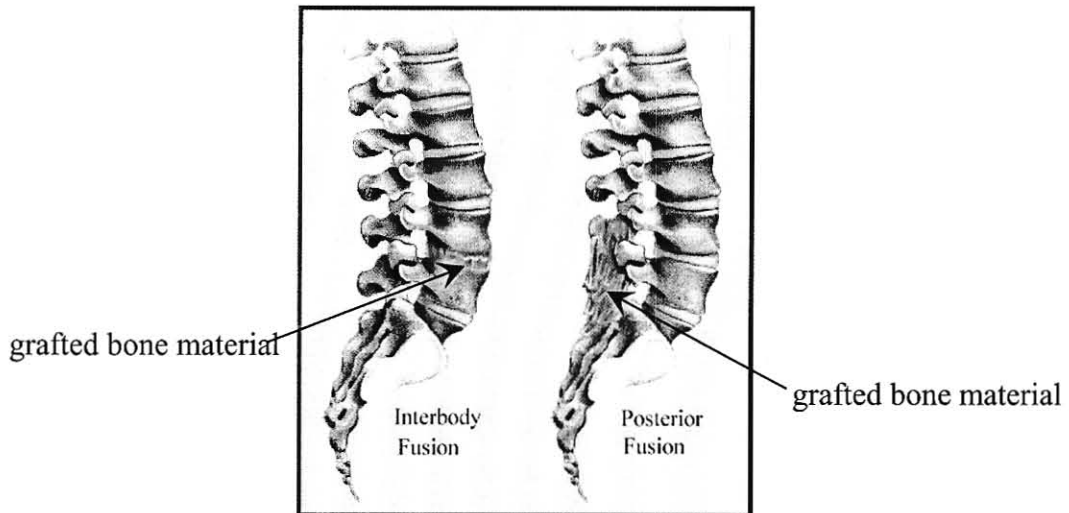


Figure 1. Illustration of harvested bone applied during spinal fusion surgery [3].

Over a period of six to twelve months, the grafted bone is expected to fuse with the adjacent vertebrae to form a collective bone segment. Spinal instrumentation is often implanted across the affected vertebrae provide stability and to promote fusion development. Instrumentation utilizes titanium, titanium-alloy, stainless steel, or non-metallic rods, hooks, braided cable, plates, screws and more recently threaded inter-body cages [4]. Figures 2 and 3 illustrate the rods and pedicle screws and their implementation into the spine. While this method restricts relative movement of the spine, it usually reduces or eliminates pain suffered by patients.

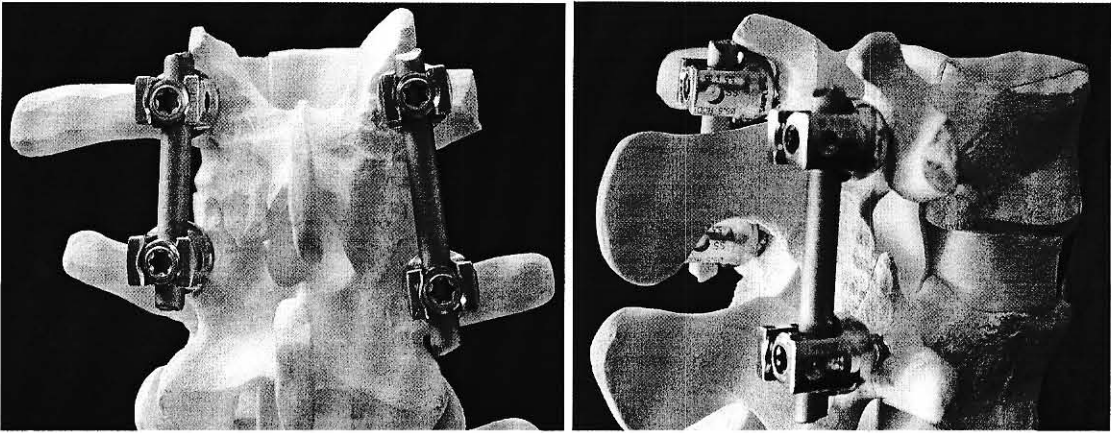


Figure 2. Illustrations of spinal fusion instrumentation implemented on a demonstration spine model.

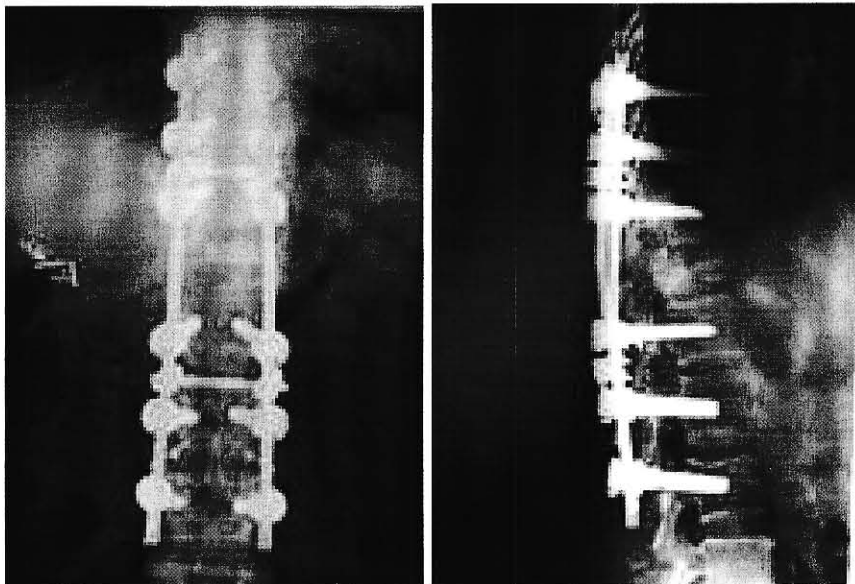


Figure 3. Radiographic images of implanted spinal instrumentation [4].

1.2 Justification

After surgery is performed, periodic evaluations are conducted using pain indices, patient surveys, radiographic images, computed tomography (CT) scans or magnetic resonance imaging (MRI). Relative motion across fusion levels are evaluated by

comparing standing flexion and extension from radiographic images. However, image obstructions often prevent clear determination of relative motion. Computed tomography (CT) provides greater detail than planar radiographic images; however, relative motion cannot be evaluated for the patient must remain in a fixed position during scanning. Magnetic resonance imaging (MRI) is primarily used to investigate the surrounding soft tissue and not to evaluate bony elements or fusion.

The primary problem with each of these methods of evaluation is they are subjective and do not provide objective data that can conclusively determine the presence of fusion. Nor can they offer supplemental information on the rates of fusion per different types of patients or if hardware failure has occurred. Therefore, development of a system that offers objective data is needed.

Previous research has offered a method of how to objectively monitor spinal fusion by means of observing bending strain generated in the implanted spinal rods. Systems have been developed to monitor strain of the spinal rods. However, functional issues of bulky size, sensitivity and laborious installation techniques have dissuaded use by orthopaedic surgeons.

1.2.1 Using Bending Strain to Objectively Detect the Presence of Spinal Fusion

To further understand the loading characteristics of the lumbar spine, Gibson [5] performed a discectomy on an excised spine from a cadaver. The spine was constrained and loaded in a Material Testing System (MTS) to simulate a 113.4 kg patient resulting in

rod bending strain values of approximately 1000 $\mu\epsilon$. Bending stress, $\sigma_{bending}$, and bending strain, $\epsilon_{bending}$, are defined as

$$\sigma_{bending} = \frac{Mc}{I} \quad (1)$$

and

$$\epsilon_{bending} = \frac{Mc}{EI} \quad (2)$$

where M is the calculated moment, c is the distance from the surface of the rod to the neutral axis, I is the area moment of inertia and E is Young's modulus (200 GPa) for 316L stainless steel. Calculations using 50.8 mm long pedicle screws, a 6.35 mm diameter rod and a patient of similar weight derived a bending strain of 1112 $\mu\epsilon$ on the surface of the rod and confirmed the data of Gibson. A corpectomy experimental model was also used to simulate spinal loading as shown in Figure 4. Figure 5 shows a free body diagram of the forces and bending moments applied to the spinal rods through the pedicle screws due to loading of the nylon blocks.

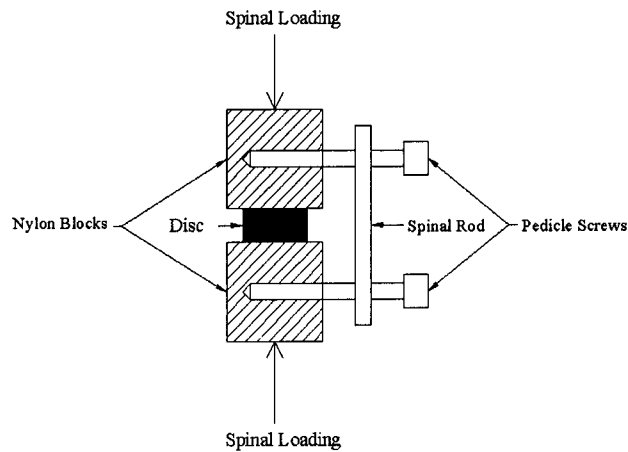


Figure 4. Graphical representation of the vertebrae and spinal fusion hardware as employed in a corpectomy model.

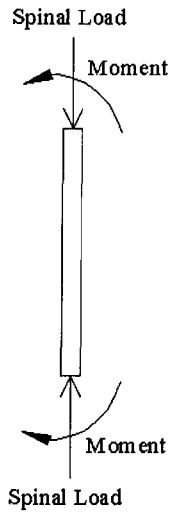


Figure 5. Free body diagram of the forces and moments applied to the spinal rod due to loading of the vertebrae.

Axial stress is defined by

$$\sigma_{axial} = \frac{P}{A} \quad (3)$$

and axial strain is characterized as

$$\varepsilon_{axial} = \frac{\sigma}{E} \quad (4)$$

where P is the applied vertical load or spinal load due to body weight as shown in Figure 5, and A is the cross-sectional area of the rod. Calculations of bending strain, equation 2, and axial strain, equation 4, for this application show that more than 90% of total strain developed is attributed to bending strain.

Kanayama et al. [6] observed that spinal rods in combination with pedicle screws showed a reduction of bending strain as the fusion mass developed. In addition, histological and radiographic evaluations did not indicate complete maturation of the fusion mass even though mechanical data demonstrated that the bony union had achieved sufficient biomechanical integrity. Therefore, a progressive transfer of loading from the

rods to the spine during the fusion process should result in decreased rod bending strain. Based upon this premise, changes in bending strain can offer insight and objective data for the presence of fusion and rates of fusion progression. In addition, sudden changes in bending strain can also help determine if hardware failure has occurred, such as pedicle screw head failure.

1.2.2 Existing Spinal Fusion Detection Systems

Since the advent of Kanayama's findings several attempts have been developed to observe bending strain to conclude the presence of fusion. Southwest Research Institute has developed a system that monitors relative motion between vertebrae. However, attachment of the sensor required additional drilling into the spinous process of the vertebrae and the system was relatively large for implantation [7], as shown in Figure 6. Additionally, the device is intended to be removed after one year due to long-term biocompatibility issues with the housing.

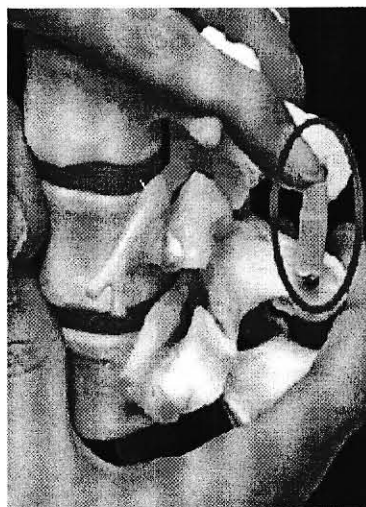


Figure 6. Illustration of Southwest Research Institute's system to monitor spinal fusion [8].

1.2.3 Existing Implantable Strain Monitoring Systems

Rohlmann successfully instrumented a spinal rod to measure forces and moments applied to the lumbar spine [9-17], as seen in Figures 7 and 8. However, the device is large and had to span several vertebrae. Rohlmann continues to use this device primarily for research purposes.

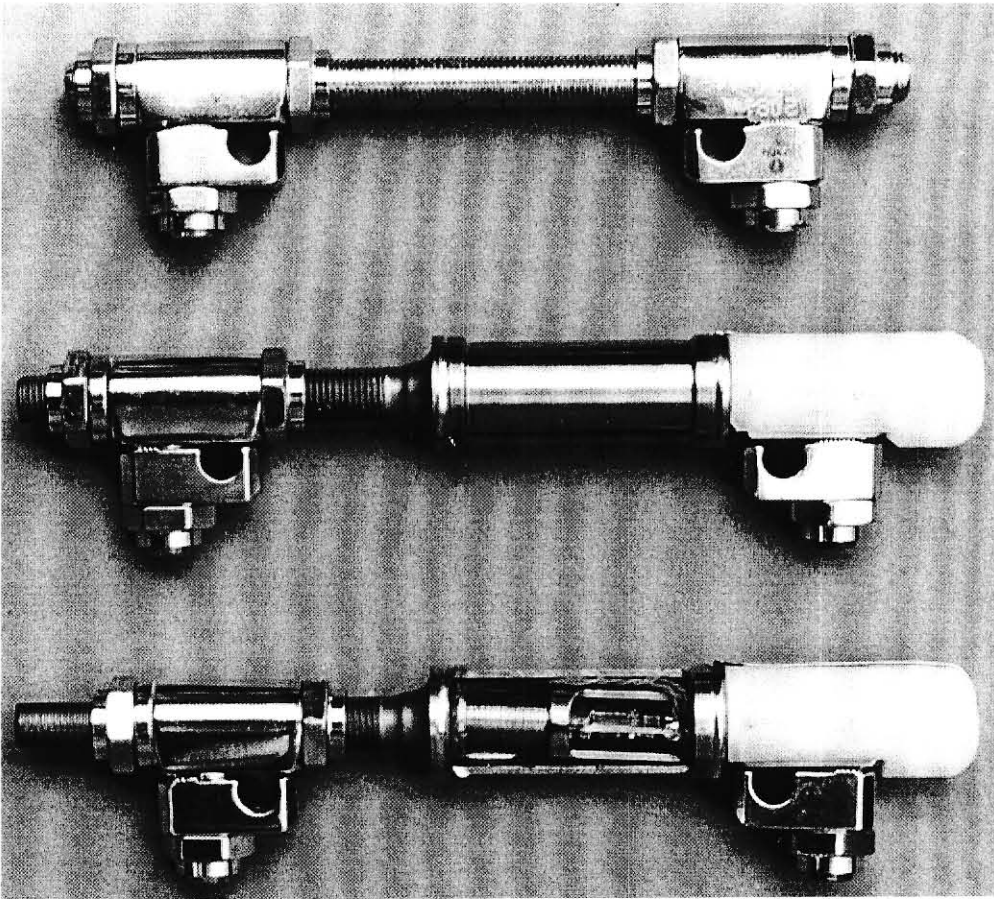


Figure 7. Instrumented devices developed by Rohlmann.

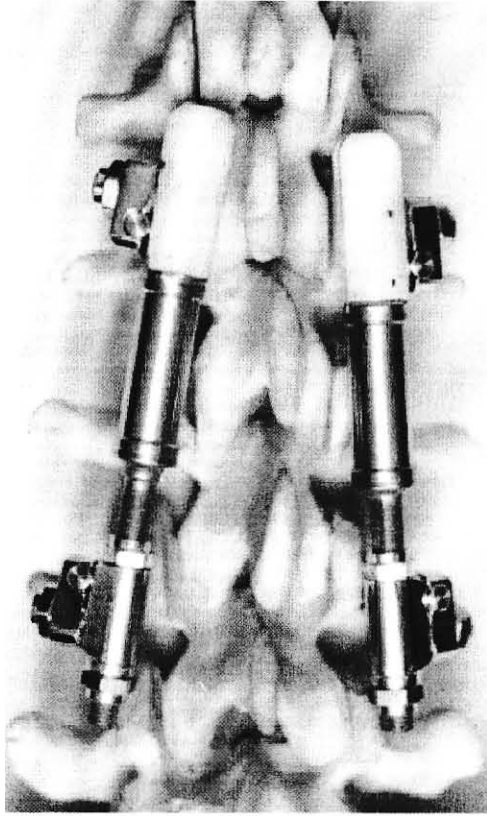


Figure 8 The instrumented device developed by Rohlmann implanted on a spine demonstration model.

Vamvanij [18] devised a conclusive test of spinal fusion from direct fusion exploration. However, the standard fusion evaluation method continues to be radiographic review. Lee and Harris [19, 20] developed a roentgen stereophotogrammetric technique using metallic markers for assessing cervical spine motion. However, this technique was not adequately sensitive to monitor the progression of spinal fusion. Perusek [21] developed an extensometer suitable for use in humans to measure bone strain, but the instrumentation was not suitable for long-term implantation as shown in Figure 9

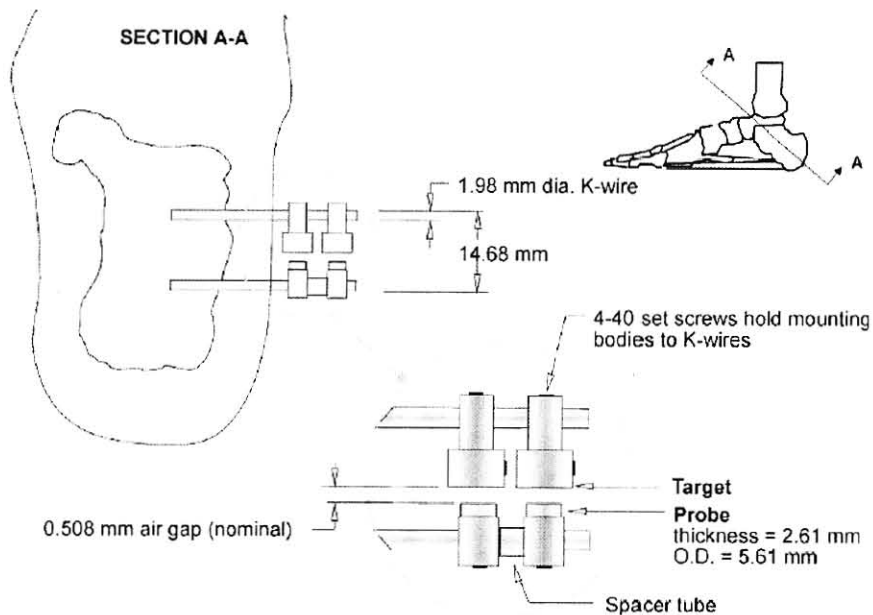


Figure 9 The extensometer application developed by Perusek.

Ledet [22, 23] developed a system that would perform real-time lumbar spine force measurements *in vivo*. However, the arrangement was designed to be implanted in the vertebral space between L4 and L5 of baboons. This application is not ready for clinical application due to the large size of the entire system, as seen in Figure 10. Strain gages are attached to the devices shown on the right side of the illustration, which are electrically connected to the circuit board. Additionally, the system would not be appropriate for patients where the vertebral disc was not intended to be removed.

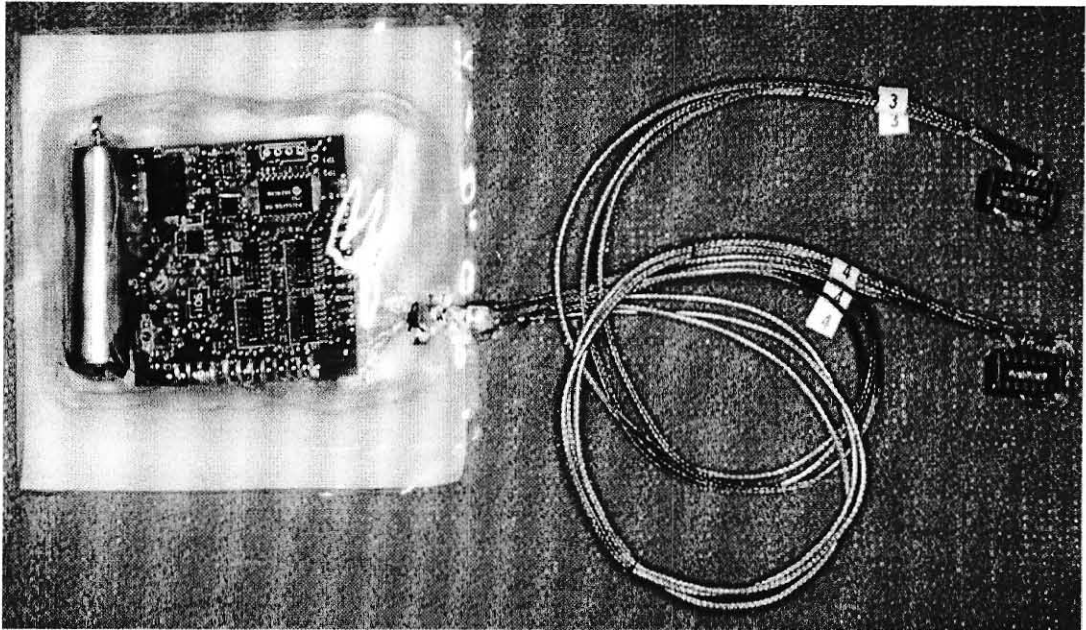


Figure 10 This system was developed by Ledet to be implanted between the vertebral spaces of baboons.

Taylor [24-26] developed a system that used strain gages and could be implanted for long periods of time, as seen in Figure 11. However, the system was primarily used for femoral replacements and the system was incorporated within the implant. It has been decided to not develop an instrumented proprietary fixation system due to required and extensive federal testing. It is anticipated that orthopaedic surgeons would also be reluctant to abandon currently used fixation systems. Finally, manual bending and manipulation of the rods are needed during surgery to replicate curvature of the patient's spine. This manipulation could break internal components of the system before implantation. Therefore, it was determined to attach the system to fixation systems readily used by orthopaedic surgeons. Finally, the system used internal batteries that are externally recharged and the use of batteries was not considered a viable option due to toxicity concerns.

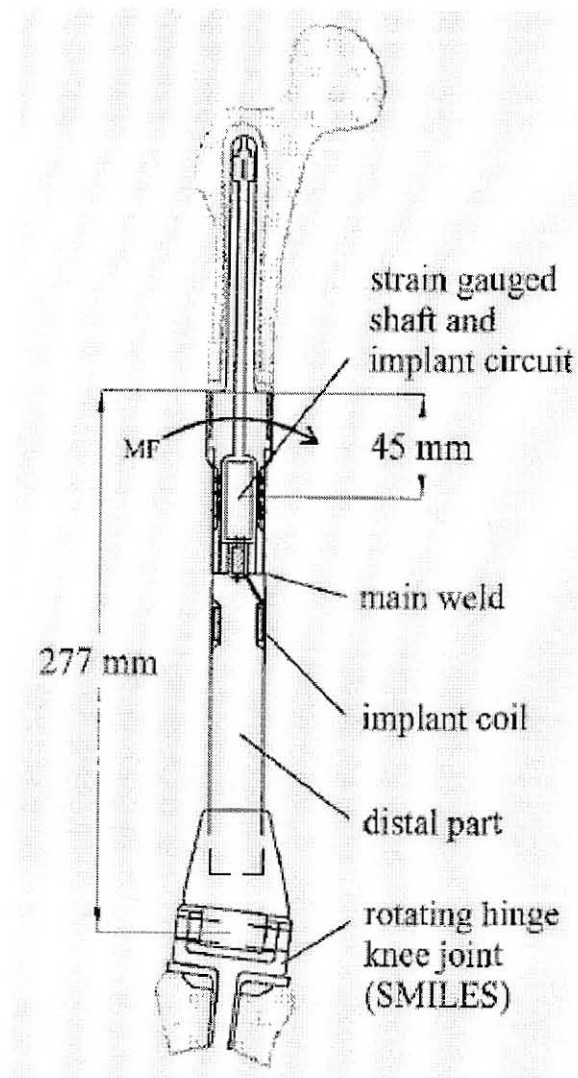


Figure 11. The instrumented femoral implant developed by Taylor.

1.3 Strain Monitoring System Requirements

From these investigated methods, a technique or system has not been developed that objectively evaluates the progression of spinal fusion. Therefore, a diagnostic system monitoring bending strain in the spinal rods can be developed to offer objective data to assist orthopaedic surgeons with the determination of spinal fusion, rates of fusion and

avoid costly exploratory surgeries when fusion is in doubt. Such a solution should meet the following requirements:

1. The housing of the system must be biocompatible for long term implantation or for the life of the patient. Typically, the system would not be removed after fusion was identified.
2. The system must be wireless, meaning there would be no electrical wires leading through topical or subcutaneous tissue.
3. The system must not be powered by a battery for the system will not be retrieved after implantation. Toxicity and functional longevity of a battery are overriding concerns, which eliminated the possibility of using it with the system.
4. The system must be small with dimensions no greater than 13 mm in length and diameter.
5. Quick and easy installation.
6. Function without failure for at least one year.

2.0 HOUSING

Primary components of the telemetric strain monitoring system are the MEMS-based capacitive bending strain sensor, telemetry circuitry and the housing. The purpose of the housing is to provide internal protection for the sensor and circuitry from the internal human environment and to prevent toxic contamination from the system to the patient. Alternative approaches of incorporating the sensor and circuitry in the spinal rods or pedicle screws were investigated, but were not pursued. Current fixation systems are diverse within the orthopaedic community. Developing a new proprietary system would require extensive research resources and delay potential utilization of the system. Therefore, a system that would quickly and simply attach to pre-existing fixation systems was designed.

Initial designs were developed using rapid prototyping technologies and tested in a Material Testing System (MTS) in four point bending. Finite element analysis (FEA) was implemented to explore reasons why the initial designs produced poor results. The final design was derived from the FEA model and tested in the MTS using a customized LabView program to collect strain data. Suitable housing material was also investigated that met requirements of long-term biocompatibility, a non-metallic material, low cost and acceptable strain transfer.

2.1 Housing Literature Search

One of the most important areas of sensor design is packaging and a sensor's packaging can represent 90% of material costs [27]. Housing designs for implantable devices varied considerably depending upon their application and location within the body. Biocompatibility, small size, low cost and the ability to be sterilized were some of the factors for housing design. Figure 12 demonstrates a tubular telemetry controlled muscle stimulator enclosed in glass for limb paralysis or spinal cord injury patients [28].

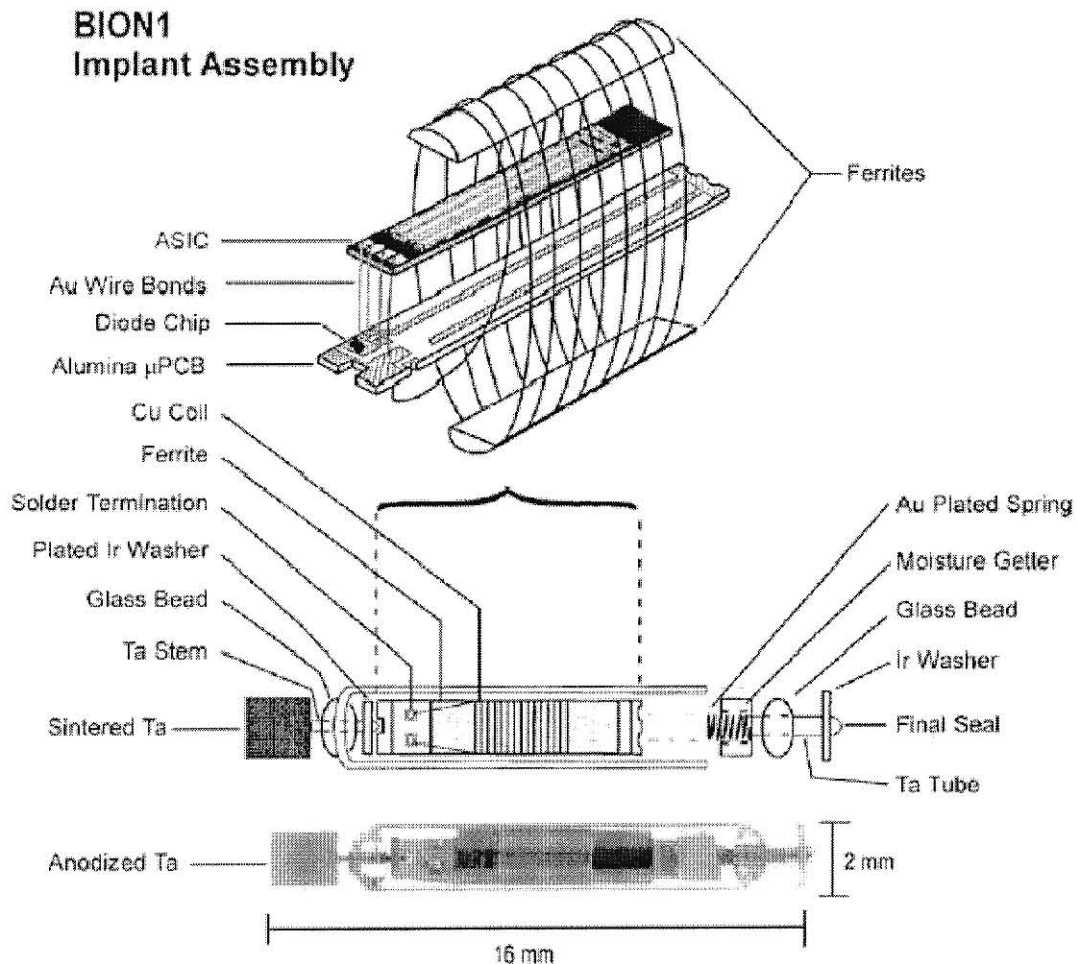


Figure 12. The BION™ muscular stimulation system used for patients who experience muscle or limb paralysis.

Figure 13 demonstrates another telemetry system that measures intra-articular tibial forces [29]. The T-shaped cross-section utilized different materials dependent upon the need of the implant and location.

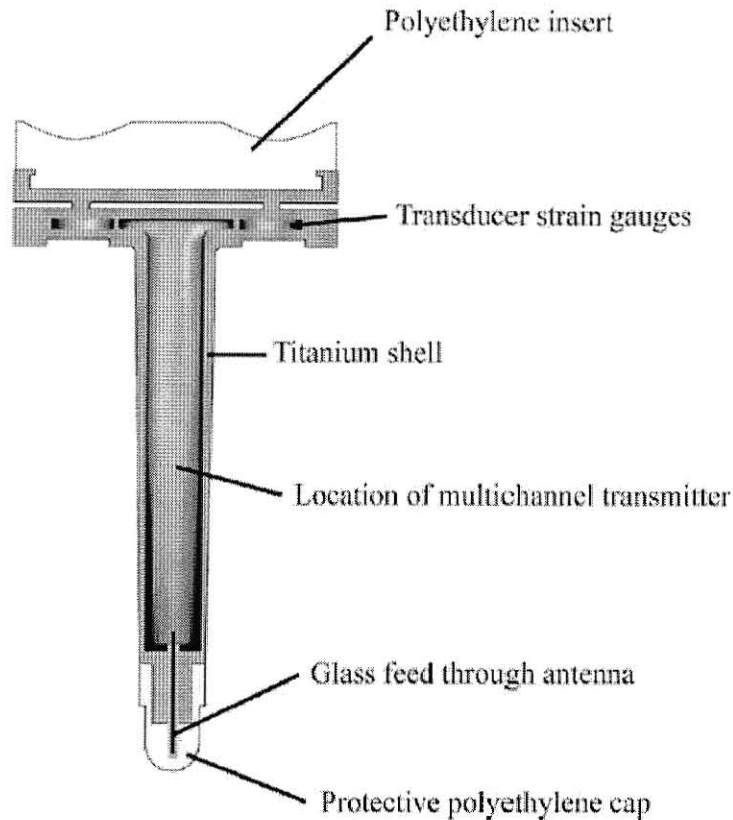


Figure 13. An implantable telemetry device to measure intra-articular tibial forces.

The need for encapsulation of devices, especially those that are constantly exposed to chemical environments, is one of their outstanding problems [30]. The majority of implant device failures resulted from breakdown of the encapsulating material. Biomedical polymers including epoxy resin, silicone, polyurethane, polyimide, etc. are used to seal or enclose electronics in the medical device field [31]. Encapsulating the entire system in epoxy was considered [32], however, this would possibly interfere with actuation of the sensor. Figure 14 demonstrates some of these materials in the

Abiocor replacement heart system along with packaging consideration given to the rechargeable batteries and the charging mechanism through the skin [33].

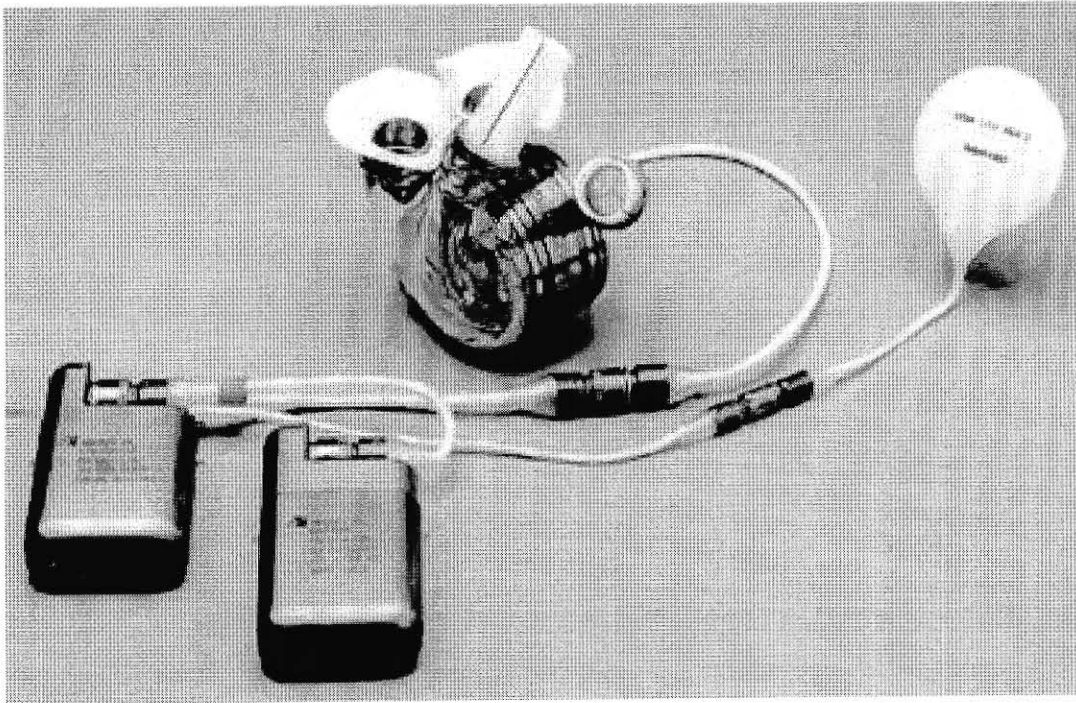


Figure 14. The AbioCor Implantable replacement heart system.

Pi Research produces ferrite couplers for automotive racing purposes [34]. The device clamps onto a circular cross-section, where Figure 15 shows the hinge and locking mechanism features of the coupler, which were of particular interest.

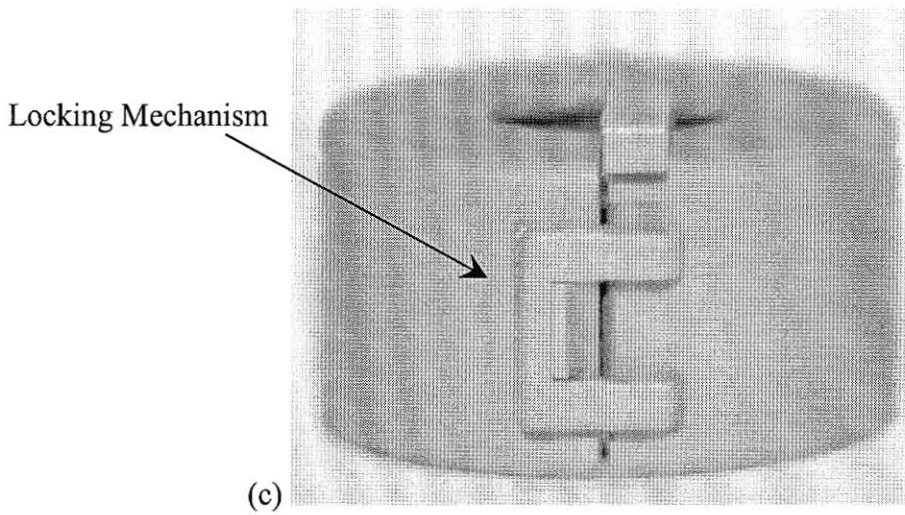
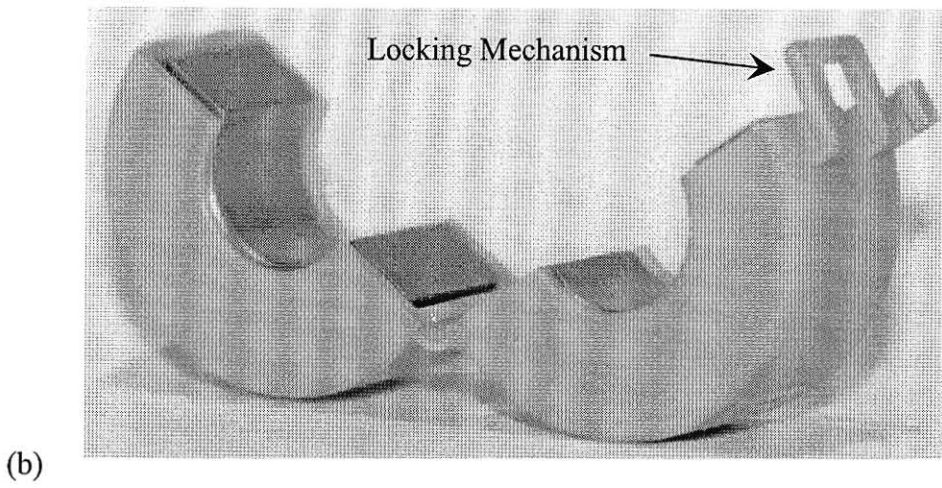
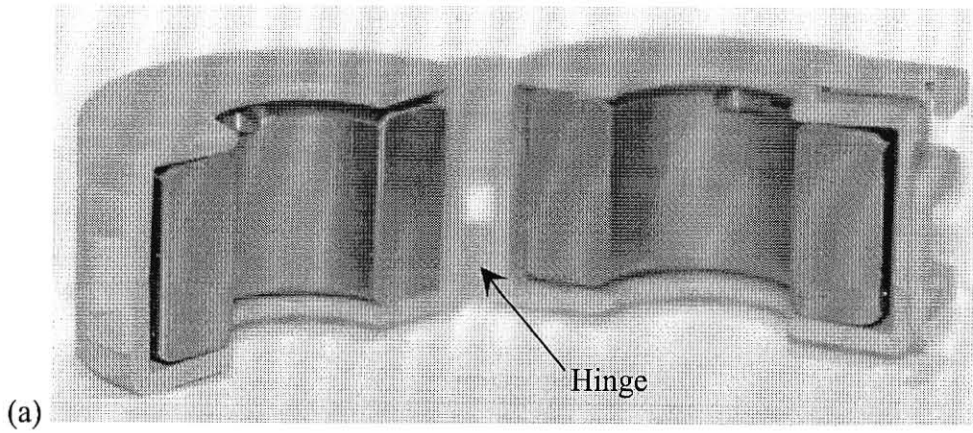


Figure 15. The ferrite coupler from Pi Research.

2.2 Preliminary Housing Approach

Design constraints for the housing were long-term implantation, ability to be sterilized without degradation, quick and simple attachment to the spinal rods, complete transfer of bending strain to the internal bending strain sensor and a small size with a length and diameter no larger than 13mm. Size constraints were mandated by the accommodating space between the L2 - L3, L3 - L4, L4 - L5 and L5-S1 vertebrae where lumbar spinal fusion surgery occurs.

A major design requirement for the housing was an expeditious and simplified installation into a small space. In this section, the development process of several preliminary housing designs using solid modeling software and rapid prototyping technologies is discussed. Housings were constructed from different polymers and tested to determine how their material properties affected strain transfer. The housings were mounted onto 316L stainless steel rods using different attachment methods including safety wire, hose clamps and cyanoacrylate adhesives. The prototypes were tested in four-point bending in a Material Testing System (MTS 810, Eden Prairie, MN) to replicate similar loading conditions of the lumbar spine. Strain data was recorded to monitor strain transfer from the rod through the housing.

2.2.1 Preliminary Housing Materials and Methods

To quickly test several initial designs, Solid Edge Software was employed to create three-dimensional solid models that were used to fabricate housings in the rapid

prototyping center. The fabricated housings were mounted to stainless steel rods by safety wire, hose clamps or cyanoacrylate adhesives. Strain gages were attached to the housing surface and rod to evaluate strain transfer.

Housing material choices were narrowed to a variety of polymers, which included ultra high molecular weight polyethylene (UHMWPE), polymethylmethacrylate (PMMA, Plexiglass®), Acetal Resin (Delrin®), polycarbonate (Lexan®), and polyetheretherketone (PEEK). Housings were fabricated from Delrin, Lexan and PEEK using common machining techniques and tested. Preferred characteristics of the housing were 100% strain transfer from the rod to the sensor surface of the housing.

2.2.1.1 Solid Edge Models and Rapid Prototyped Housings

Solid Edge (UGS, Huntsville, AL, ver. 12) was employed to develop solid models of the housing and avoid fabrication costs. Prototypes were produced with nylon glass-reinforced material in the DTM Sinterstation 2000 using the rapid prototyping facility. Resolution limitations were encountered with the sintering process for small characteristics, such as small fillets and radii, but these were manually cleaned using a Dremel tool. Figures 16 through 20 show examples of the Solid Edge models of the housings.

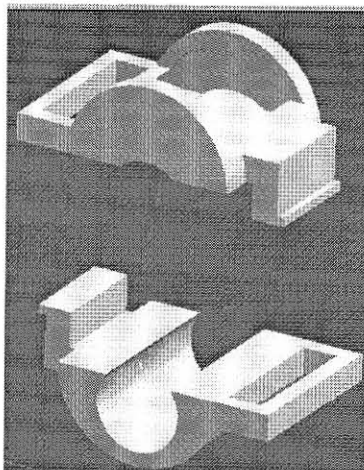


Figure 16. Front view the housing designed to test a locking mechanism.

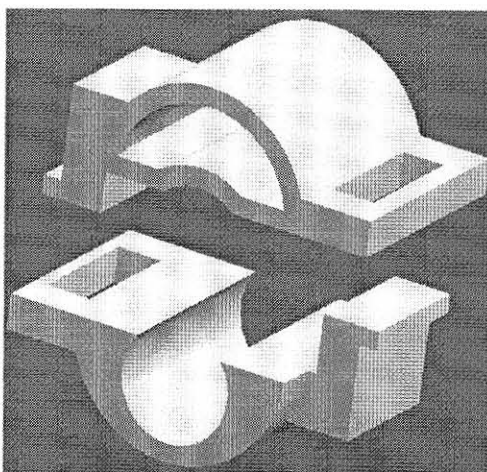


Figure 17. Rear view of a housing designed to test a locking mechanism.

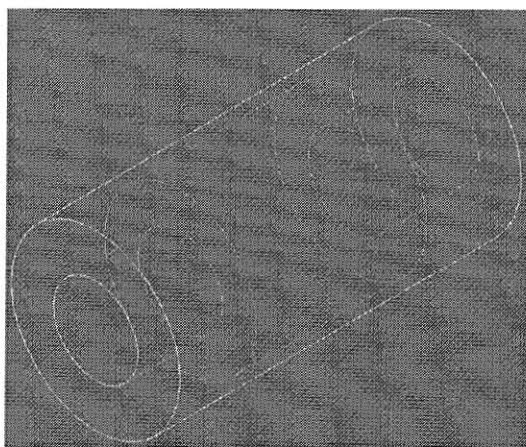


Figure 18. This extensometer design was not shaded to demonstrate the thin outer shell to see if strain amplification could be attained on the surface of the housing.

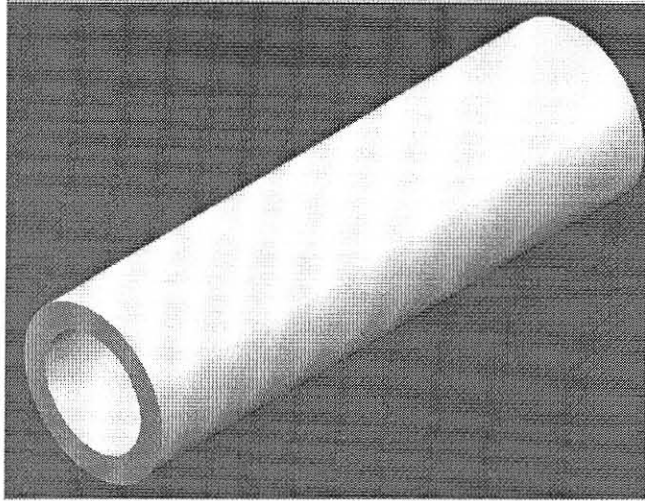


Figure 19. This sleeve tube design was used to determine if adequate strain transfer through the nylon, glass-reinforced material could be achieved.

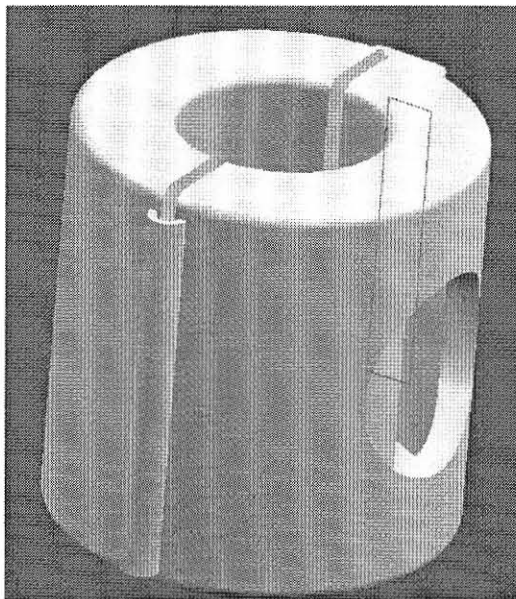


Figure 20. The hole in the side of the housing was to accommodate room for a foil strain gage to be applied to the inner surface.

The prototype housings, shown in Figure 21, are seen from left to right:

1. Housing with an offset rod hole, locking mechanism and side opening.
2. Housing with an offset rod hole, locking mechanism and a frontal opening.
3. Long Extensometer
4. Short Extensometer
5. Long Sleeve
6. Two halves

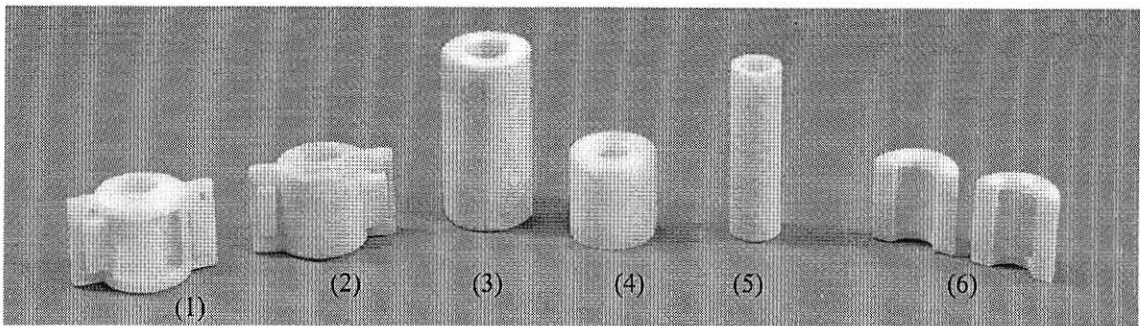


Figure 21. Housings from the rapid prototyping facility using nylon glass-reinforced material produced from the DTM Sinterstation 2000.

Housings 3 through 6 were tested for strain transfer. The extensometer design was utilized to amplify strain and increase sensitivity by increasing the distance from the neutral axis of the rod to the outside surface of the extensometer housing. The locking mechanism from the ferrite coupler was incorporated in the first and second housings, however, it did not apply adequate clamping pressure required to transfer strain from the rod and was abandoned. The hinge from the ferrite coupler was also added to the solid model shown in Figure 20. It did not help the design and was changed to the two halves design #6 as shown in Figure 21.

2.2.1.2 MTS Testing Configurations

Measurements Group CEA-06-062UW-120 strain gages were attached to the outside surface of the housing and on a 6.25 mm diameter 316L stainless steel rod adjacent to the housing, as shown in Figure 22a and 22b. This illustration shows three test rods with housings attached to the rods using small hose clamps and safety wire.

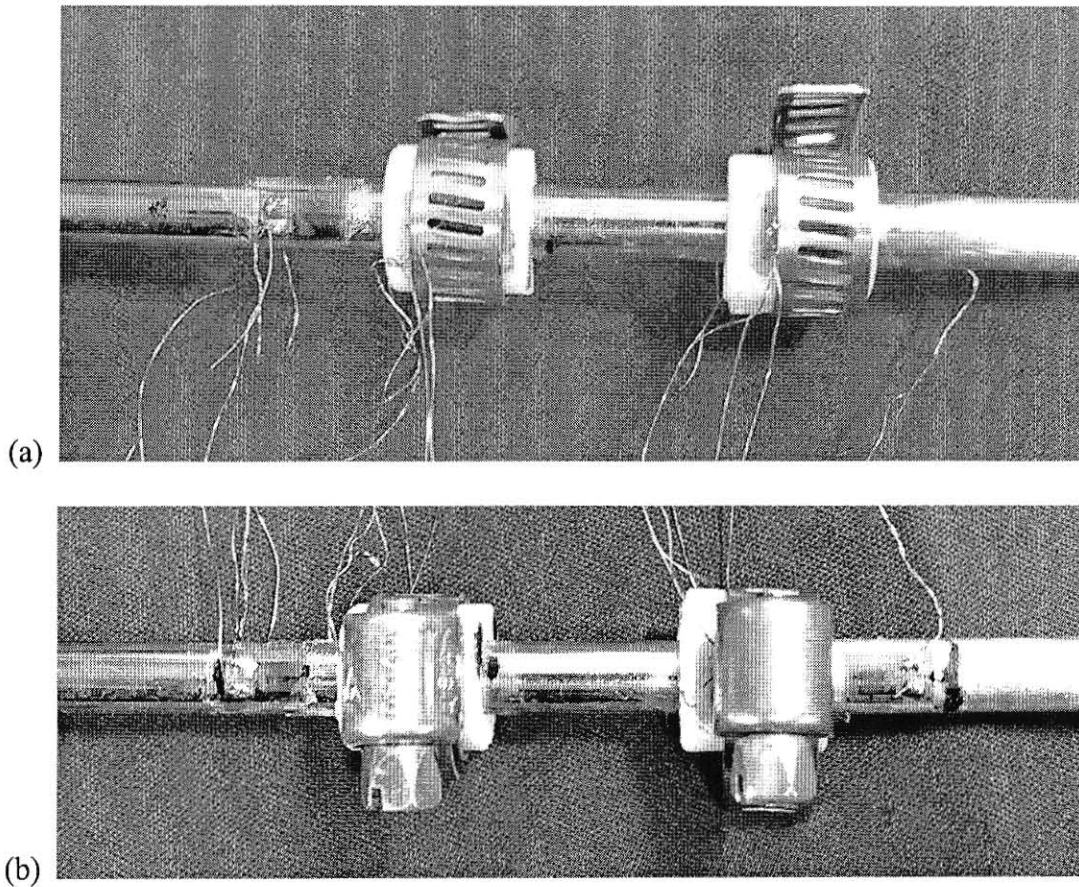


Figure 22. Illustrations (a) and (b) show the top and bottom of a test rod with housing design 6 affixed with hose clamps.

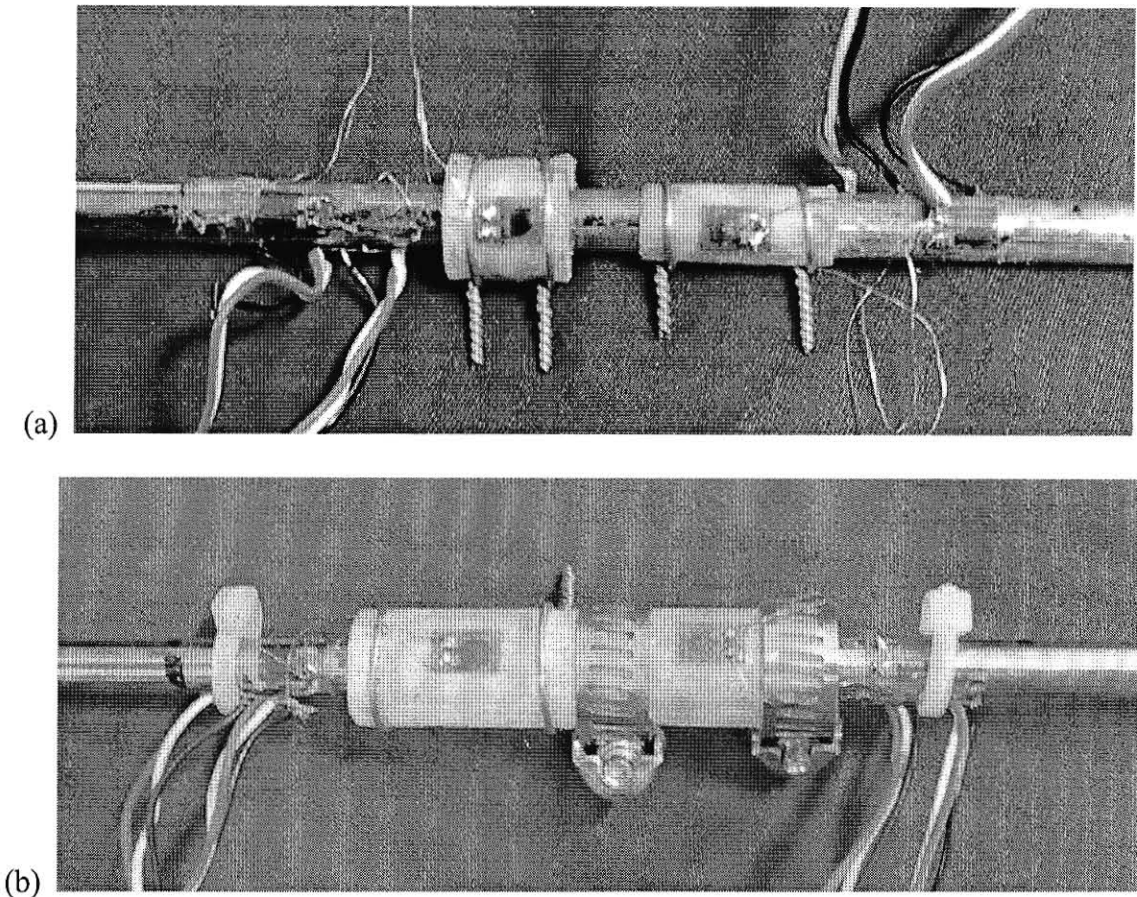


Figure 23.(a) A test rod with housing design 4 on the left and design 5 on the right, where both were affixed with safety wire. Illustration (b) has two examples of housing design #3 with the left housing affixed with safety wire and the right housing attached with hose clamps.

Each rod was placed and loaded in the MTS in four point bending. This configuration was selected to create uniform strain across the rod surface and to replicate loading of the implanted rod. Figure 24 shows the rod in the MTS fixture, the load configuration of the rod in the MTS and the resulting moment diagram from the applied loads. The moment diagram demonstrates uniform strain by the plateau developed between the two loading points of the upper channel in the MTS fixture.

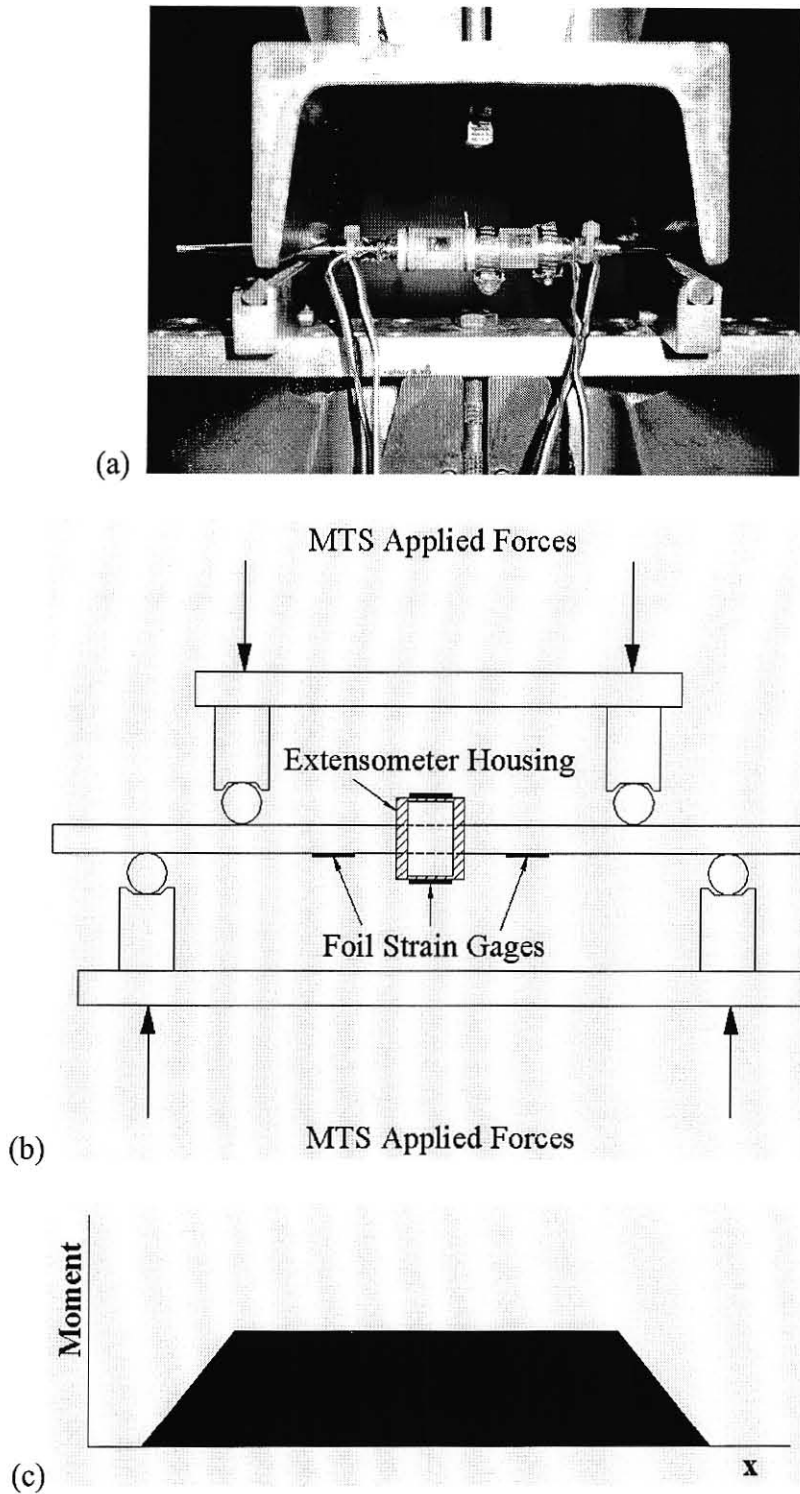


Figure 24. MTS fixture to achieve uniform strain at the surface of the rod (a) MTS with a rod loaded in the test fixture (b) A graphic of the loads applied by the MTS and placement of the strain gages on the rod. (c) The moment diagram as a result of the four-point bending test fixture in the MTS.

The strain gages were connected to a 2120A Measurements Groups strain gage conditioning unit and shunt calibrated in a Wheatstone half-bridge configuration. This bridge configuration was selected to compensate for temperature fluctuations during testing. A dummy strain gage was mounted on the stainless steel rod and housing for temperature compensation. Figure 25 shows the wiring diagram used for this arrangement and how the dummy gage serves as the compensating component.

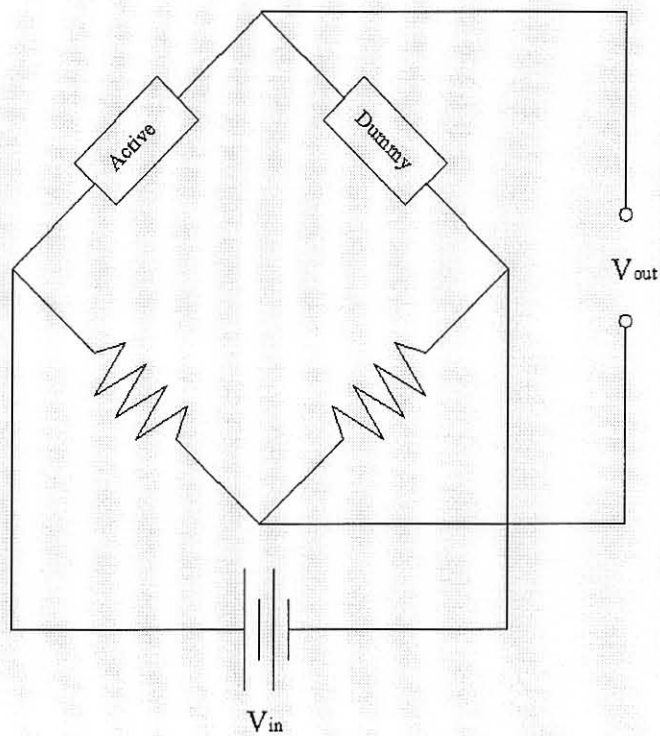


Figure 25. Wiring arrangement for the Wheatstone half-bridge.

The test rods were loaded at increasing intervals of 22 N and strain readings were manually recorded from the gages on the rods and housings.

2.2.1.3 Housing Material Selection

Material constraints for the housing included:

- a. Biocompatibility
- b. Implantable for long term.
- c. Can be sterilized.
- d. Easily and inexpensively manufactured.

Metallic materials were not considered due to interference with the telemetry system and ceramics were not chosen due to difficulties in manufacturing and attachment.

Polymers have moderate strength, are low cost, abundantly available and possess physical properties that can be regulated by design composition, internal structural arrangement and processing [35]. Polymers used in clinical applications include acrylic, polyester, UHMWPE, silicone, polyester, PVC and PEEK [36-49]. Desired characteristics included a high modulus of elasticity and the capability for injection molding, while maintaining isotropic elastic properties. Materials considered acceptable were:

1. Ultra High Molecular Weight Polyethylene (UHMWPE)
2. Polymethylmethacrylate (PMMA, Plexiglass®)
2. Acetal Resin (Delrin®)
3. Polycarbonates (Lexan®)
4. Polyetheretherketone (PEEK)

Only Lexan®, Delrin®, PEEK and 30% Carbon Filled PEEK was used for testing for they contained the largest diversity of material characteristics.

The PEEK material was particularly attractive and is offered by Invibio as PEEK-Optima®. This material is approved for long-term implantation and can be injection molded [50]. Applications include spinal fusion cages, suture anchors, spiked washers, surgical screws, femoral implants, dental healing caps, balloons, intercardiac pumps and heart valves [51].

2.2.1.4 Housing Material Testing

The short sleeve housing design was modified to include a securing flange and was evaluated for each of the materials. Figures 26 and 27 show the housings constructed from Lexan, Delrin and PEEK. Nuts secured the threaded screws and applied circumferential pressure to the rod from the housing. The housings were tested to determine if adequate strain transfer would occur using four-point bending.

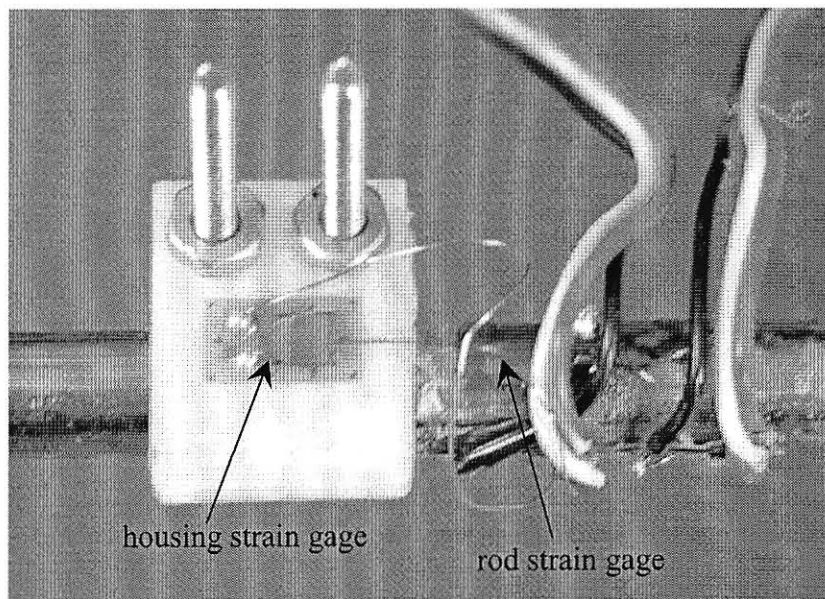


Figure 26. An illustration of the Delrin sleeve housing secured to the sleeve design using screws.

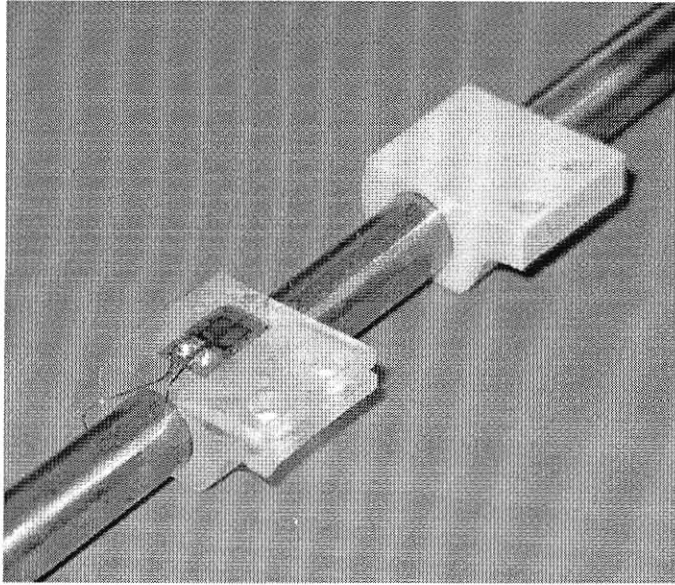


Figure 27. Housings fabricated using Lexan and PEEK not secured with screws.

2.2.2 Preliminary Housing Results

2.2.2.1 MTS Testing Results for Rapid Prototyped Models

Figures 28 through 31 show results from MTS testing for the rapid prototyped housings. Results, shown in Figure 28, for the two halves design attached with hose clamps shows poor rod strain transfer. Rod strain gages were mounted on either side of the housing and averaged to obtain a measure of applied rod strain at the housing location.

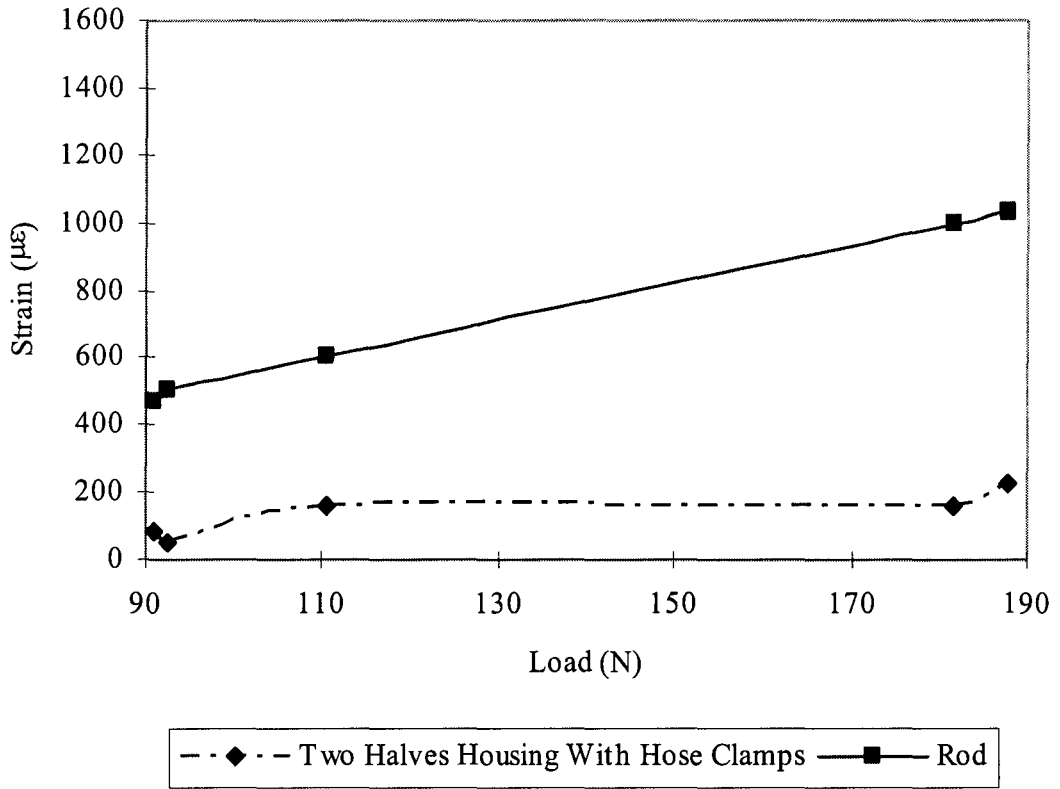


Figure 28. Graphical results of the rapid prototyped two halves housing design with hose clamps.

Results are shown in Figure 29 for the two halves design adhered to the rod using cyanoacrylate adhesive and hose clamps. Rod and housing strain values are comparable showing good strain transfer.

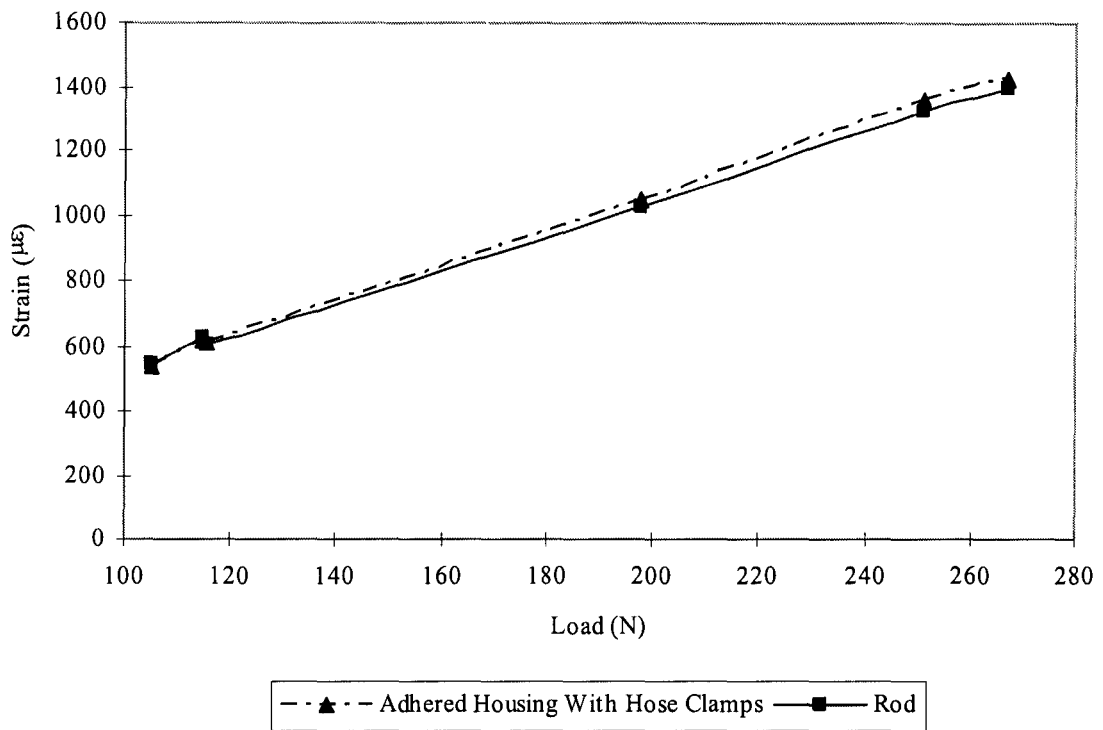


Figure 29. Graphical results of strain versus load for the two halves design mounted to the bar with cyanoacrylate adhesive and hose clamps.

Figure 30 shows the results for the long sleeve and short extensometer housing attached with safety wire. The short extensometer housing exhibits poor strain transfer, while the sleeve design demonstrates approximately equal rod strain values showing good strain transfer.

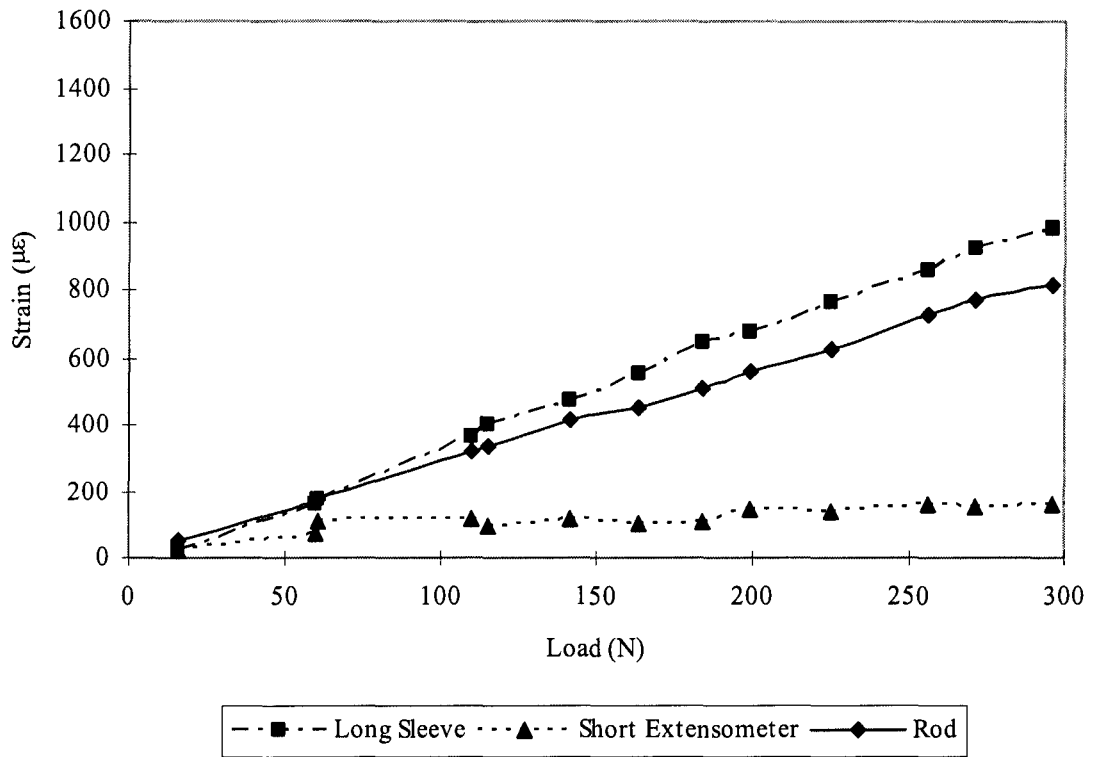


Figure 30. Strain versus load results for the long sleeve and short extensometer housings mounted to the bar with safety wire.

Figure 31 shows the results for the long extensometer housings affixed with safety wire and hose clamps. Results for the extensometer attached with hose clamps shows good strain transfer, while data from the housing attached with safety wire shows negligible strain transfer.

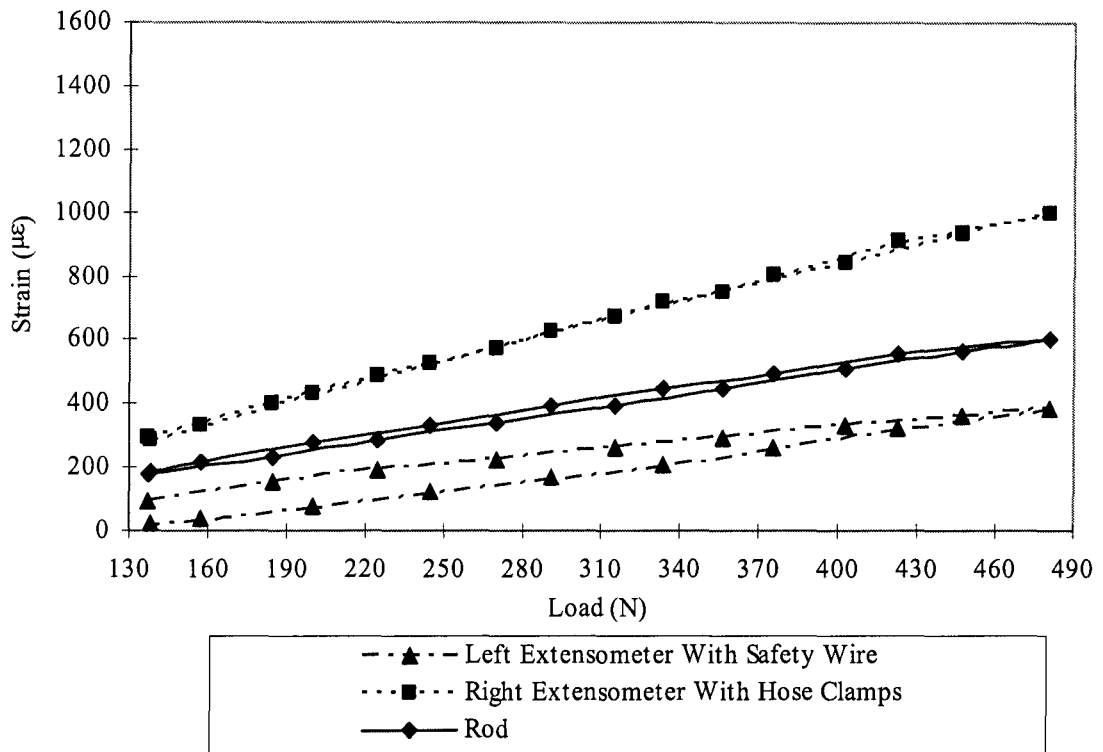


Figure 31. Results for the extensometer using two different clamping techniques.

2.2.2.2 MTS Testing Results for Preliminary Housings of Various Materials

Figures 32 to 34 show results from the Delrin, PEEK, 30% Carbon-filled PEEK and Polycarbonate housings. Each housing result shows poor strain transfer and hysteresis.

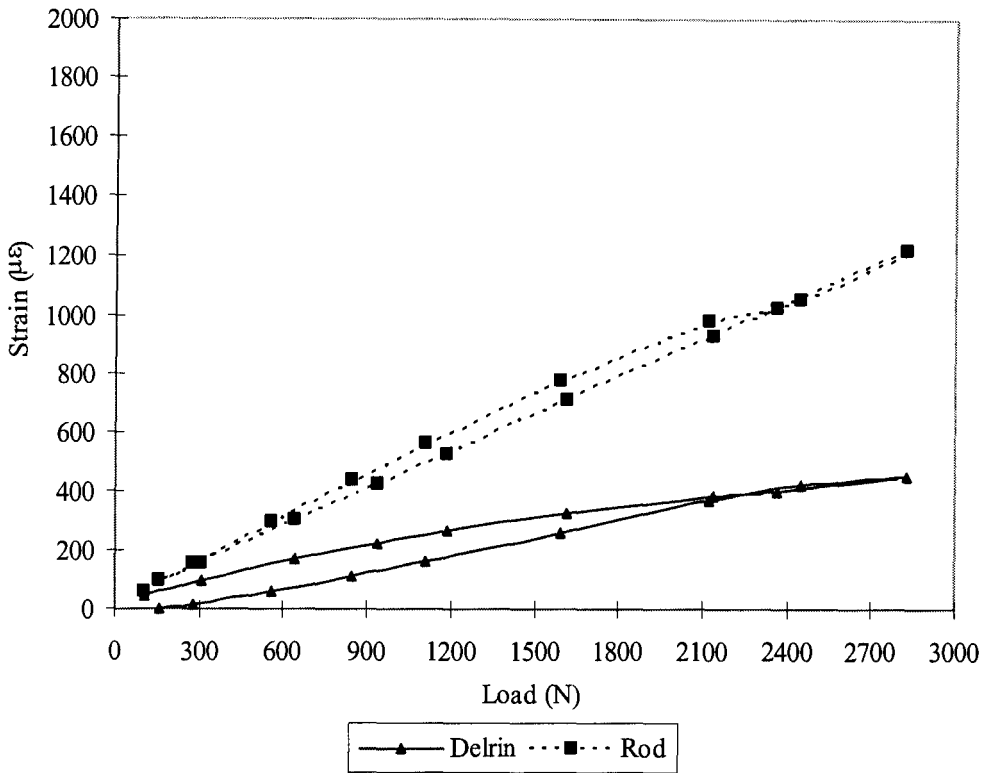


Figure 32. Four-point bending test results for the Delrin housing attached with screws.

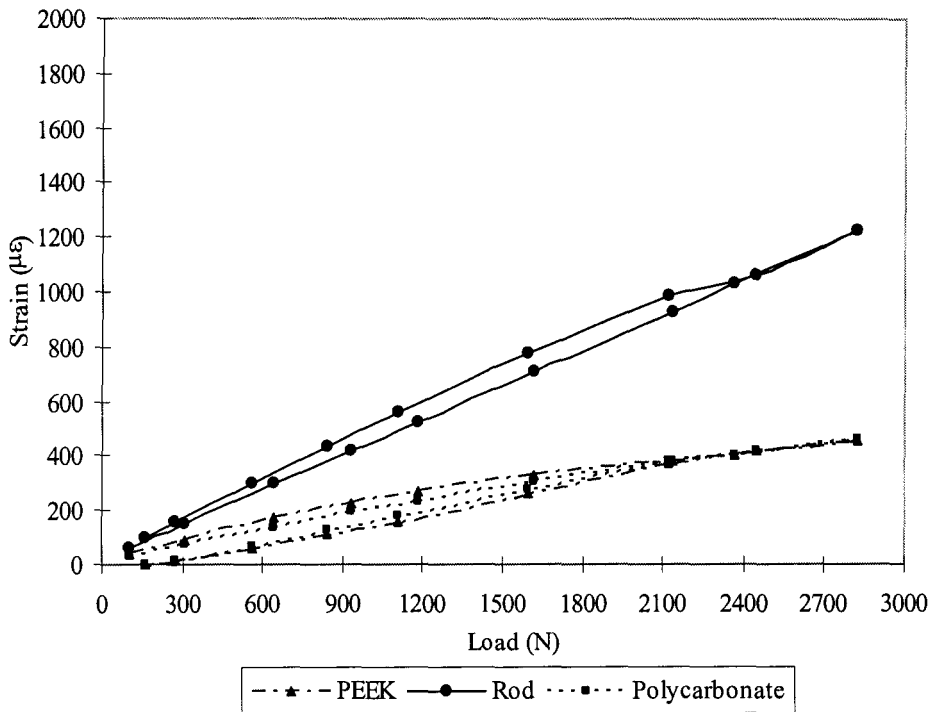


Figure 33. Results of the PEEK and Polycarbonate housings attached with screws.

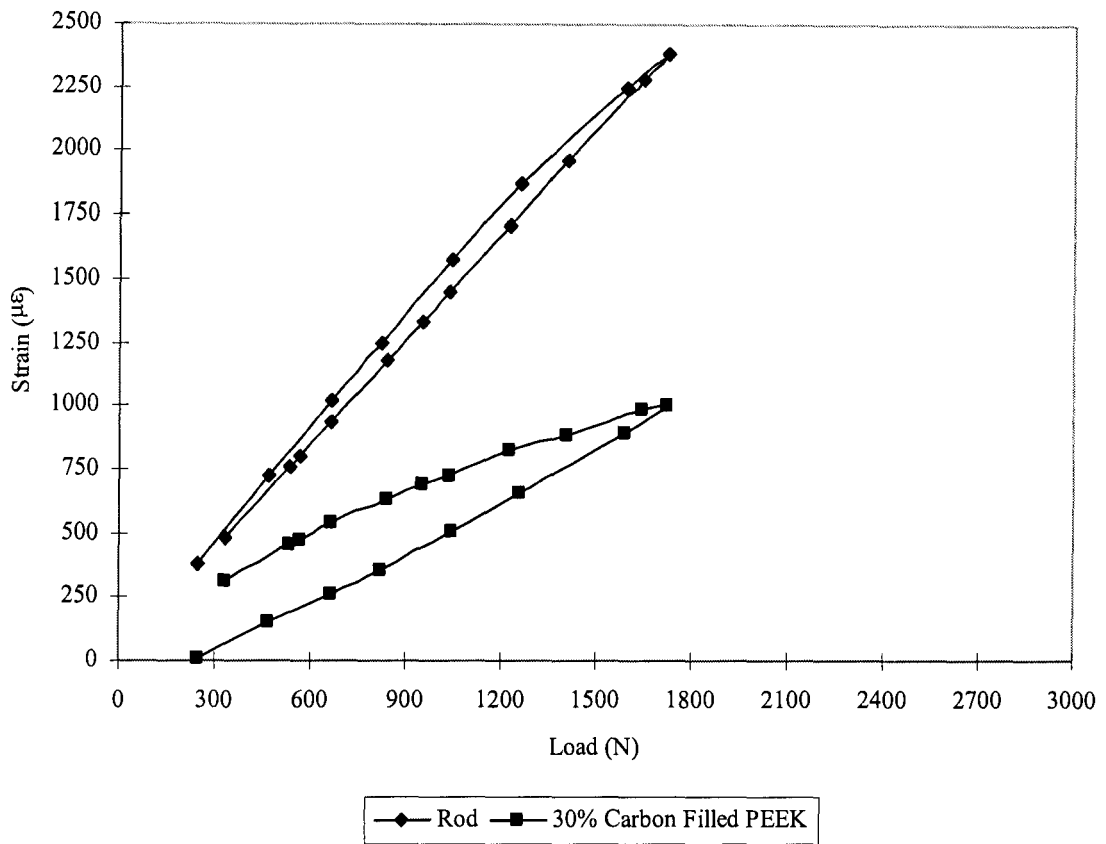


Figure 34. Results of the 30% Carbon Filled PEEK housing attached using screws.

2.2.3 Preliminary Housing Discussion

2.2.3.1 Discussion of the Rapid Prototyped Models

Results shown in Figure 28 of the two halves rapid prototyped design attached with hose clamps shows poor strain transfer due to the apparent differential between the housing and rod strain. In an effort to improve strain transfer the housing was affixed to the rod with cyanoacrylate adhesive and hose clamps. The result gave comparable

housing and rod strains and demonstrated good strain transfer. The adhesive illustrated that adequate rod strain transfer can be obtained if the housing conforms and remains in contact with the surface of the rod.

However, the use of adhesives to secure the housing to the rod was not a viable option. A clean interface is required between the housing and rod to develop an effective bond, which would be difficult to maintain during surgery. Other concerns were degradation of the bond during long-term exposure in the implanted environment. In addition, the housing could not be applied to rod before implantation due to bending of the rod to match the contour of the patient's lumbar spine.

The long sleeve housing data results shown in Figure 27 shows 115% to 120% rod strain transfer. This was attributed to the increased distance from the neutral axis of the rod to the surface of the housing as evident from equation (2). Also apparent were similar strain values from the strain gages attached directly to the rod indicating that a uniform magnitude of strain was occurring on the surface of the rod. However, strain results from the short extensometer were inadequate due to lack of clamping pressure applied by the safety wire. This clamping mechanism was effective for the sleeve design due to the lower stiffness of the cross-section as compared to the same clamping area of the extensometer. Safety wire was also used for the two-halves design, however, the adhesive was identified as the effective component to transfer strain rather than the safety wire.

Different clamping mechanisms were evaluated using the long extensometer housing design on test rod three. However, this housing design had several issues that made it unsuitable for the application. The length of the housing was longer than the

13mm length constraint. Also, the location of the upper skin would decrease space for the sensor and telemetry circuitry and increase the overall diameter of the sensor housing. Testing did proceed despite these issues to evaluate the effect of the clamping mechanism.

The results show approximately 164% strain transfer of rod strain for the extensometer attached with hose clamps. From these tests, the extensometer housing design secured with hose clamps provided the highest amplified response and increased sensitivity. This was attributed to the increased distance from the neutral axis to the upper skin of the extensometer compared to the dimensional distance from the rod surface distance to the neutral axis. Hysteresis was noted for the extensometer housing secured with safety wire. This was not fully investigated due to the poor results from the design, but it became evident from testing that adequate clamping pressure was a critical parameter for strain transfer.

2.2.3.2 Discussion of the Preliminary Housings of Various Materials

Test results for each of the housings fabricated from the various materials demonstrated poor rod strain transfer and hysteresis. During testing, the edges of the housing receded and lost contact under load at the rod interface. Due to insufficient circumferential clamping pressure, the housing would not conform to the surface of the rod and resulted in poor strain transfer. Lack of housing development changed the course of design to incorporate finite element analysis to understand the shortcomings of the design and to develop an adequate geometry that would fulfill the constraints.

2.2.4 Conclusions for Preliminary Housings

Constraints established for the housing required that strain exhibited on the rod must equal or exceed strain on the housing. Testing of the various designs to meet these constraints developed the following conclusions from the gathered data.

1. Implementation of four-point bending in the MTS was an effective technique for evaluating the effectiveness of rod strain transfer for each design.
2. The amount of clamping pressure on the housing directly controlled the effectiveness and percentage of strain transfer.
3. The use of adhesives to affix the housing provided good rod strain transfer; however, they were determined impractical for installing the system onto the spinal rods.
4. An analytical method, such as finite element analysis, can assist evaluation of new housing designs for rod strain transfer.

2.3 Final Housing Approach

Due to the variety of problems encountered with determining the housing design geometry, materials, fabrication time and cost it was determined to use finite element analysis (FEA). This tool could quickly help determine if the selected design parameters would be sufficient to transfer 100% of strain from the rod to the housing. Analysis

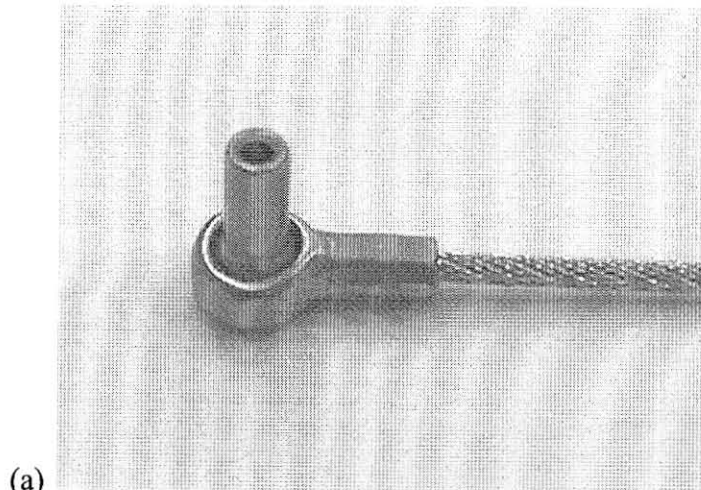
would also help understand why previous design attempts had failed and to determine correct design geometry.

ABAQUS (ABAQUS, Providence, RI, ver 6.3-1) finite element analysis software was used to develop models guided from data and design parameters from MTS testing. A housing was fabricated based upon the modeling results and tested in four-point bending. The telemetry circuitry and a strain sensor were integrated with the housing and the system was implanted on a cadaver spine and evaluated.

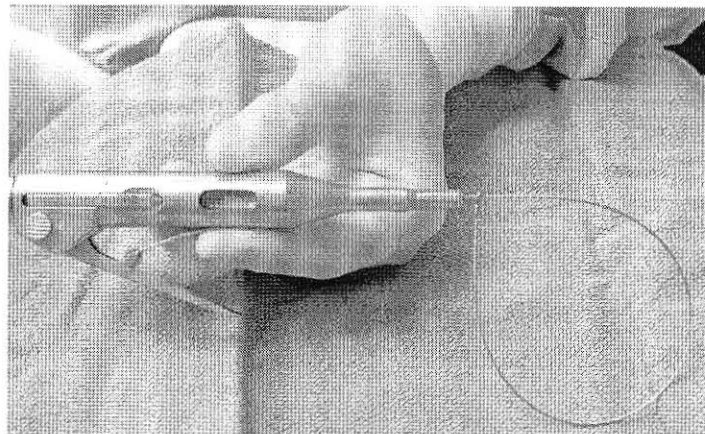
2.3.1 Materials and Methods

Material selection was carefully considered and PEEK-Optima® was chosen for its material properties and medical device application. Modeling was approached in three key steps by establishing initial conditions, clamping of the housing to the rod and bending of the rod to simulate loading conditions in the lumbar spine. Boundary conditions, load application, interaction properties and mesh details are discussed in detail.

After modeling was completed, the housing was fabricated using virgin PEEK material. The housing was mounted onto the rod using the Atlas Cable System provided by Medtronic Sofamor Danek. This system was also selected for its established presence in orthopaedic surgery. Figure 35 shows the stainless steel cable before it is applied in surgery and tooling to tighten the cable during application.



(a)



(b)

Figure 35. Illustrations of the Atlas Cable System manufactured by Medtronic Sofamor Danek. (a) The spherical bearing head of the cable allows the end of the cable to pass thru it as seen in (b). The tool in this illustration allows the cable to be tightened around an object to a specified pressure.

Strain gages were applied to the housing surface where the sensor would reside with additional gages placed on the rod to the left and right of the housing. Custom LabView (National Instruments, Austin, TX) virtual instruments were written to record strain values from the housing, rod and load from the MTS.

A series of tests in the MTS were performed on the rod with the attached housing to simulate long-term implantation. The first test applied a cyclical load for a specified duration to replicate movement of the patient and to determine if the strain signal would

degrade over a period of time. The second test applied a constant magnitude of strain above 1000 $\mu\epsilon$ for a long period of time to determine if creep would occur or if the strain signal would decay. The final test established if the housing would continue to transfer strain at elevated levels beyond 1000 $\mu\epsilon$.

After characterization of the housing in the MTS, the rod and housing were prepared for implementation in a cadaver spine. A MEMS-based capacitive bending strain sensor, designed by Ji-Tzouh Lin, was attached to the housing's sensor surface and electronic telemetry circuitry, developed by Douglas Jackson, was connected to the sensor. A temporary outer cover fabricated in the rapid prototyping center was placed around the system for protection. The system was placed in the MTS and submerged in a water tank to test if leakage would occur. The system was placed in the lumbar spine of a cadaver male approximately in his 70's. The cadaver was physically manipulated to induce strain on the rod and the response of the system along with strain data from the rod was measured using a customized LabView program.

2.3.1.1 ABAQUS Finite Element Modeling of the Final Housing

The sleeve design was modeled in ABAQUS, with variation applied to the sensor surface cross-sectional thickness, distance from the rod to the sensor surface and the cable guide width, as shown in Figure 36.

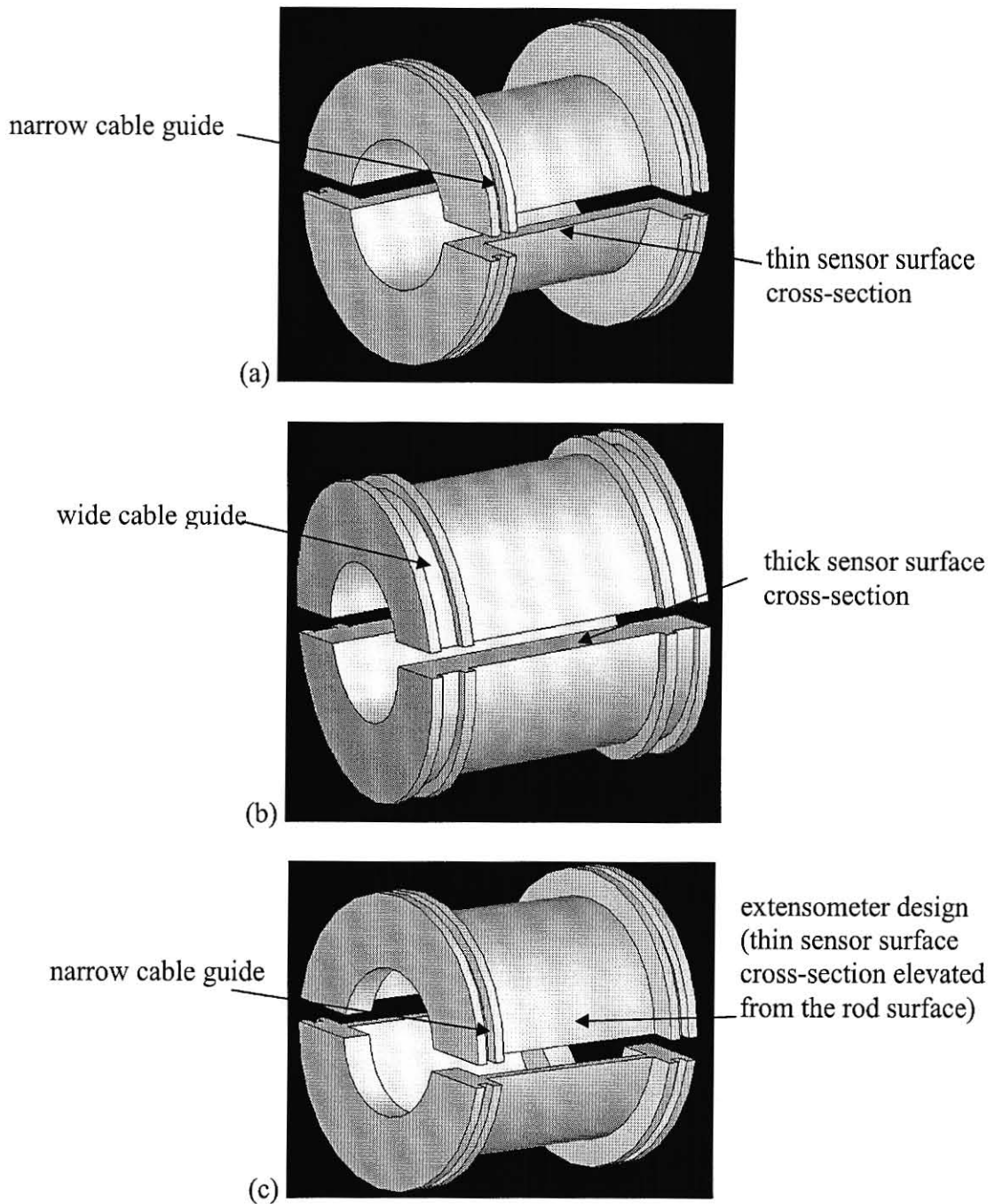


Figure 36. Initial housing designs with (a) housing with a thin wall section next to the rod surface and a thin wire channel, (b) housing with a thick wall section near the rod surface and a wide wire channel and (c) extensometer design with a thin wall section that is elevated away from the rod surface.

The housing would be attached to the spinal fusion rod with the Atlas Cable System manufactured by Medtronic Sofamor Danek.

The material Polyetheretherketone (PEEK), named PEEK-Optima® and commercially available by Invibio, was selected for its ability to be implanted greater than one year, capability to be injection molded and be sterilized. The isotropic material has characteristics of 0.4 for Poisson's ratio and a Young's Modulus of 4.09 GPa.

The housing and rod were modeled as shown in Figure 37. A successful design was determined when the strain transfer from the rod surface to the housing sensor surface achieved 100%. Analysis progressed in three steps, with application of the initial conditions, clamping of the housing to the rod and loading the rod to induce bending. The initial step fixed the assembly in space and defined interaction characteristics between the housing and rod.

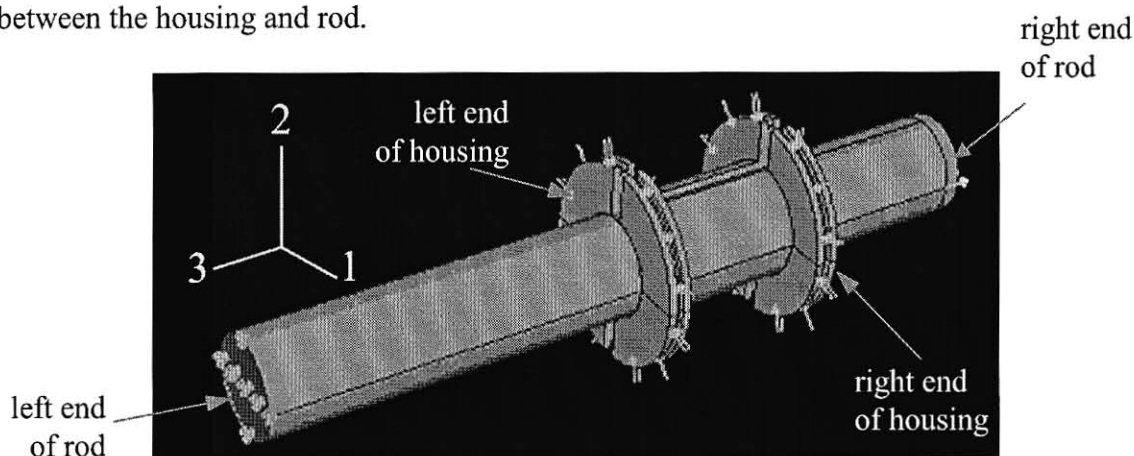


Figure 37. ABAQUS FEA model of the housing and rod.

The tangential interaction parameters between the housing and rod were specified with a friction coefficient of 0.19 and isotropic material properties. Normal interaction between the housing and rod was defined as hard contact and allowed separation after contact. Clamping of the housing to the rod was simulated by applying a uniform normal pressure of 10 MPa to the cable guide surfaces. The final step replicated vertebral loading by applying a bending moment to the rod. The moment was produced by

applying a load on the right end at the top of the rod in the positive 3 direction and in the negative direction on the bottom right end of the rod. The rod loads remained normal to the end of the rod during bending, thereby producing constant bending strain on the surface of the rod. Figure 38 is an illustration of the loads and their direction applied to the rod.

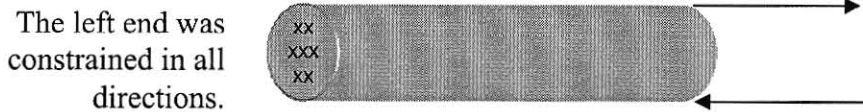


Figure 38. Loading of the bar in the ABAQUS model.

Boundary conditions were applied separately to the housing and rod during each step of the sequence to simulate installation conditions during surgery. The coordinate system used for the model is illustrated in the upper left corner of Figure 37. During the initial step, the housing and rod were restrained on the left end in all three directions.

The right end of the rod and housing were fixed in the 1 and 2 directions.

The second step applied uniform clamping pressure to the housing. The left end of the rod was fixed in all three directions, but the right end of the rod was unconstrained. During this step, the left end of the housing was constrained in the 2 and 3 directions with the right end constrained along the 2 direction.

The last step applied loading to the rod to induce bending and to replicate loads applied by the lumbar spine. The left end of the rod was fixed in all three axial directions while the right end of the rod was constrained in the 1 and 2 directions. No boundary conditions were applied to the housing during the loading step for contact between the housing and rod was maintained by the clamping pressure.

The rounded surfaces of the housing and rod were meshed using 10-node modified quadratic tetrahedrons or C3D10M elements, as seen in Figure 39. The rod and housing element sizes were 0.7 mm and 0.3 mm, respectively. The size of the rod elements were chosen when the strain gradient observed on the rod possessed adequate resolution. The housing elements were intentionally smaller due to the contact interaction, where the conforming housing material required a smaller element size than the harder rod material. The housing contained 72,522 elements and the rod used 24,780 elements.

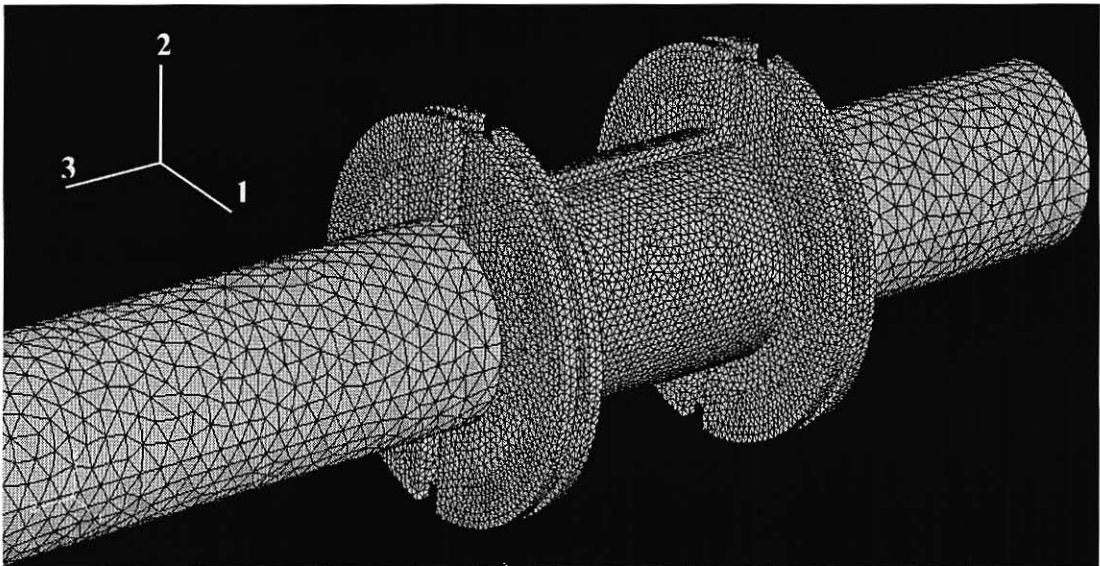


Figure 39. An illustration of the meshed assembly.

After the model was assembled the loading and boundary conditions were applied. The model was submitted for analysis to a Silicon Graphics Onyx 2 Infinite Reality super computer. Computational time of the model required 23 hours to complete because of the interaction complexity between the housing and rod. Due to model complexity a convergence study was not performed.

2.3.1.2 Fabrication, Fixturing and MTS Testing of the Final Housing

Prototype housings were fabricated from virgin PEEK material using parameters achieved from the FEA model. The design was modified to create a housing with a large side opening to accommodate the spherical bearings of the Atlas Cable System, as shown in Figure 40.

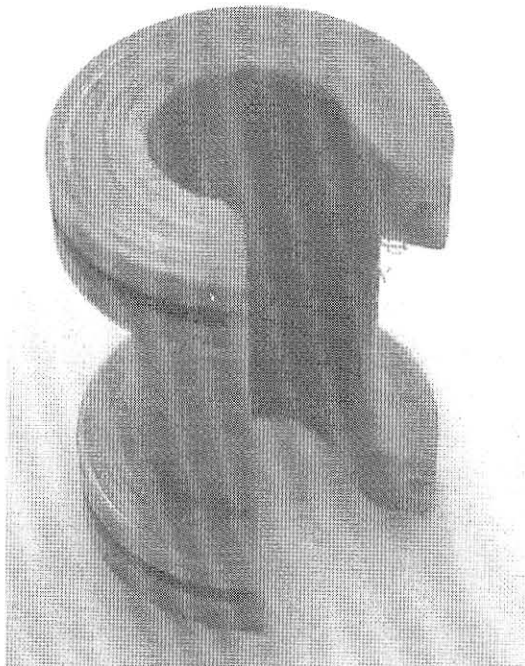


Figure 40. The one piece housing manufactured from PEEK and with a large side opening to accommodate the spherical bearings of the Medtronic Sofamor Danek Atlas Cable System.

For simple installation the surgeon would snap the housing onto the rod and affix it using the Medtronic Sofamor Danek Atlas Cable System. Figure 41 shows a series of illustrations that demonstrates how the housing is secured to the rod.

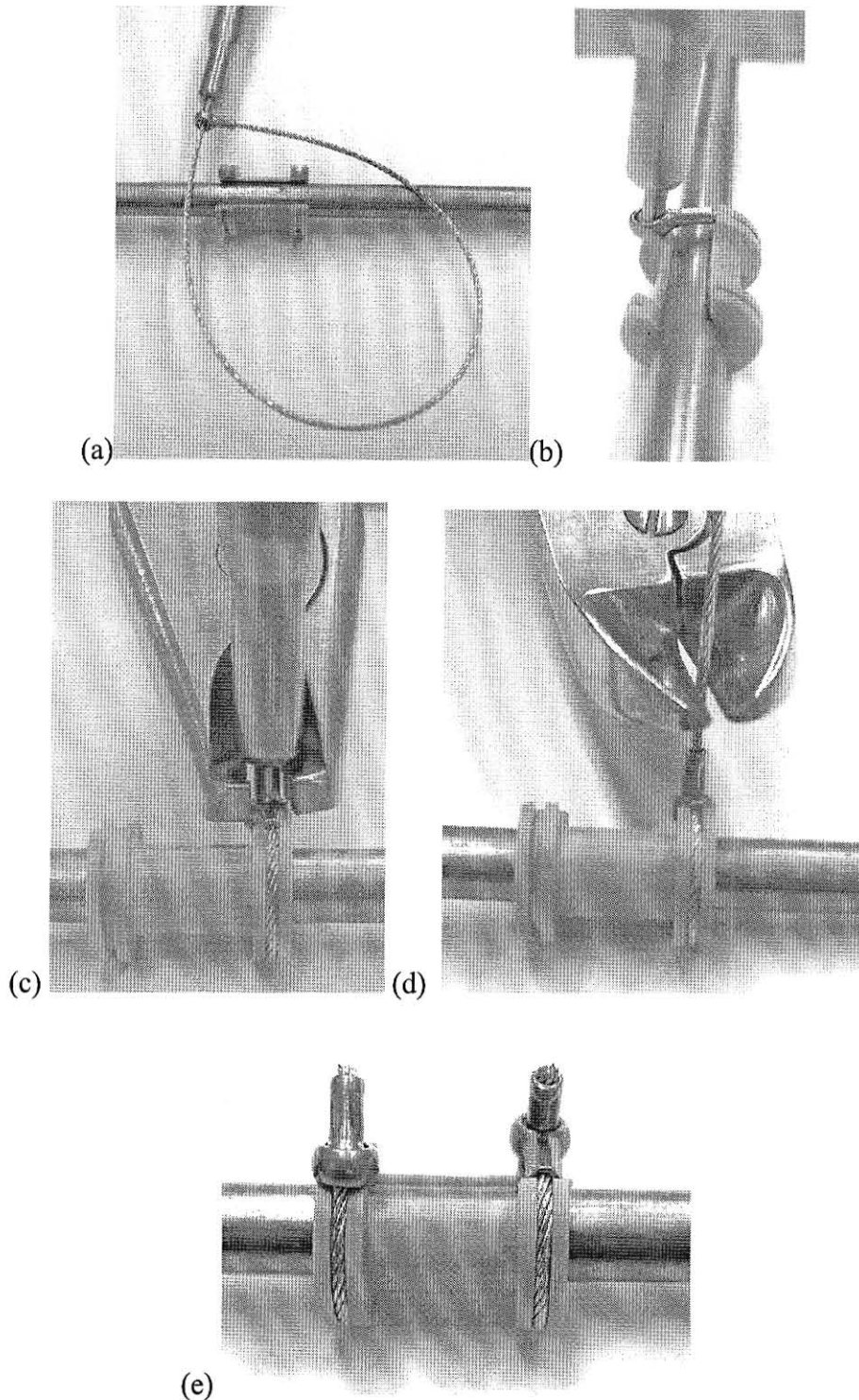


Figure 41. Method of attaching the housing to the rod (a) The housing is snapped onto the rod and the cable is loaded in the tensioning tool. (b) The cable is applied to the cable guide of the housing and tightened to 50 lbs/in². (c) While the cable is held in tension the clamping device crimps the stem of the spherical bearing securing the cable in place. (d) The cable cutter cuts the excess cable. (e) Two cables are used to secure the housing to the rod.

The rod was configured in four-point bending in the MTS fixture to evaluate rod strain transfer, as shown in Figure 42. The MTS load controller was manually manipulated to apply selected loads to determine if the housing strain response would match or exceed strain generated on the rod. A low frequency cycle test was used to emulate implantation for one year, which is the typical evaluation period after surgery. A cyclical load at 0.05 Hz, 20 seconds per cycle or 900 cycles per test for five hours was applied to develop a varying rod strain of 350 to 1350 $\mu\epsilon$. If the housing response showed any characteristic changes then it was determined that the duration of the cycle test would be increased.

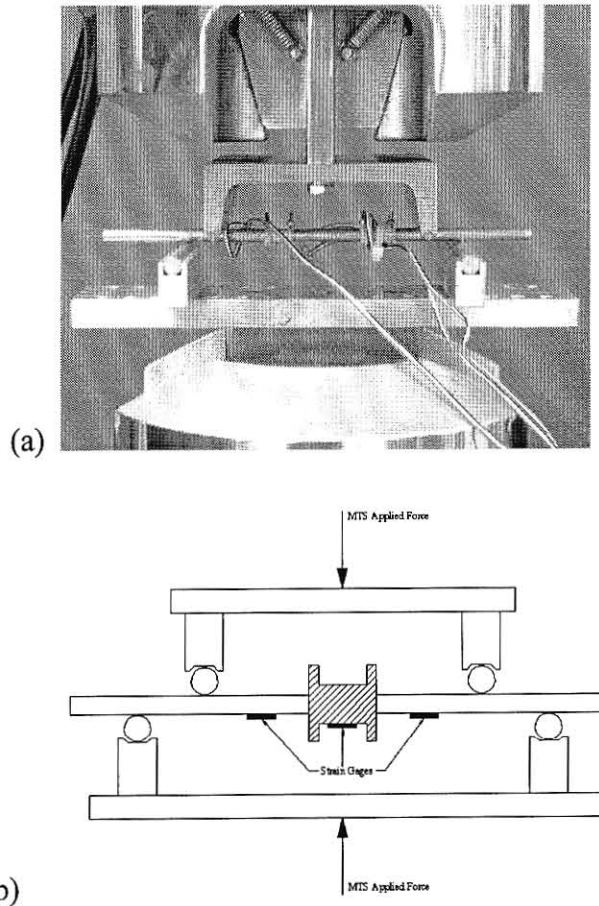


Figure 42. The MTS fixture used to achieve continuous strain at the surface of the rod. (a) The rod in the MTS under loading. (b) Graphic of the loading applied by the MTS on the rod and placement of gages on the rod.

Previous corpectomy modeling by Gibson determined the applicable strain range was 0 to 1000 $\mu\epsilon$. Therefore, the upper strain level was selected to exceed the 1000 $\mu\epsilon$ to ensure the housing would perform at elevated strain levels. The strain gages were connected to two 2120A Measurements Group strain gage conditioning units. Following shunt calibration, the strain signals were recorded using a custom virtual instrument developed in LabView (National Instruments, Austin, TX, ver. 6.1) and a National Instruments 6024 data acquisition card. Figure 43 shows the testing station including the MTS, strain conditioners, MTS load controller, oscilloscopes for strain signal monitoring and the computer utilized to record data with the customized LabView virtual instruments. Figure 44 shows analog traces of the strain data during cycle testing on the oscilloscopes, which were primarily used to precisely balance the strain gages.

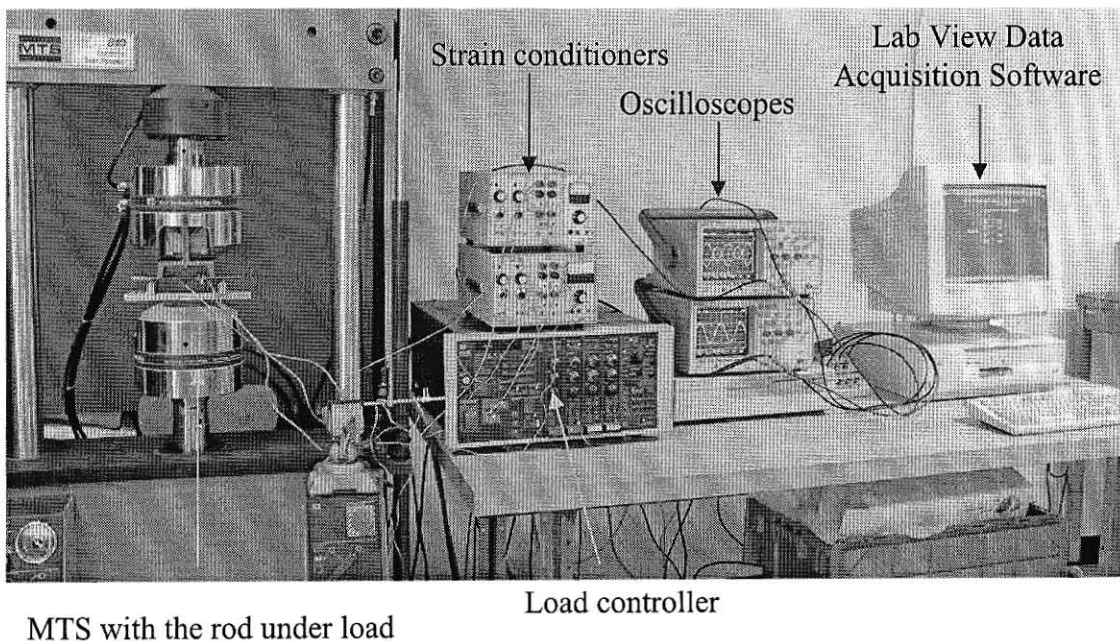


Figure 43. The testing system with the rod loaded in the MTS.

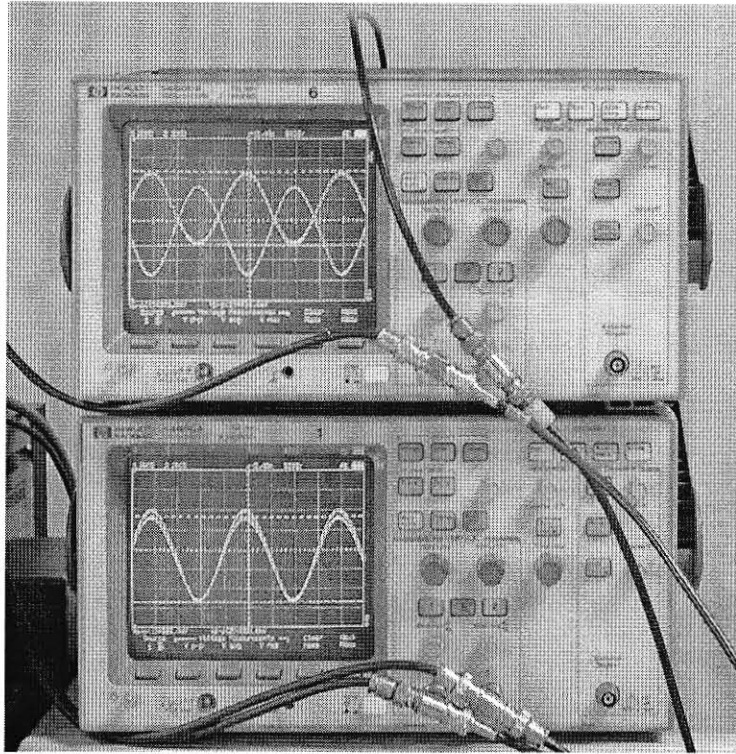


Figure 44. Oscilloscopes showing the strain gage signals and load data from the MTS.

A LabView virtual instrument was written to acquire data from the strain gages and the MTS load cell. A sampling rate of 20 data points per second was chosen for the input frequency of 0.5 Hz from the MTS to avoid aliasing determined by conditions from the Nyquist sampling theorem [52]. This theorem indicates that a continuous signal can be properly sampled only if it does not contain frequency components above one-half the sampling rate. The sampling rate was chosen to gain maximum and minimum values from each cycle and to recognize creep characteristics. Data was recorded in an array and written to a file during each cycle, where another virtual instrument extracted the maximum and minimum values of each cycle. Figures 45-47 show the front panel and diagrams for the virtual instrument.

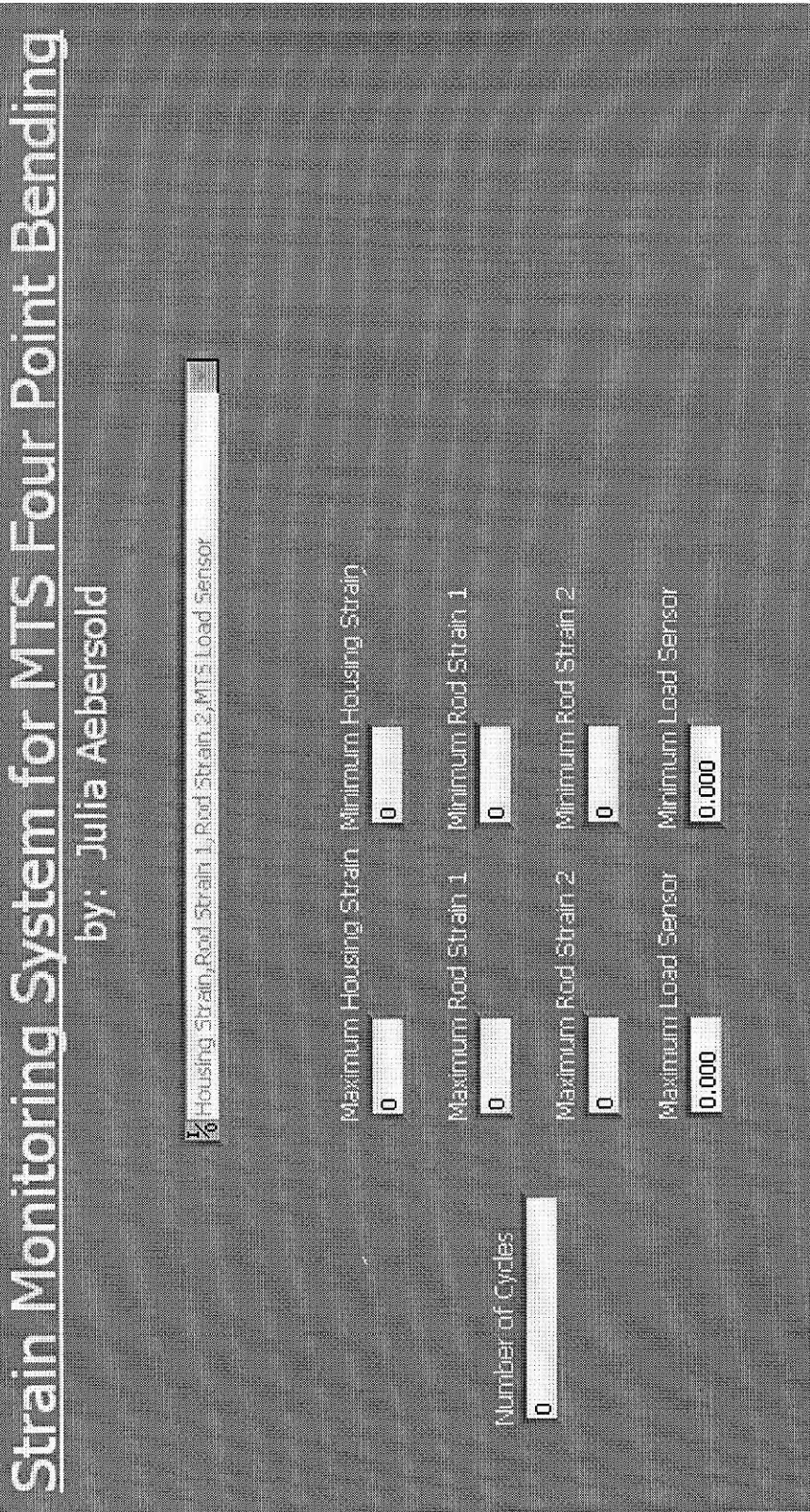


Figure 45. The front panel of the LabView program developed to collect data during housing testing.

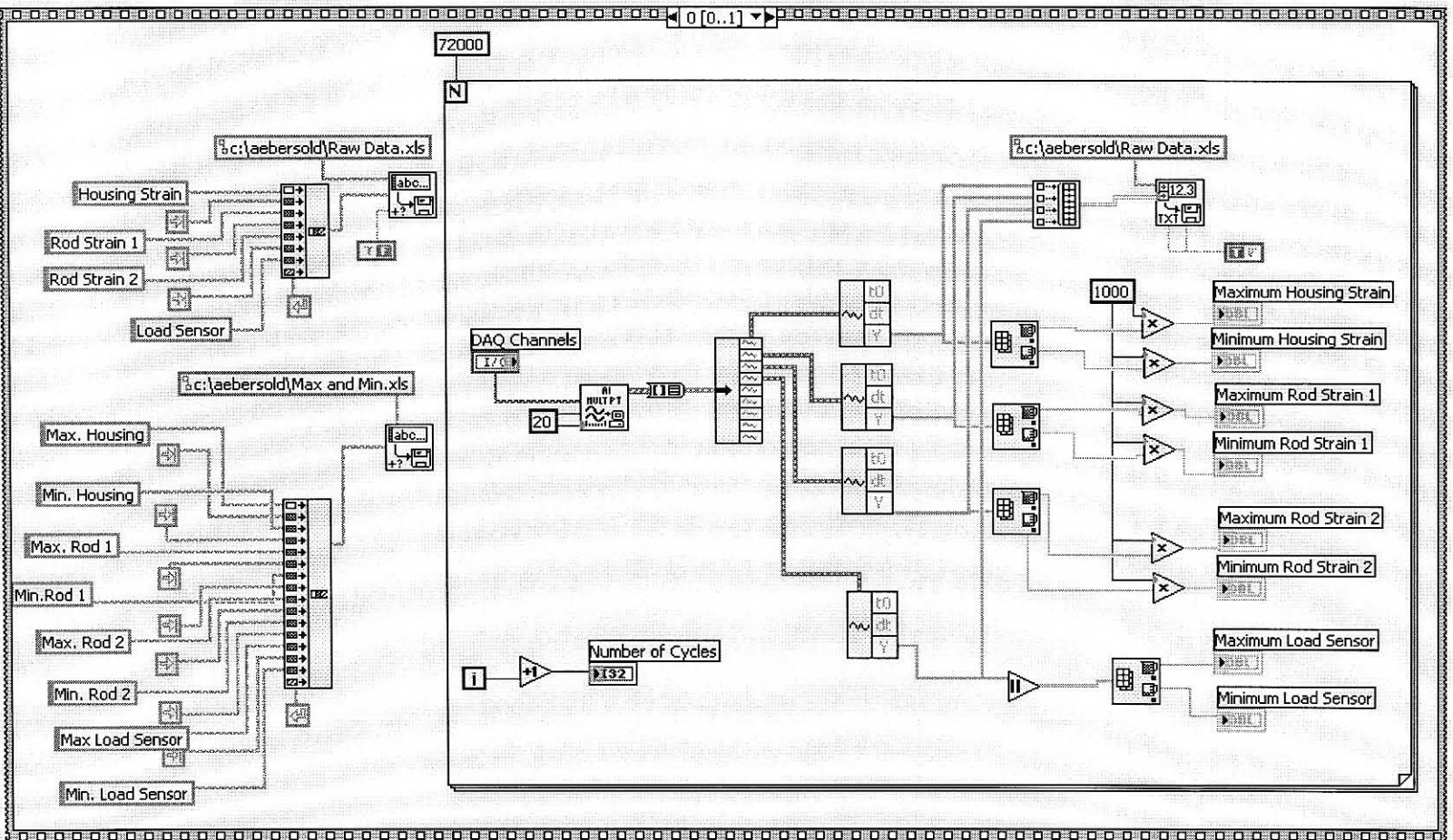


Figure 46. The diagram of the LabView virtual instrument used to collect data from the strain gages and MTS load cell.

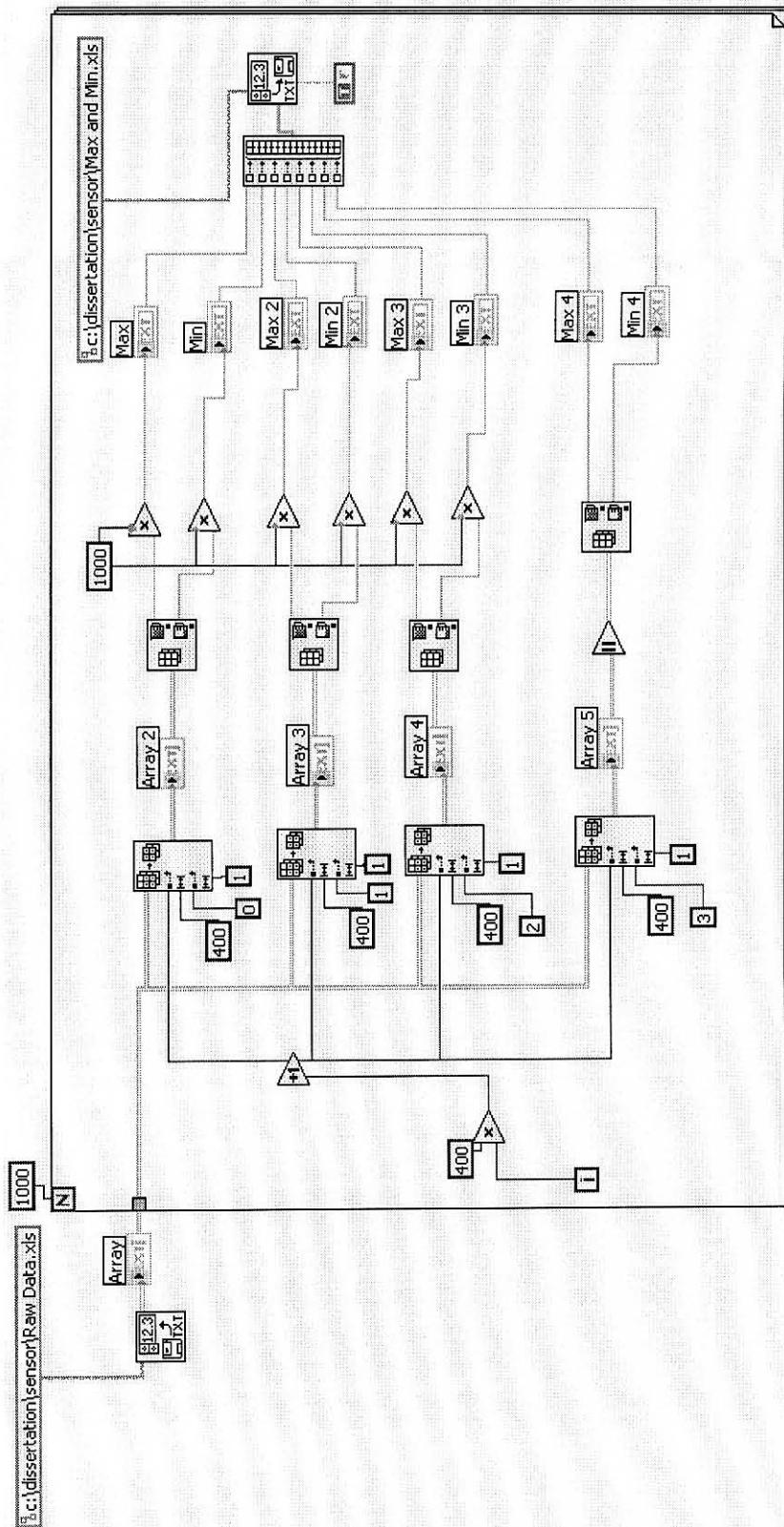


Figure 47. The diagram for the second virtual instrument used to extract the maximum and minimum values from each cycle.

2.3.1.3 Water Tank Testing of the Final Housing

A MEMS-based capacitive strain sensor and a telemetry circuitry were attached to the housing and tested using the MTS. A rosette strain gage was applied to the rod in addition to a single strain gage. A cover was fabricated using the rapid prototyping process to enclose the system components. The cover was box shaped with adequate room to cover the transmitting antenna of the telemetry system. Holes were placed in the cover and lid to allow it to pass onto the rod and enclose the housing with the telemetry components as shown in Figure 48.

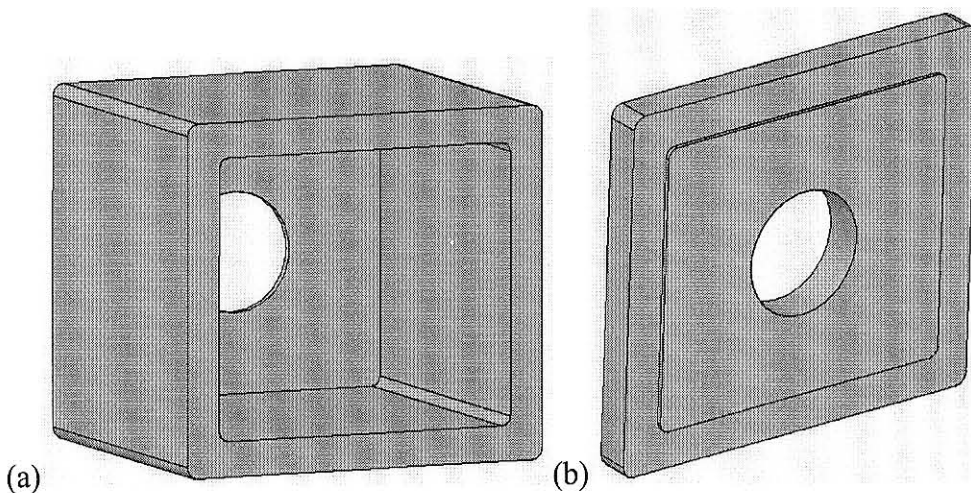


Figure 48. Illustrations of the box cover for the telemetry system.

The entire assembly was sealed using a silicone sealant to keep water from entering the system, as shown in Figure 49.

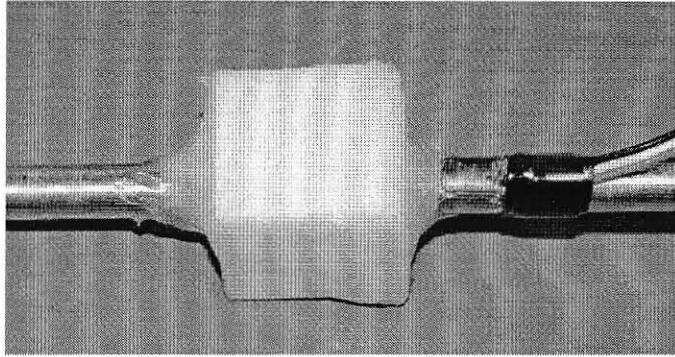
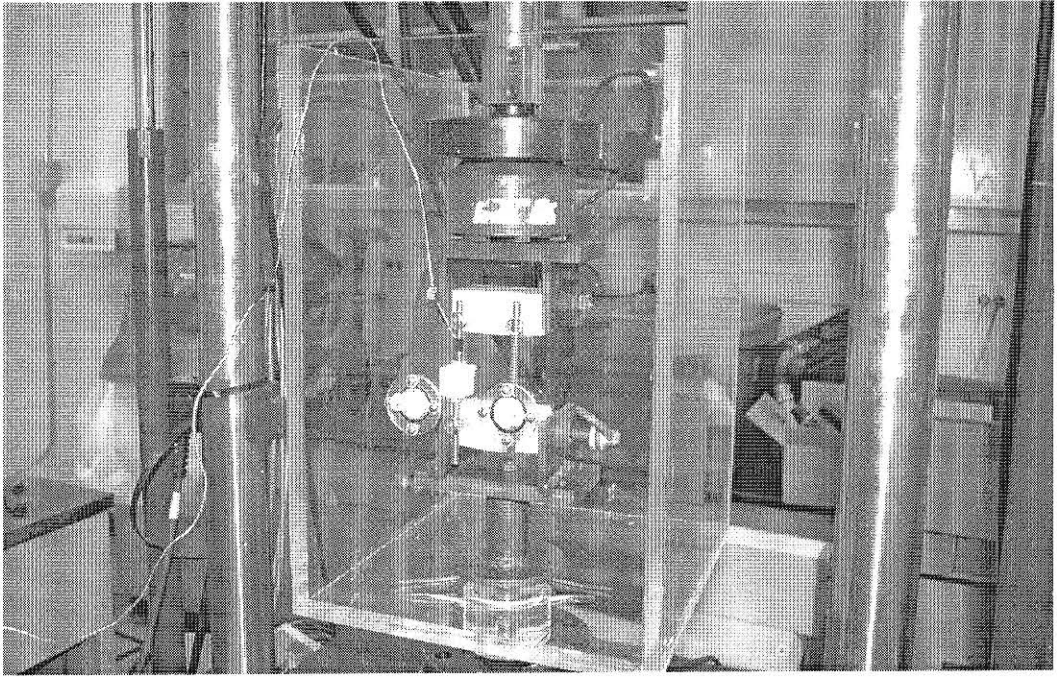
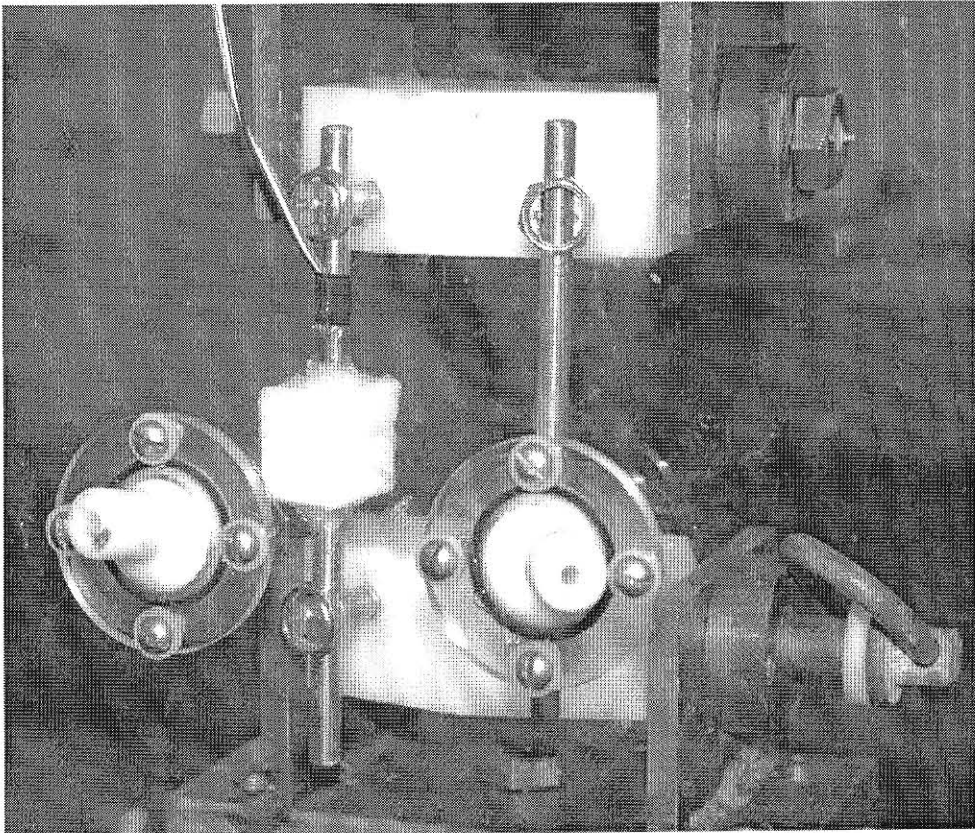


Figure 49. An illustration of the strain monitoring system enclosed in the box cover.

The system was mounted in a corpectomy model in the MTS and placed in a water tank, which submerged the system while undergoing four-point bending. Leakage, transmission range and response of the telemetry circuitry were evaluated. Figure 50 shows the system in the water tank while secured in the corpectomy model undergoing four-point bending.



(a)



(b)

Figure 50. Illustrations of the (a) telemetry system mounted in the corpectomy model in the MTS and water. (b) A closer view of the same test fixture of the instrumented rod configured in the corpectomy model and MTS.

2.3.1.4 Cadaver Testing of the Final Housing

The spinal fusion system was implemented into a male cadaver approximately in his 70's. A posterior incision was made along the midline of the lumbar vertebrae and pedicle screws were placed in the L2 and L5 vertebrae. Normally during surgery, pedicle screws are placed in adjacent vertebrae, but due to the large size of the system a larger span was required. Figure 51 shows the system secured in the pedicle screws in the cadaver. The large black ring is the hand held reader for the system.

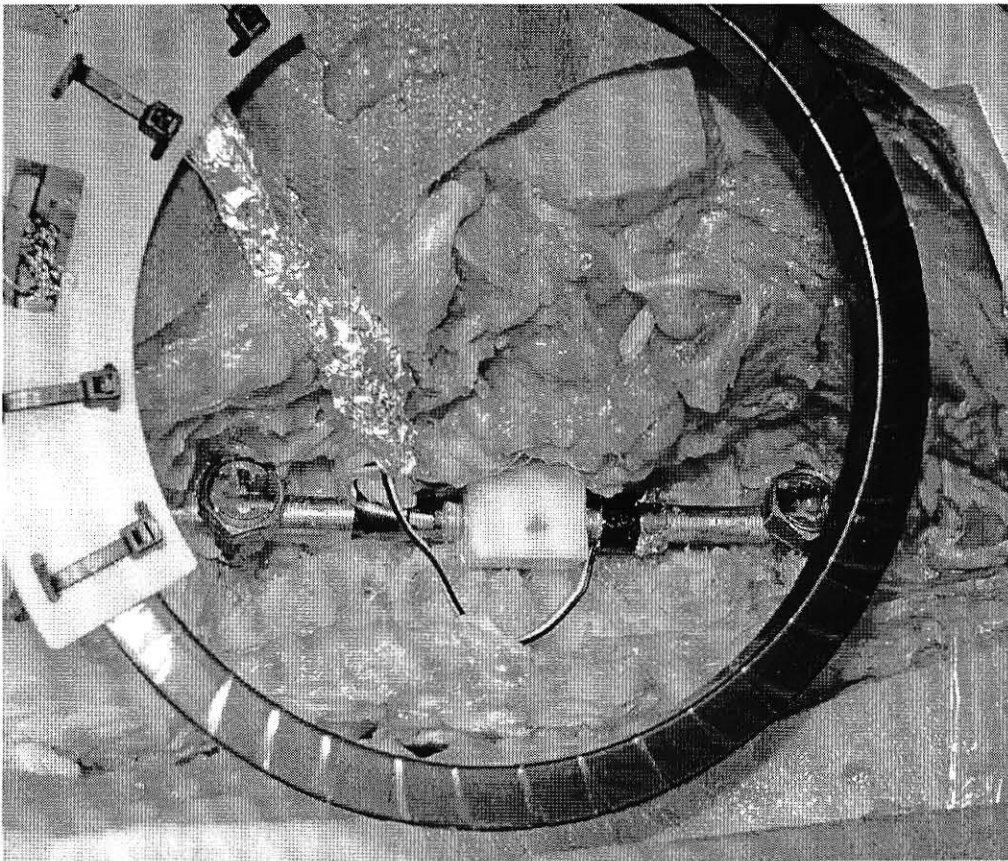


Figure 51. The strain monitoring system secured in the pedicle screws placed in L2 and L5 vertebrae of the cadaver spine.

The reader inductively powered the internal telemetry components of the strain monitoring system by transmitting a baseline frequency of 2404 Hz. Strain on the rod

induced a frequency shift in the telemetry system, which was correlated to the bending strain occurring on the implanted rods. Aluminum foil was placed on the strain gage wires leading from the rod to minimize noise. Not shown in Figure 51 is the opposing rod on the other side of the vertebrae outfitted with a rosette gage, which also spanned L2 to L5. Two rods were used in the procedure to distribute load applied to the lumbar spine.

Reference data were taken while the cadaver remained in the prone position. Two people on either the side of the cadaver raised the body approximately eight inches from the table and held the position approximately fifteen seconds. Seven channels of strain data and frequency were collected from the telemetry system at a rate one sample every two seconds. However, due to equipment limitations only four strain channels were low-pass filtered to remove unwanted high frequency noise.

2.3.2 Results

Illustrated in this section are results from the ABAQUS finite element model, which shows the strain results developed from the model as they appear on the rod and housing during bending. Of particular interest was the profile of the strain across the sensor surface of the housing and if the strain was amplified. The results also determined the most effective clamping pressure.

The results from MTS testing were used to validate the finite element model of the housing. The housing strain was compared to the rod strain to determine percent

strain transfer. Finally, water tank and cadaver testing results are used to show that the housing functioned properly.

2.3.2.1 ABAQUS Finite Element Modeling Results

The longitudinal strain developed on the housing and rod in the 3 axis direction is shown in Figure 52. Values shown in red are approximately $1000 \mu\epsilon$. Gray areas show strain magnitudes exceeding $1000 \mu\epsilon$, which occurs on the sensor surface of the housing and near the end of the rod, where concentrated loads were applied to produce bending in the rod.

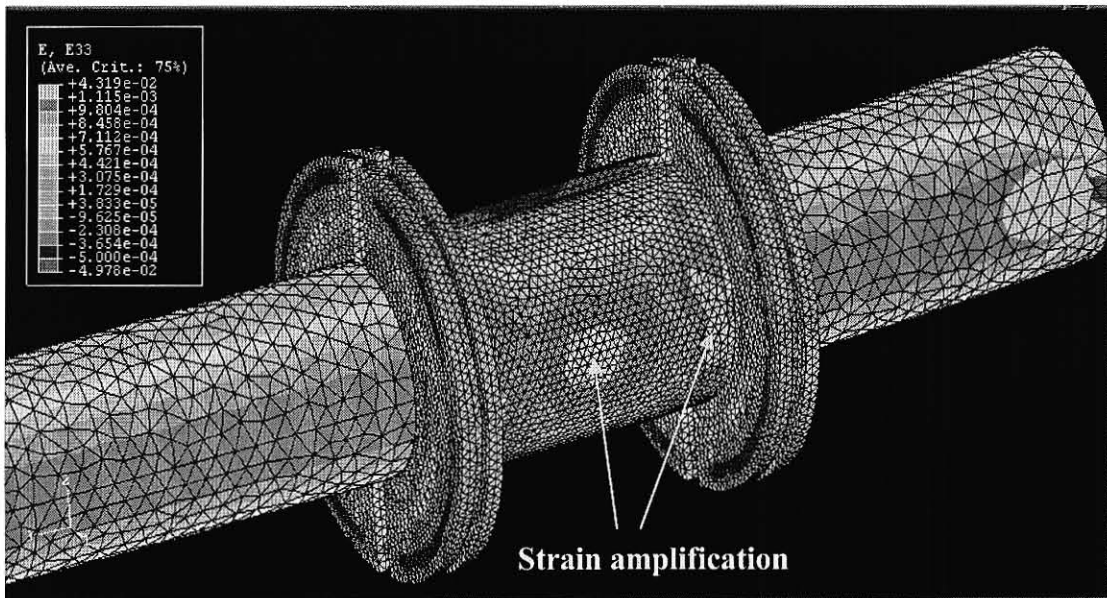


Figure 52. ABAQUS longitudinal strain graphical results from the FEA model.

All nodal points on the rod and housing were probed for strain magnitudes in the area where the MEMS-based capacitive strain sensor would reside. Figure 53 shows the percent strain transfer for these nodal values from the sensor surface for each housing design.

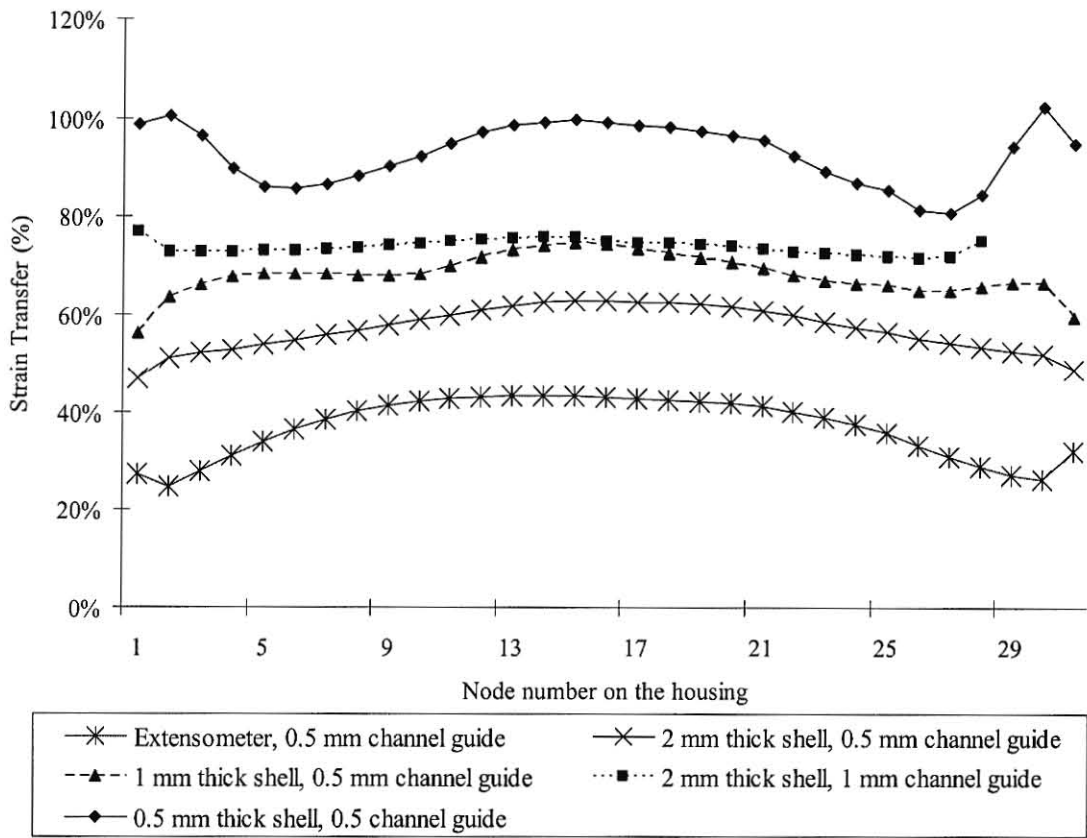


Figure 53. Strain transfer values for each of the housing designs.

The percentage of rod strain transfer from Figure 53 was averaged and the result for each housing design is shown in Table I.

Design	Channel Width	Clamping Pressure	Percentage of strain transfer from the rod to the housing
Extensometer	0.5 mm	10 MPa	36.96%
2 mm thick shell	0.5 mm	10 MPa	57.31%
1 mm thick shell	0.5 mm	10 MPa	68.57%
2 mm thick shell	1.0 mm	10 MPa	74.13%
0.5 mm thick shell	0.5mm	10 MPa	93.17%

Table I. Percentage of strain transfer for each housing design modeled in ABAQUS.

The effect of clamping pressure related to strain transfer percentage was evaluated by increasing the normal pressure exerted on the channel surface of the FEA model. Figure 54 shows rod strain transfer percentages for nodal values occurring across the housing's sensor surface. The strain sensor would be placed between nodes 5 and 25.

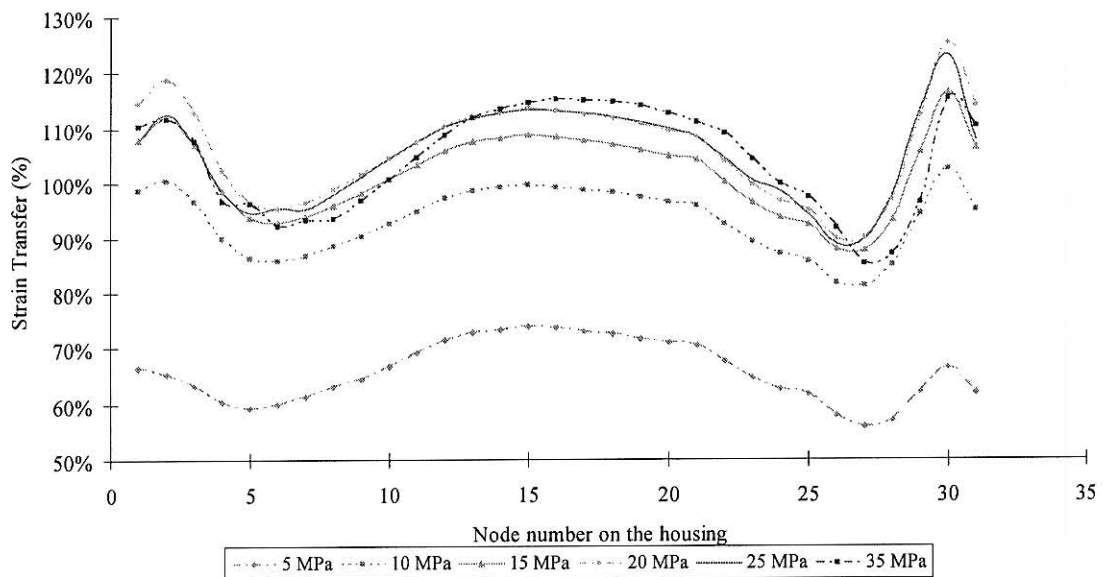


Figure 54. Data revealing percentage strain levels across the longitudinal plane of the sensor surface showing the location of best amplification.

Figure 55 shows the percentage rod strain transfer for various clamping pressures to determine which clamping pressure would give the highest strain transfer.

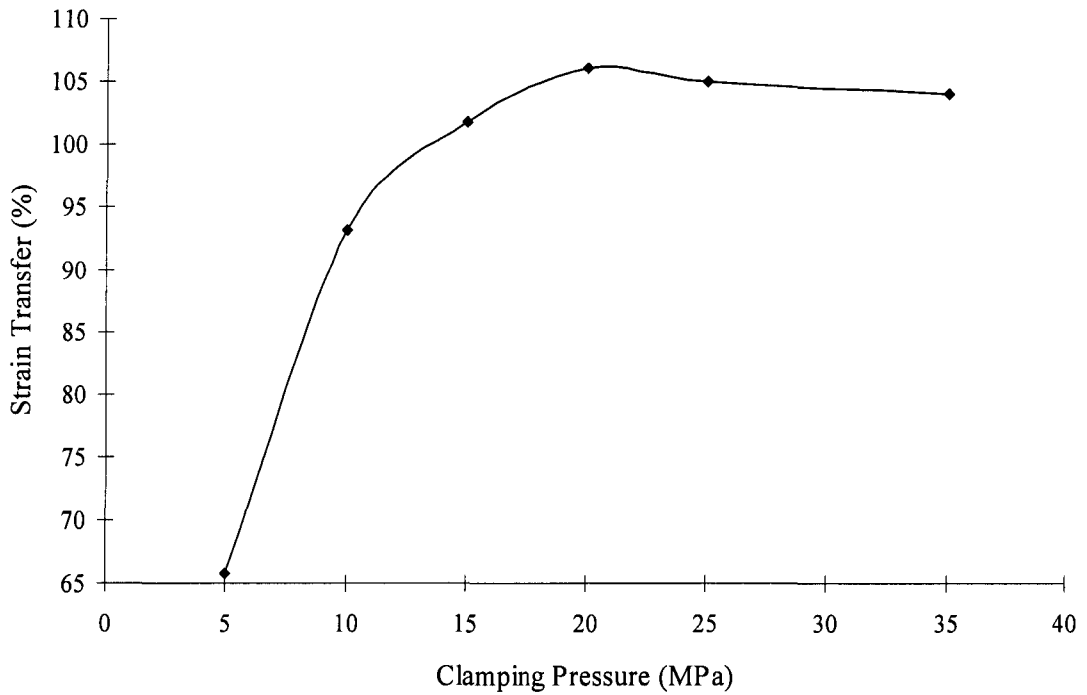


Figure 55. Graphical data showing the optimal clamping pressure for the 0.5 mm shell housing design.

Maximum rod strain transfer occurred at a clamping pressure of 20 MPa for 1000 $\mu\epsilon$. However, verification was needed that this value would transfer approximately 100% rod strain at values other than 1000 $\mu\epsilon$. Strain values lower than 1000 $\mu\epsilon$ were applied to the rod using the same clamping pressure of 20 MPa. Figure 56 shows the probed housing strain values under different applied strains on the rod and Figure 57 shows the percentage of rod strain transfer occurring at each nodal value.

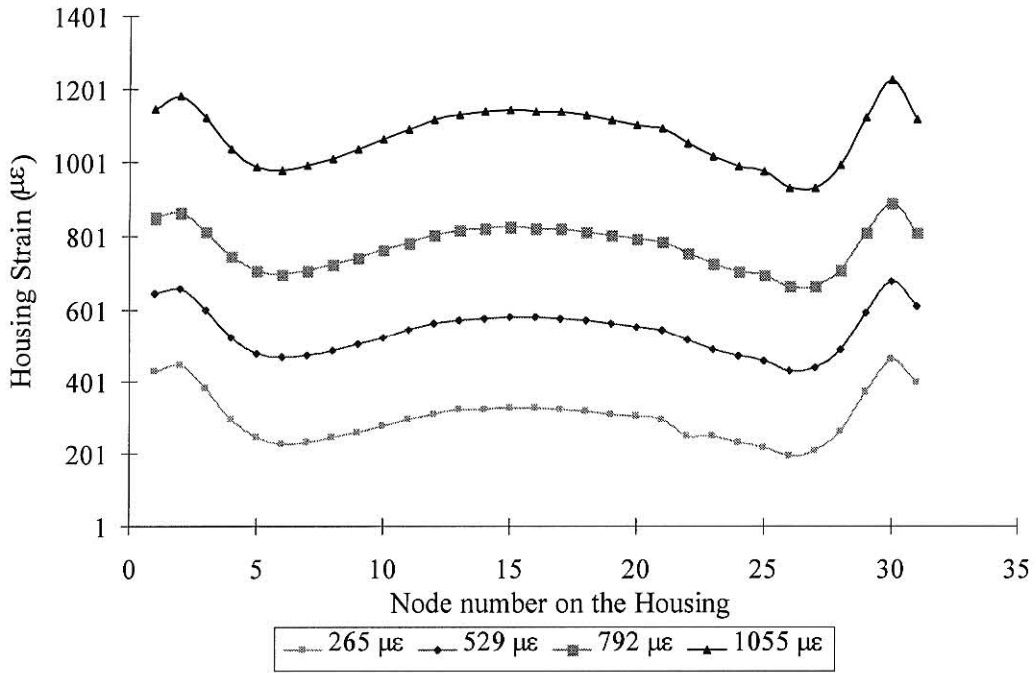


Figure 56. Strain modeling results from ABAQUS for the housing clamped at 20 MPa.

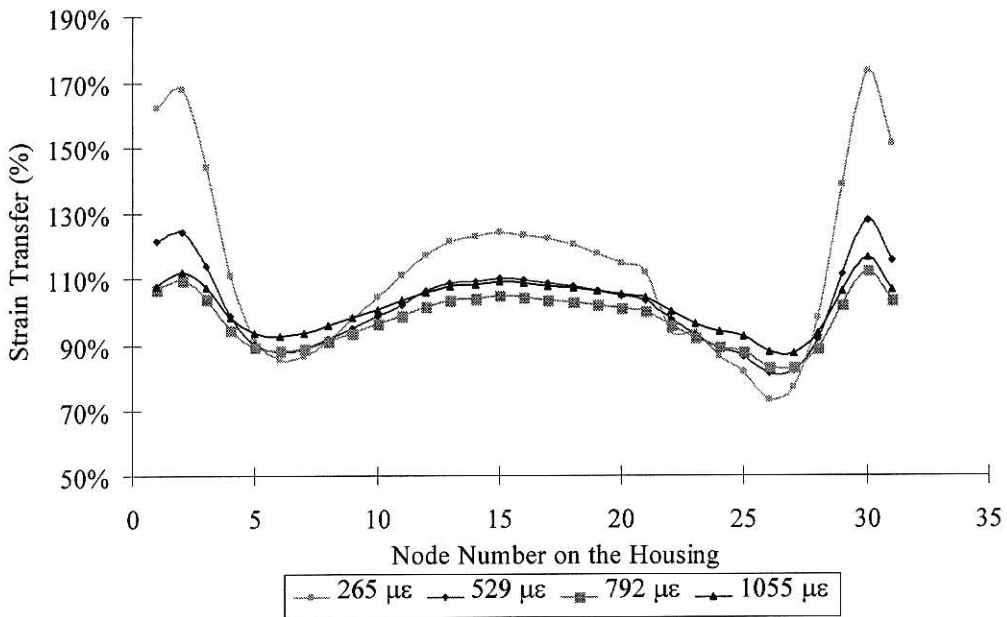


Figure 57. Strain modeling results from ABAQUS showing the percentage of strain transfer compared at different bending strain values.

Table II shows the averaged percentage of rod strain transfer for nodes 5 through 25.

Clamping Pressure	Rod Bending Strain	Average Percentage of strain transfer
20 MPa	265 $\mu\epsilon$	113.55%
20 MPa	529 $\mu\epsilon$	102.11%
20 MPa	792 $\mu\epsilon$	97.81%
20 MPa	1055 $\mu\epsilon$	101.89%

Table II. Strain transfer percentages from different levels of bending strain at 20 MPa of clamping pressure.

2.3.2.2 MTS Testing Results of the Final Housing

The housing was fabricated from PEEK and tested in the MTS using both static and dynamic loads. The results for the static test are shown in Figure 58.

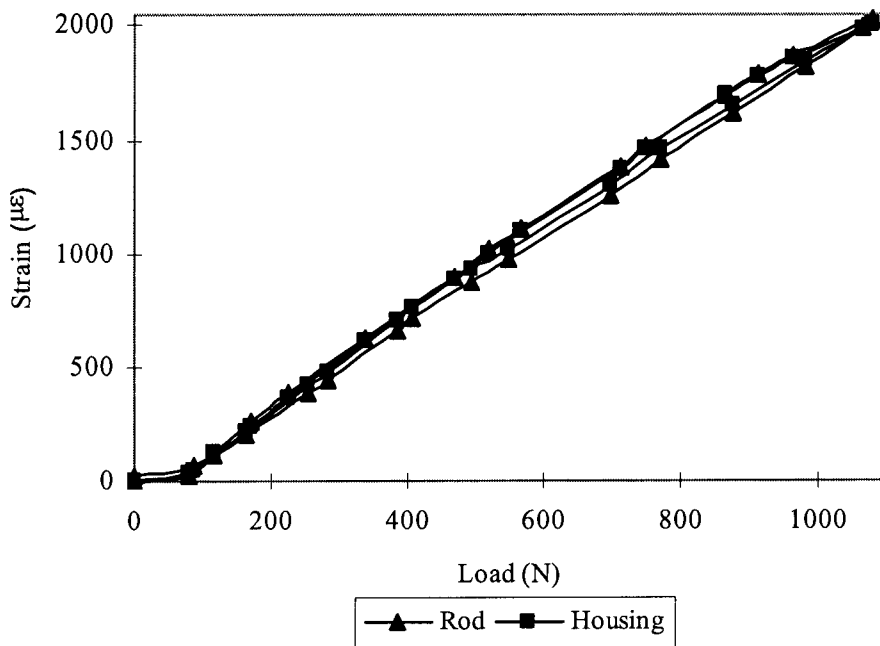


Figure 58. Manual MTS testing results from the bar before initiating cycle testing.

A cyclic load was applied to the rod in the MTS and maximum values from each cycle were collected and shown in Figure 59.

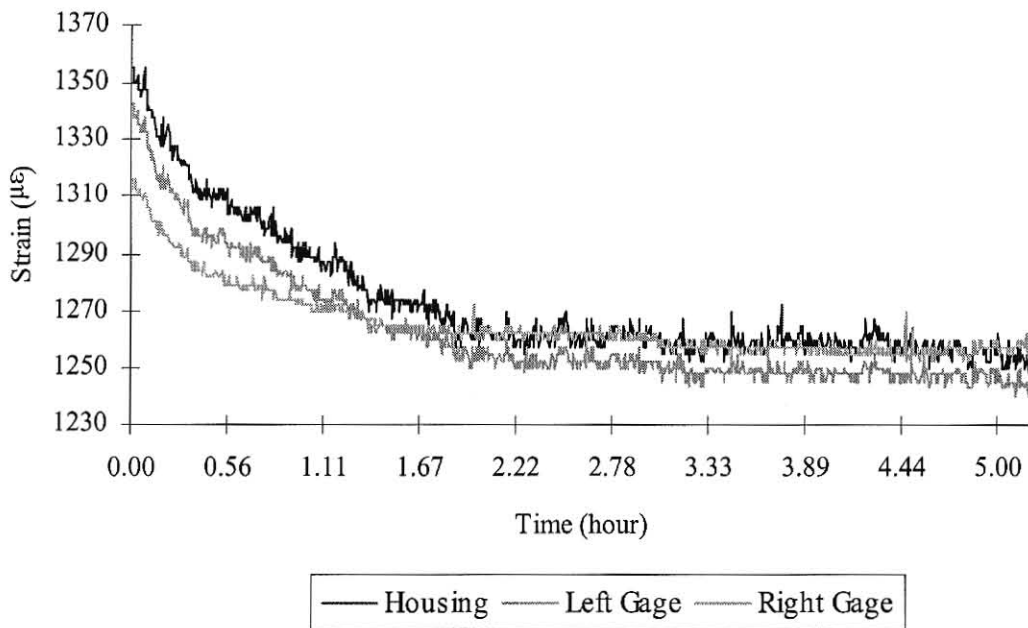


Figure 59. Maximum strain values collected from each cycle during the MTS cycle test.

A constant static load was applied to the rod to investigate whether the housing strain data would drift over a period of time. Once the static load was applied to the rod, strain data from the rod gages and housing were recorded with the results shown in Figure 60.

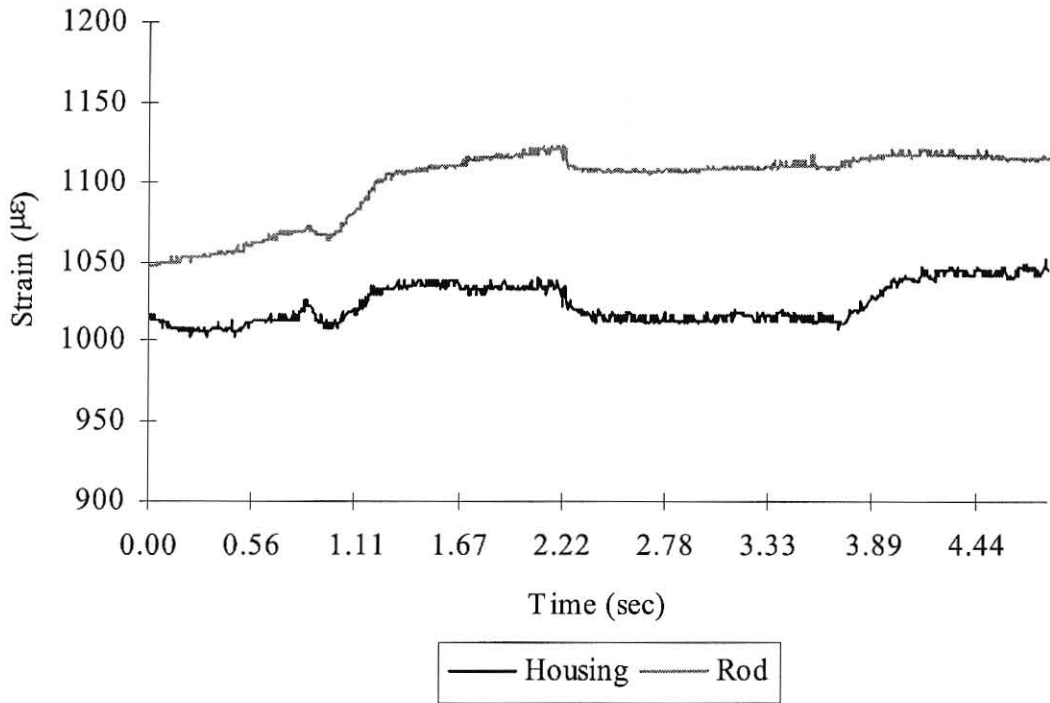


Figure 60. Static strain testing of the rod and housing.

2.3.2.3 Water Tank Testing Results of the Final Housing

The instrumented rod was calibrated by placing the rod in a cantilever fixture and applying known loads to one end. Rod strain and the corresponding frequency transmitted from the telemetry system were recorded to form the calibration curve shown in Figure 61.

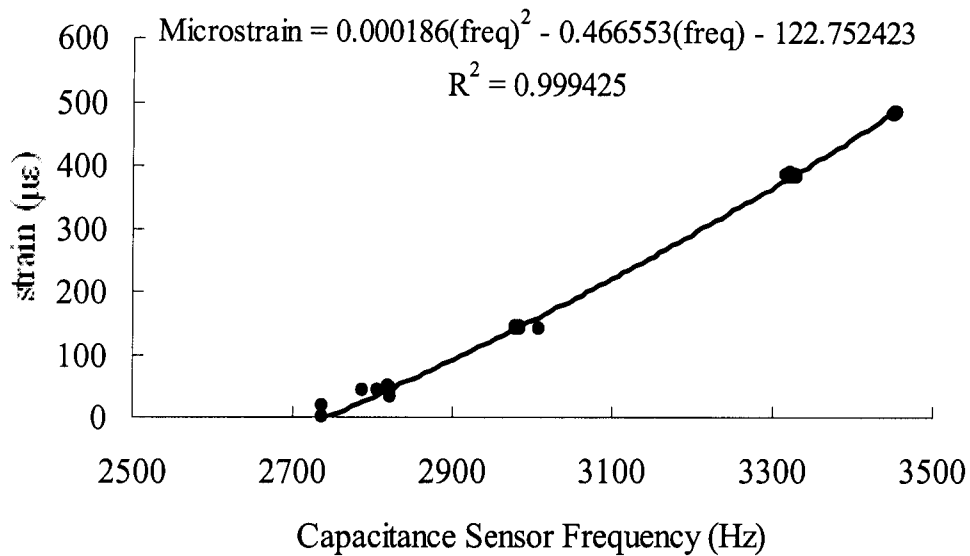


Figure 61. The calibration curve generated from cantilever bending of the telemetry system.

After the system was prepared and submerged in the water tank the transmission distance was measured and met the system constraint of 150 mm. However, a small amount of water leakage past the outer cover was observed after being submerged by the system for several hours due to a considerable capacitance change exhibited by the sensor at a static MTS load. The system was dried and the cover was sealed again using polyurethane, which prevented any further leakage.

Frequency values gathered during water tank testing were converted to corresponding strain values using the calibration curve from Figure 61 and are shown in Figure 62. This figure shows the strain values from the foil strain gage on the telemetry rod and converted strain values from the telemetry system. Loads were applied in a stair-step configuration by the MTS to demonstrate that the spinal fusion system functioned properly.

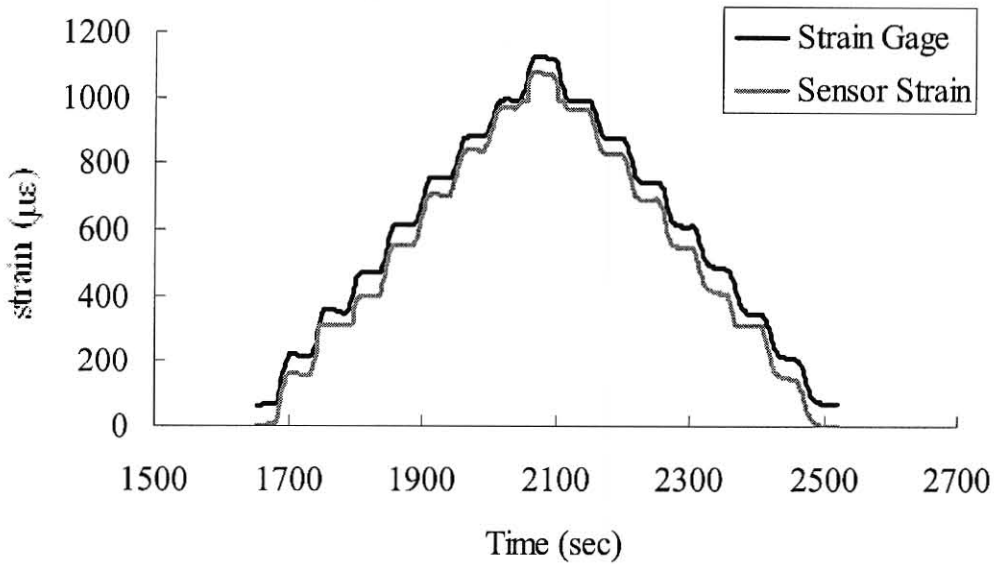


Figure 62. Comparison of the foil strain gage measurements and converted frequency to strain values in the corpectomy model, while submerged in water tank.

2.3.2.3 Cadaver Testing Results of the Final Housing

Functionality of the spinal fusion monitoring system was verified using a cadaver. Filtered longitudinal strain data from both rods and the frequency data were recorded while manipulating a cadaver, as seen in Figures 63 and 64. Data from the two opposing rods are different in magnitude, but changes occur simultaneously and the strain differential remains the same throughout the test. The frequency data follows a similar pattern of change compared to the rod strain.

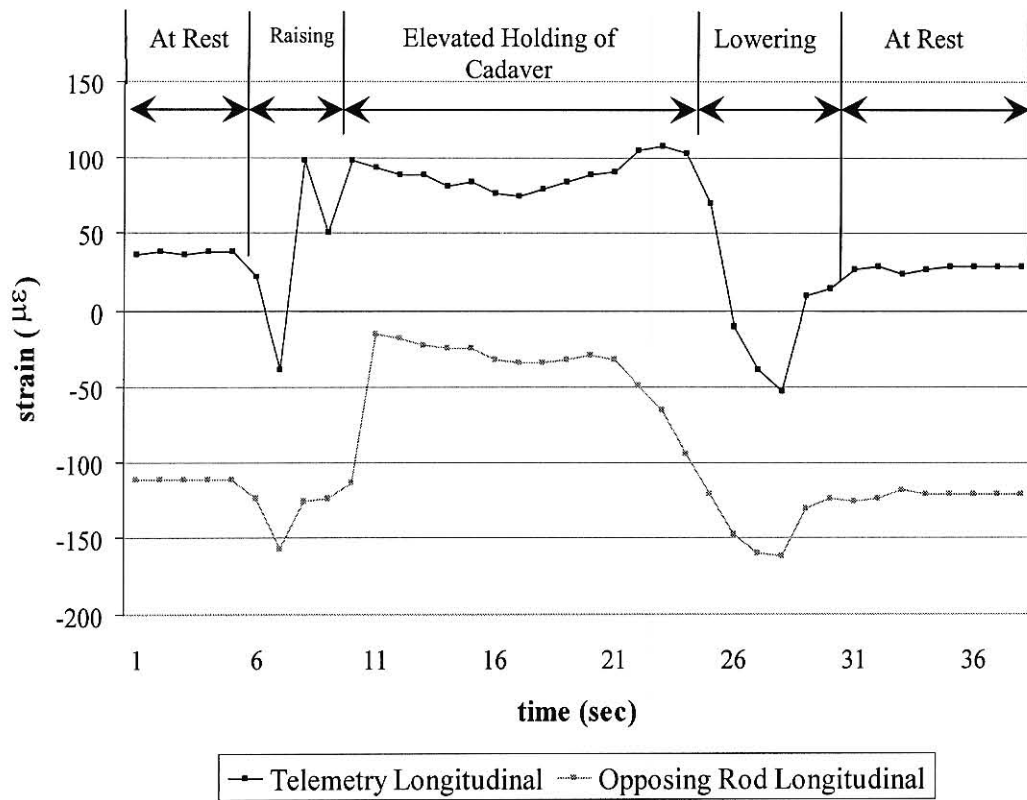


Figure 63. Cadaver testing showing longitudinal strain on both rods.

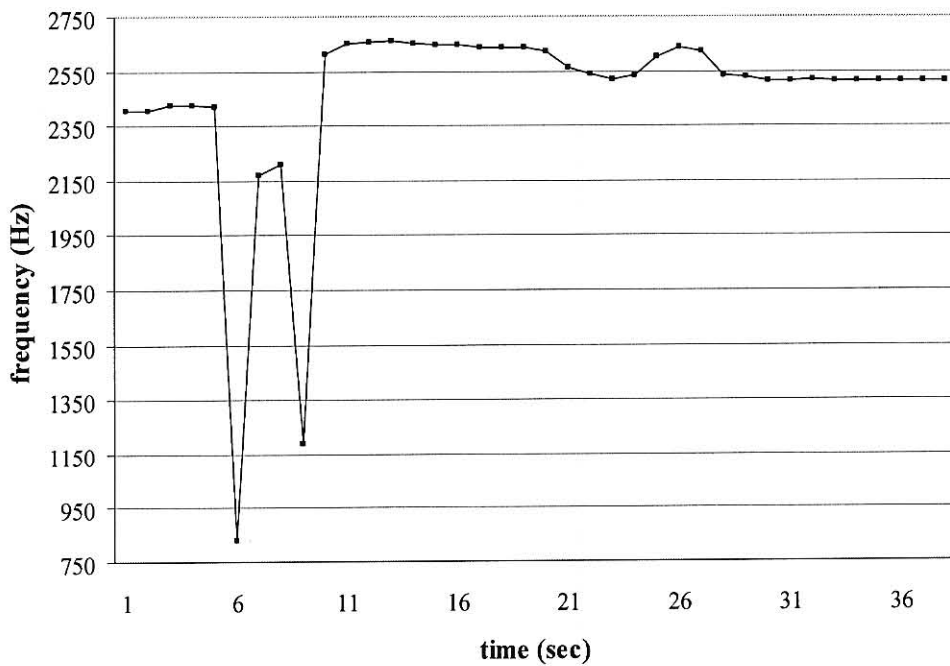


Figure 64. Frequency data gathered from cadaver testing.

2.3.3 Discussion

2.3.3.1 ABAQUS Finite Element Model Discussion of the Final Housing

The finite element model showed housing strain results fluctuating noticeably across the sensor surface resulting in comparable and amplified rod strain values. Amplification occurred in the middle region where the sensor would reside and near the cable guides. The results were encouraging and showed that adequate clamping pressure would result in strain transfer percentage exceeding 100%.

The 0.5 mm thick shell housing with 10 MPa of clamping pressure produced an averaged strain transfer of 93.17%, which fell below the established criteria for the system. A thinner shell design was not selected due to possible degradation of the housing's ability to be robustly manufactured.

Figure 55 shows that maximum strain transfer occurred at a clamping pressure of 20 MPa for the 0.5 mm shell design with the highest strain amplification value of 113.70% in the middle of the longitudinal plane of the sensor surface. Variation of symmetry occurs from the strain curves from Figure 56 and is attributed to small discrepancies associated with mesh generation for each model. The clamping pressure of 20 MPa was ideal for 1000 $\mu\epsilon$, however, Figures 56 and 57 depict the housing's strain transfer efficiency at other strain levels were consistent throughout the 0 to 1000 $\mu\epsilon$ strain range.

An exception is noted for the 265 $\mu\epsilon$ data where strain transfer percentage was slightly elevated. Table II information shows that the housing transmits approximately

100% or more of the rod strain at all levels throughout the strain range. As a result, the 0.5 mm thick shell housing design was chosen for its highest percentage of strain transfer and for the thin cable channel, which allowed adequate space for the sensor and telemetric components.

However, the poor performance of the extensometer design was attributed to the physical boundary conditions controlling the amount of strain transfer. Figure 65 shows how the sensor surface would not conform to the surface of the rod or its radius of curvature, thereby producing longitudinal stretching or axial strain. Other design constructions revealed that the inner and outer sensor surfaces conformed to the radius of curvature of the rod due to normal pressure exerted by the cable onto the wire guides.

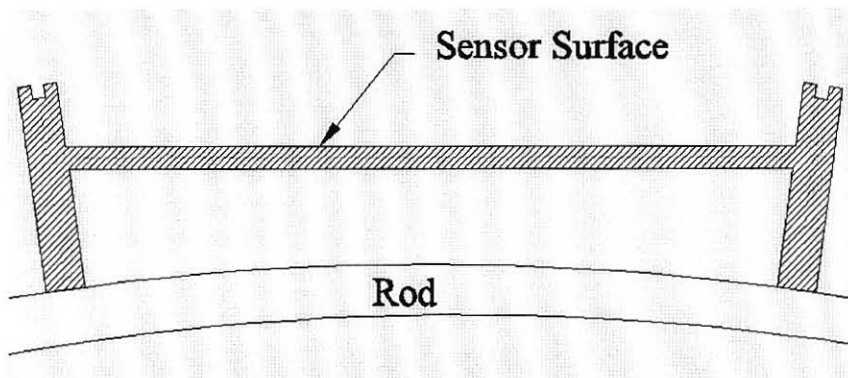


Figure 65. A pictorial demonstrating the extensometer sensor surface undergoing longitudinal strain deformation. This deformation does not undergo bending strain or conform to the rod surface. The darkened area represents the cross-section of the upper half of the housing.

2.3.3.2 MTS Final Housing Design Discussion

Figure 58 shows that the response of the housing during MTS testing was comparable to the rod. Housing strain slightly exceeded the rod strain confirming a small amount of amplification. In addition, the results were repeatable with no evidence of hysteresis.

The MTS cycle test from Figure 59 shows an initial decay of all three strain signals from the rod and housing. This occurrence was attributed to the system achieving steady state in the MTS. Strain behavior of the housing and gages on the rod were similar even when steady state was achieved. However, the housing strain was amplified due to the 0.5 mm thickness of the housing and increased distance from the neutral axis of the rod to the sensor surface of the housing.

Figure 60 demonstrates the housing response to a static load to determine if drift would occur over a period of time. During this test the rod strain was larger in magnitude than the housing strain. This was attributed to a malfunction of one of the strain gages adjacent to the housing, which were used to verify a constant magnitude of strain across the surface of the rod. Therefore, it could not be determined if the MTS applied the same load on both ends of the test rod. The result allowed application of slightly different loads on each end of the rod developing a strain gradient rather than a constant magnitude of strain across the surface of the rod. However, static testing could still reveal if degradation occurred from the housing strain signal. From Figure 60 the strain differential between the rod and housing remained constant throughout the test after an

initial settling period. Strain variation from both signals was also noticed during the test, which was attributed to small load changes from the MTS.

2.3.3.3 Water Tank Testing Discussion

Functionality of the telemetry system during water tank testing was supported by two important items gathered during testing. The first item confirmed that the telemetry system transmitted frequency data more than 150 mm to an external reader while submerged in water. Additionally, graphical data from Figure 62 demonstrates that the converted frequency data was comparable to the rod strain at all selected loads, without evidence of hysteresis.

2.3.3.4 Cadaver Testing Discussion

Functionality of the telemetric strain monitoring system was presented in Figures 63 and 64 where filtered longitudinal strain data from both rods and the frequency data were presented. Ideally, the data from the two longitudinal strain gages on either rod should have been similar in magnitude. However, an approximate 150 $\mu\epsilon$ differential occurred between the two rods giving evidence that they were not loaded equally. This may be a normal occurrence within the body or could have been attributed to unintentional errors during testing.

As the body was raised from the table the sensor was placed in compressive bending strain for a moment and caused the strain sensor to short circuit. This is seen

from the frequency graph of Figure 64, where a momentary non-reading occurred between 6 and 11 seconds. However, during elevation, lowering and resting portions of the test the rods were exhibiting tensile strain. As a result, the frequency data followed a similar pattern compared to the strain data, but the amount of change was not as dramatic as the strain data. This was attributed to different response characteristics of the linear strain gages as compared to the parabolic capacitive strain sensor.

3.0 MEMS-BASED CAPACITIVE BENDING STRAIN SENSOR

Components of the spinal fusion system are the housing, telemetry circuitry and a microelectromechanical systems (MEMS) based capacitive bending strain sensor.

MEMS are the integration of mechanical elements, sensors, actuators and electronics on a common silicon substrate. Components are produced using compatible micromachining processes that selectively etch or add structural layers to add mechanical or electromechanical devices [53].

A solution was needed that could be implanted for the life of the patient, not require a power source, be wireless and eliminate potential exploratory surgeries. As a result a MEMS-based capacitive based strain sensor was considered that would be used with a passive telemetry system. Changes in bending strain could offer objective data to orthopaedic surgeons to determine if spinal fusion was occurring. The device would also offer rates of fusion progression and information whether fusion instrumentation had failed.

Presented within this section are the development, fabrication and results of a capacitive MEMS-based bending strain sensor. This type of sensor was selected for its ease of implementation in the telemetry circuitry. A minimum initial capacitance of 5 pF was required for the telemetry circuitry. An outside reader would energize the internal system and strain values exhibited on the sensor would correspond to particular

frequencies received by the outside reader. Sensitivity for the system required the sensor to change 5 pF over the designated strain range of 0 to 1000 $\mu\epsilon$. Finite element analysis was implemented to understand and manipulate actuation of the sensor, while understanding the stress magnitudes developed by the sensor. Four-point bending was performed on the sensor, with results analyzed to determine behavioral characteristics and sensitivity.

3.1 Sensor Literature Search

Modern medical science has emerged with a need to monitor physiological functions (i.e. intravascular pressure, intraocular pressure, etc.) [54-57]. MEMS devices have been a growing part of the medical device industry since the 1980's [58–62]. A variety of these monitoring devices require that their tasks be performed wirelessly and implanted for indefinite terms to allow patient mobility, continuance of daily activities and avoidance of costly surgeries to remove the systems after utilization is complete. These necessities negate the use of a battery and limit the types of materials used for long-term biocompatibility.

Comb drives or systems using interdigitated fingers for variable capacitors, electrostatic actuation and frequency tuning have become integral parts of microelectromechanical system (MEMS) devices in an emerging technology for RF and wireless communications [63-76]. Due to needs of the telemetry system, interdigitated fingers were investigated for their ability to offer a variable capacitive output.

3.2 Preliminary Sensor Approach

The initial sensor design involved selection of materials for the MEMS-based sensor, analytical calculations, preliminary design, sensor modeling using CoventorWare and ABAQUS finite element software, fabrication and testing. These areas are covered in the next section along with discussion and conclusions based upon the preliminary design.

3.2.1 Preliminary Sensor Materials and Methods

Analysis of the sensor began by understanding the deformation of the rod. Based upon this information initial sensor designs were modeled using CoventorWare software with additional modeling using ABAQUS software.

Sensors were fabricated to develop an interdigitated circular array that would develop an increase in capacitance while undergoing increased tensile strain. Once sensor fabrication was complete it was placed on a cantilever beam where strain was manually induced and behavior was visually observed.

3.2.1.1 Sensor Change of Length Calculations and Capacitance Relationships

The main function of the sensor was to change capacitance, while attached to a rod or beam experiencing bending strain. Analysis of the rod was required to understand deformation of the rod and its angular displacement. Figure 66 represents rod

deformation under pure bending where L is the length of the rod, δ is the change in length of the rod, ρ is the radius of curvature, θ is angular curvature and c is the radius of the rod. Deformation and the change in rod length is small, therefore, sensitivity of the sensor throughout the entire strain range was an important consideration during the design process. A method to mechanically amplify small deformations was sought to increase the sensor's sensitivity.

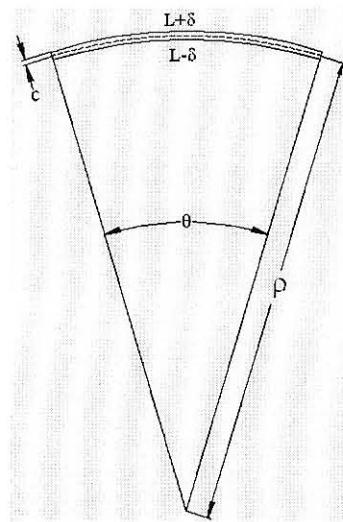


Figure 66. Spinal rod undergoing bending.

From prior research, a discectomy was performed on an excised spine from a cadaver, which was constrained and loaded in a Material Testing System (MTS) to simulate a 113.4 kg patient. Experimental results gave maximum bending strains at approximately $1000 \mu\epsilon$ [5]. The change in length of the rod's upper surface, δ , was required to determine the initial gap of the fingers of the comb drive to avoid touching of the fingers or sensor continuity. The relationship between the angle of curvature, rod length and the radius of curvature [77] is given by

$$\theta = \frac{L}{\rho} = \frac{L + \rho}{\rho + c} = \frac{L - \rho}{\rho - c} \quad (5)$$

where θ is the angle of curvature, L is the rod's length and ρ is the radius of curvature.

The ratio of the rod's radius to the radius of curvature as it relates to bending strain is given by

$$\frac{c}{\rho} = \frac{\delta}{L} = \varepsilon = \frac{\sigma}{E} = \frac{Mc}{EI} \quad (6)$$

where M is the applied bending moment, E is Young's modulus for 316L stainless steel and I is the area moment of inertia. The final relationship to determine the radius of curvature is given by

$$\frac{1}{\rho} = \frac{M}{EI} \quad (7)$$

Stainless steel 316L rods with a length of 38.10 mm, radius of 3.18 mm and a Young's modulus of 200 GPa were used as dimensional and material properties. A bending strain of 1000 $\mu\epsilon$ gave a radius of curvature of 3.175 m. The angle of curvature for the rod, θ_{rod} , was found to be 0.012 radians and its change in length, δ_{rod} , was 38.100 μm .

However, the length of the sensor was restricted to 10 mm due to spacing allowed by the sensor housing. The angle of curvature spanned by the sensor, θ_{sensor} , was calculated to be 0.003 radians, which gave a change in length for the sensor, δ_{sensor} , to be 10.0 μm .

The capacitance relationship for a parallel plate system, shown in Figure 67, is given by

$$C = \frac{\varepsilon_0 \varepsilon_r A}{d} \quad (8)$$

where C is generated capacitance in farads (F) and ϵ_0 is the dielectric of free space equal to 8.85×10^{-14} F/cm [78, 79]. The second dielectric constant, ϵ_r , is for the medium between the two plates and equal to 1 F/cm.

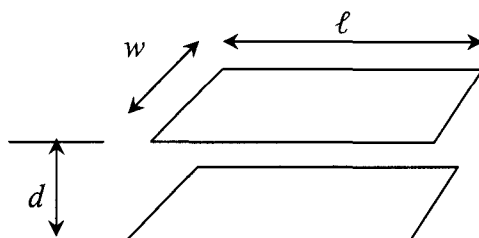


Figure 67. A parallel plate configuration.

The overlapping area between the two plates is A and d is the distance between the two plates [79]. From this relationship, increasing or decreasing the overlapping area of the plates would produce a linear difference in capacitance. Adjusting the spacing between the two plates would result a parabolic response. The sensor's response could be amplified by increasing the distance from the neutral axis of the rod to the sensor's plane of actuation. Another method of amplification was the use of lever arms and is the first approach used in the preliminary sensor designs.

3.2.1.2 Preliminary Sensor Designs

Figure 68a shows a lever arm arrangement derived from Lin [80] that would amplify a small change in length. Anchors were created to attach directly to the substrate with arms attached to the anchors and elevated above the substrate. As the substrate undergoes bending, a longitudinal strain occurs causing the anchors to move with the

substrate. As a result, the silicon arms deflect and the central lever arm moves angularly, as seen in Figure 68b.

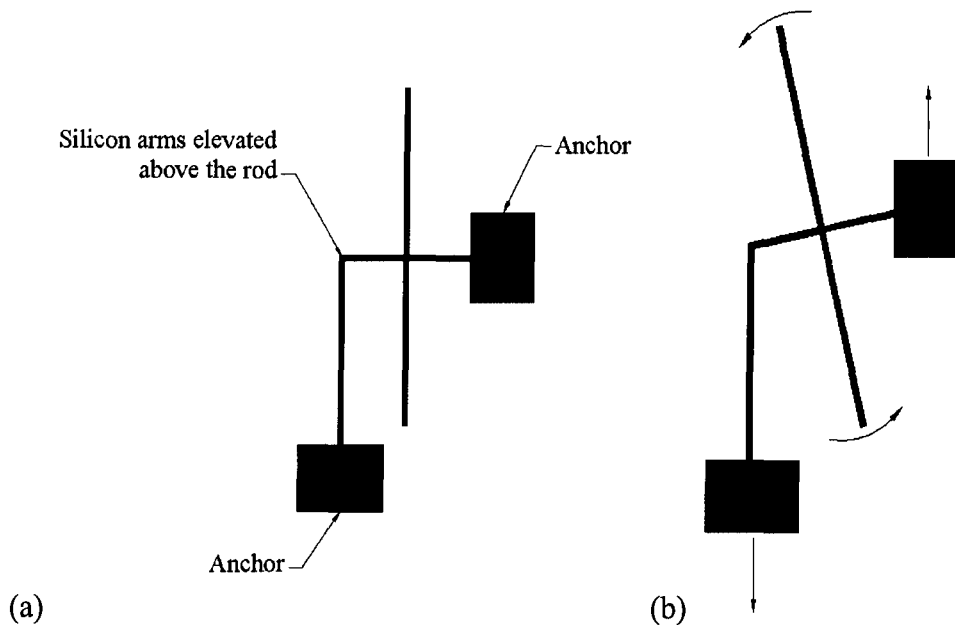


Figure 68. (a) Lever arm arrangement of the initial housing design. (b) Movement of the anchors and central lever arm, while undergoing bending strain.

Based upon this movement, the sensor was developed to take advantage of the change in spacing between parallel plates.

The initial design, or sensor 1, was an analytical approach to predict sensor movement with no modeling or finite element analysis (FEA). The design employed interdigitated fingers in an angular array with the fingers elevated above the substrate surface and the anchors attached to the bending substrate. During bending, it was anticipated that the sensor would move in a similar method as illustrated in Figure 68b. Output of the sensor would be a parabolic increase in capacitance.

3.2.1.2.1 CoventorWare Finite Element Modeling of Preliminary Sensors

Coventorware (Coventor, Cary, NC) was specifically developed for the analysis of MEMS devices and was used to model the sensor. Sensor displacement was used to calculate capacitance changes and stress analysis of the model was reviewed to make sure that the yield strength of silicon was not exceeded. The Maximum Normal Stress Criterion was used since silicon is a brittle material. This criterion states that failure occurs when the maximum principal stress reaches either the uniaxial tension strength or the uniaxial compression strength [77]. The yield strength or fracture strength of silicon to predict material failure is 7 GPa [81].

The isotropic material properties of single crystal silicon were calculated using the stiffness matrix [C] given by

$$C_{ij} = \begin{bmatrix} C_{11} & C_{12} & C_{13} & C_{14} & C_{15} & C_{16} \\ C_{21} & C_{22} & C_{23} & C_{24} & C_{25} & C_{26} \\ C_{31} & C_{32} & C_{33} & C_{34} & C_{35} & C_{36} \\ C_{41} & C_{42} & C_{43} & C_{44} & C_{45} & C_{46} \\ C_{51} & C_{52} & C_{53} & C_{54} & C_{55} & C_{56} \\ C_{61} & C_{62} & C_{63} & C_{64} & C_{65} & C_{66} \end{bmatrix} = \begin{bmatrix} 166 & 64 & 64 & 0 & 0 & 0 \\ 64 & 166 & 64 & 0 & 0 & 0 \\ 64 & 64 & 166 & 0 & 0 & 0 \\ 0 & 0 & 0 & 80 & 0 & 0 \\ 0 & 0 & 0 & 0 & 80 & 0 \\ 0 & 0 & 0 & 0 & 0 & 80 \end{bmatrix} \text{MPa} \quad (9)$$

The compliance matrix, where S_{ij} is defined as [S], was determined by

$$[S] = [C]^{-1} \quad (10)$$

where

$$\begin{bmatrix} 166 & 64 & 64 & 0 & 0 & 0 \\ 64 & 166 & 64 & 0 & 0 & 0 \\ 64 & 64 & 166 & 0 & 0 & 0 \\ 0 & 0 & 0 & 80 & 0 & 0 \\ 0 & 0 & 0 & 0 & 80 & 0 \\ 0 & 0 & 0 & 0 & 0 & 80 \end{bmatrix}^{-1} = \begin{bmatrix} 0.0077 & -0.0021 & -0.0021 & 0 & 0 & 0 \\ -0.0021 & 0.0077 & -0.0021 & 0 & 0 & 0 \\ -0.0021 & -0.0021 & 0.0077 & 0 & 0 & 0 \\ 0 & 0 & 0 & 0.0125 & 0 & 0 \\ 0 & 0 & 0 & 0 & 0.0125 & 0 \\ 0 & 0 & 0 & 0 & 0 & 0.0125 \end{bmatrix} \quad (11)$$

Results from the stiffness matrix support that silicon behaves as an isotropic material and only values from each normal direction were required for the finite element model [79]. Young's moduli E_{11} , E_{22} and E_{33} , were determined by calculating the reciprocal of each value in the compliance matrix where

$$E_{ii} = \frac{1}{C_{ii}} = \frac{1}{0.0077} = 129.87 \text{ GPa}, i = 1 \text{ to } 3 \quad (12)$$

The calculated Young's moduli values were confirmed for <100> oriented silicon [82].

A design that exhibited a series of interdigitated semi-circle fingers, or sensor 2, where the overlapping areas changed to create a change in capacitance, is shown in Figure 69. To gain further amplification from the small movement occurring on the beam, the anchor separation distance was increased. The length of the central lever arm and circular fingers were lengthened as much as possible to meet the initial capacitance requirements within the allowable space. To actuate the sensor, the bottom of each anchor was displaced $0.90 \mu\text{m}$ away from each other. Angular movement of the circular fingers developed an increase in capacitance due to the increased area between the fingers. Figure 69 shows the magnitude of the displacement of sensor 2 as an increasing gradient originating from the center to the outside perimeter. The largest magnitude of displacement by the sensor occurred on the outermost rings with $40 \mu\text{m}$ of movement. Initial capacitance of sensor 2 was 12.09 pF and 12.30 pF after actuation. The telemetry circuitry required the sensor to generate a minimum capacitance of 5 pF with a minimum differential of 5 pF . The differential of 0.21 pF for sensor 2 did not meet the requirements of the telemetry circuitry. However, modeling the sensor avoided the waste of materials, chemicals, machine utilization and time in the cleanroom.

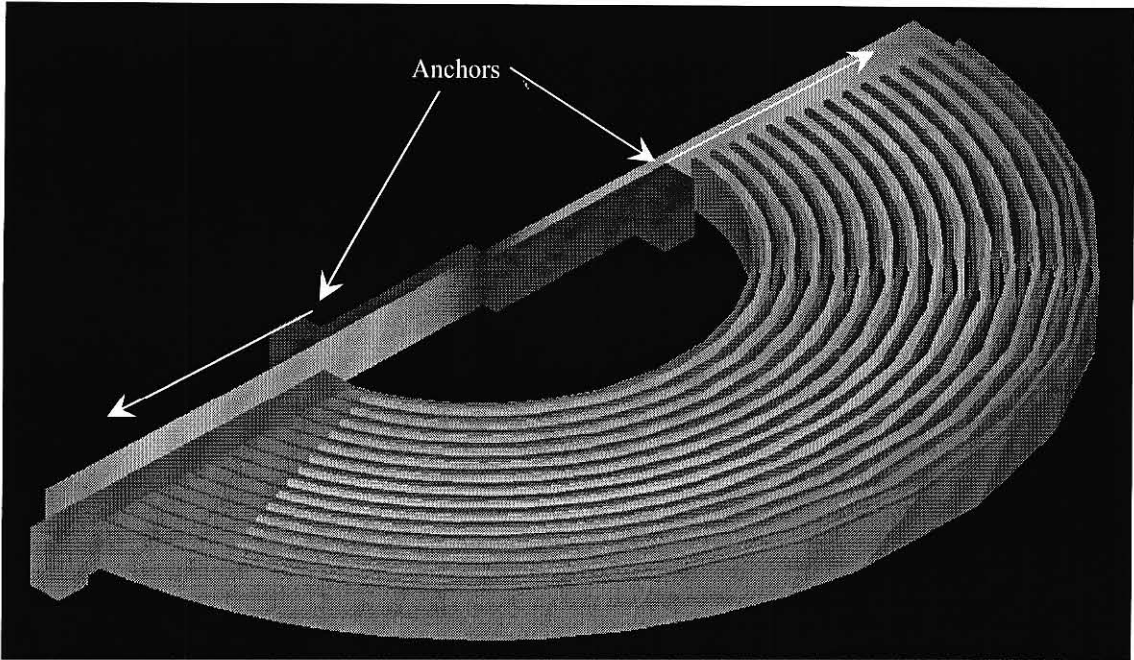


Figure 69. The displacement gradient of a model developed in CoventorWare utilizing change in overlapping area between plates.

Due to successful movement of the sensor 2, shown in Figure 69, but lack of capacitance change, a new sensor, which incorporates an angular array of interdigitated fingers and offset anchors to maximize amplification of the central lever arm, as shown in Figure 70, was designed. Also, the number of fingers was increased from 58 to 69 with a length of $1250\ \mu\text{m}$ and spacing of 60 and $100\ \mu\text{m}$ between the fingers. The initial capacitance of the sensor in the unstrained state was $5.04\ \text{pF}$ and met the initial requirements for the telemetry system. Sensor 3 was meshed using parabolic tetrahedrons with a minimum element size of $200\ \mu\text{m}$, as shown in Figure 70.

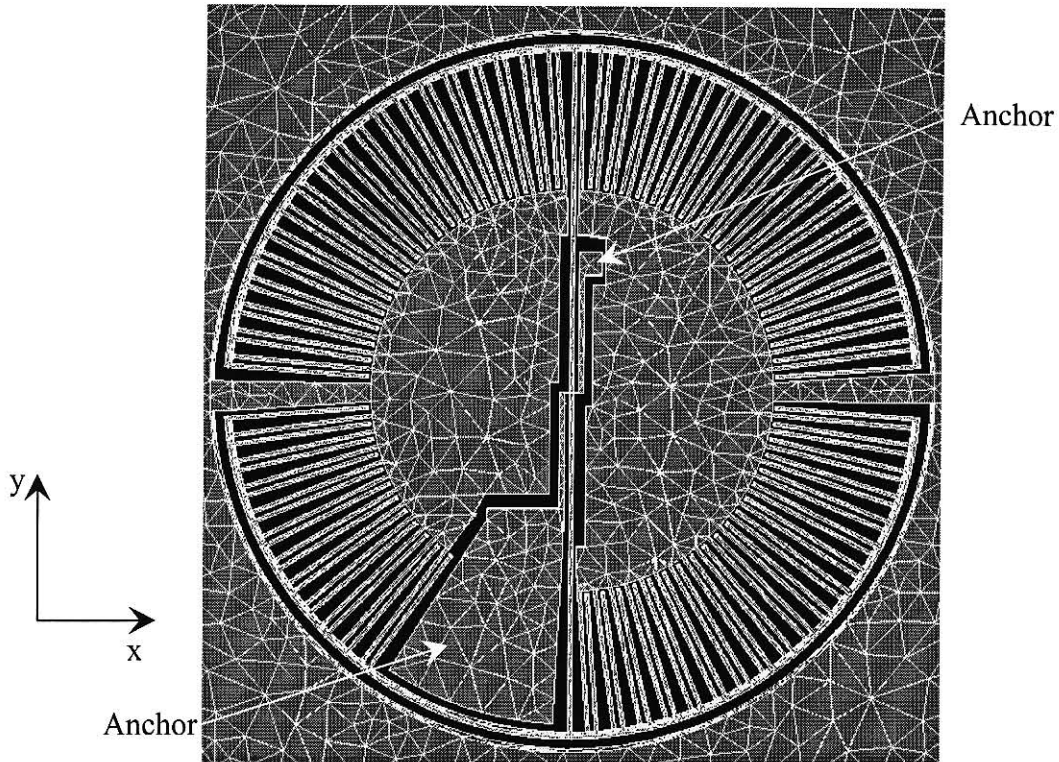
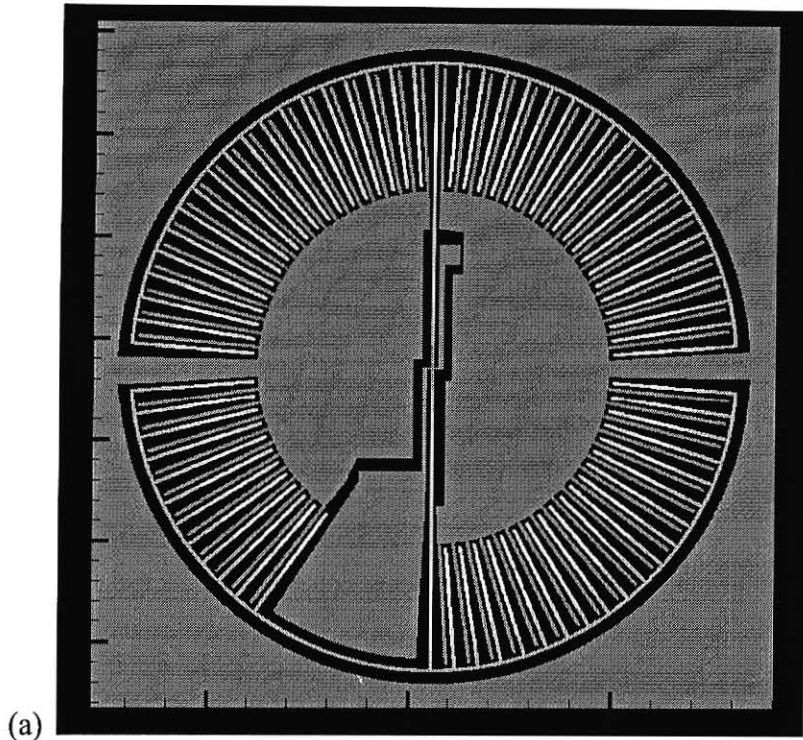
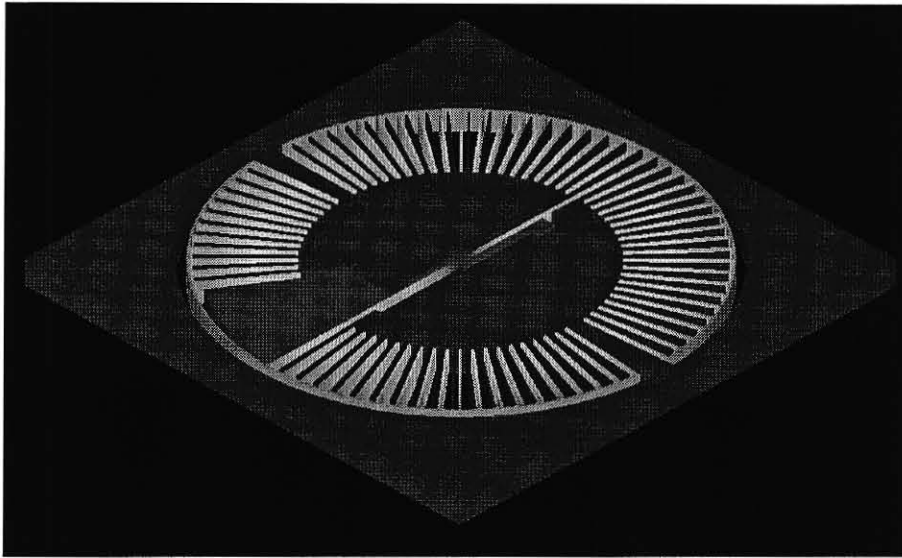


Figure 70. The mesh generated in CoventorWare for the second model using parabolic tetrahedrons.

The upper anchor was displaced $0.90 \mu\text{m}$ in the y-axial direction and the lower anchor was displaced -0.90 in the same direction to actuate the sensor. Figure 71 shows magnitude of displacement from the model for sensor 3.



(a)



(b)

Figure 71. Magnitude of the displacement of the sensor after actuation in the (a) front and (b) isometric views.

Coventorware results showed that the model of sensor 3 did move as intended and generated the capacitance required. The principal stresses occurred in the middle of the central lever arm where it attached to the satellite arms of the anchor. The principal

stresses in each direction shown are $\sigma_1 = 284.60$ MPa, $\sigma_2 = 89.60$ MPa and $\sigma_3 = 89.60$ MPa, as shown in Figure 72. None of the stresses exceeded the fracture strength of silicon at 7 GPa.

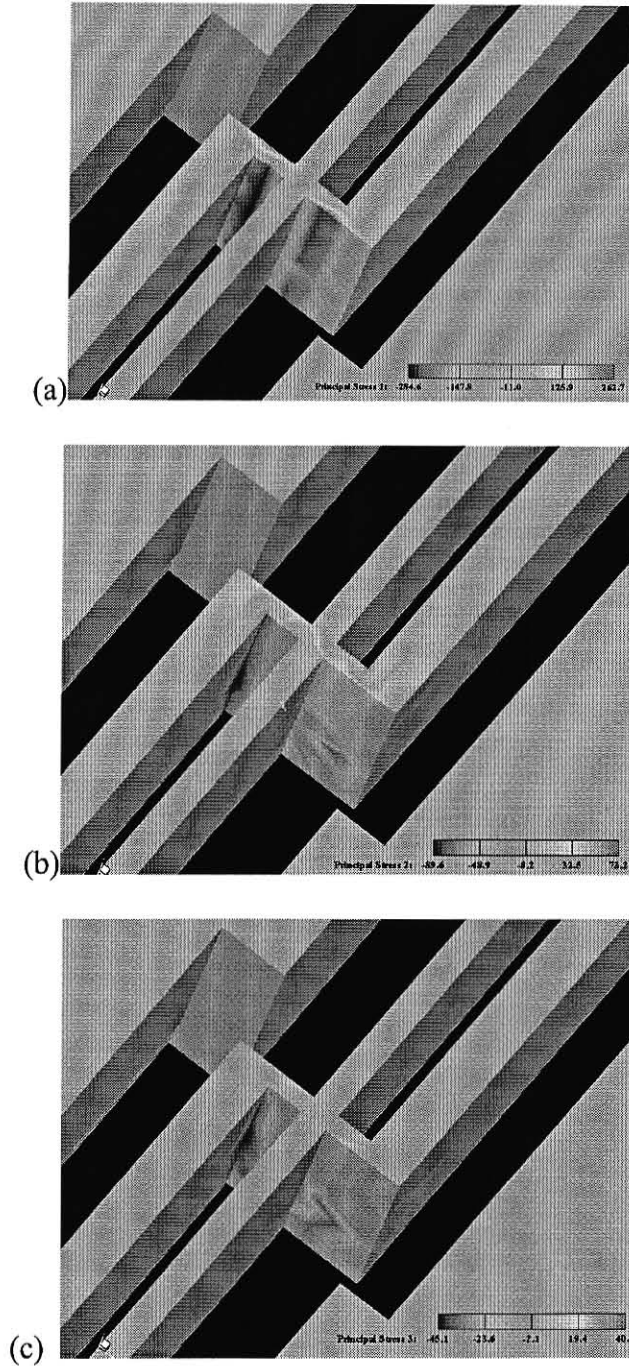


Figure 72. Results for each of the principal stress developed by manipulating movement of the anchors, where (a) $\sigma_1 = 284.60$ MPa, (b) $\sigma_2 = 89.60$ MPa (c) and $\sigma_3 = 89.60$ MPa.

Forcing the anchors to move using a displacement boundary condition was an incorrect method of actuating sensor 3. This modeling technique did not correctly model the generation of stress concentrations developed in the sensor. As a result, the sensor broke at a relatively low level of strain.

To address this problem, ABAQUS, a finite element modeling program was used to model the sensor. Of importance was to correctly model a beam undergoing pure bending with interaction between the beam and sensor correctly defined to examine and avoid stress levels that could lead to failure. Furthermore, the sensor geometry was optimized to produce the capacitance change desired to meet requirements for the telemetry circuitry.

3.2.1.2.2 ABAQUS Finite Element Modeling of Preliminary Sensors

No movement exhibited from sensor 1 and experiencing material failure from the CoventorWare designed sensor 3 set an urgency to correctly model the entire assembly of beam bending, sensor attachment to the beam and movement of the sensor. It was also important to fully understand why the previous sensors had failed. Analysis of the system began by properly constraining the beam to produce a continuous magnitude of strain across its surface while undergoing bending.

A beam was specified by dimensional information and material properties for 316L stainless steel, which are similar rods used for spinal fusion surgery. Two successive steps were used to simulate actuation of the sensor. The first step fixed the location of the beam followed by loading to create bending strain. The initial step

constrained the left end in each axial direction. The second step applied the same boundary conditions; however, a load couple was applied to the right end of the beam. Figure 73 shows the boundary conditions and the load couple applied from the second step of the model. During simulation, the direction of the couple loads was kept normal to the surface of the right end of the beam. The results gave a uniform strain magnitude of $939 \mu\epsilon$ on the surface of the beam, as shown in Figure 73b.

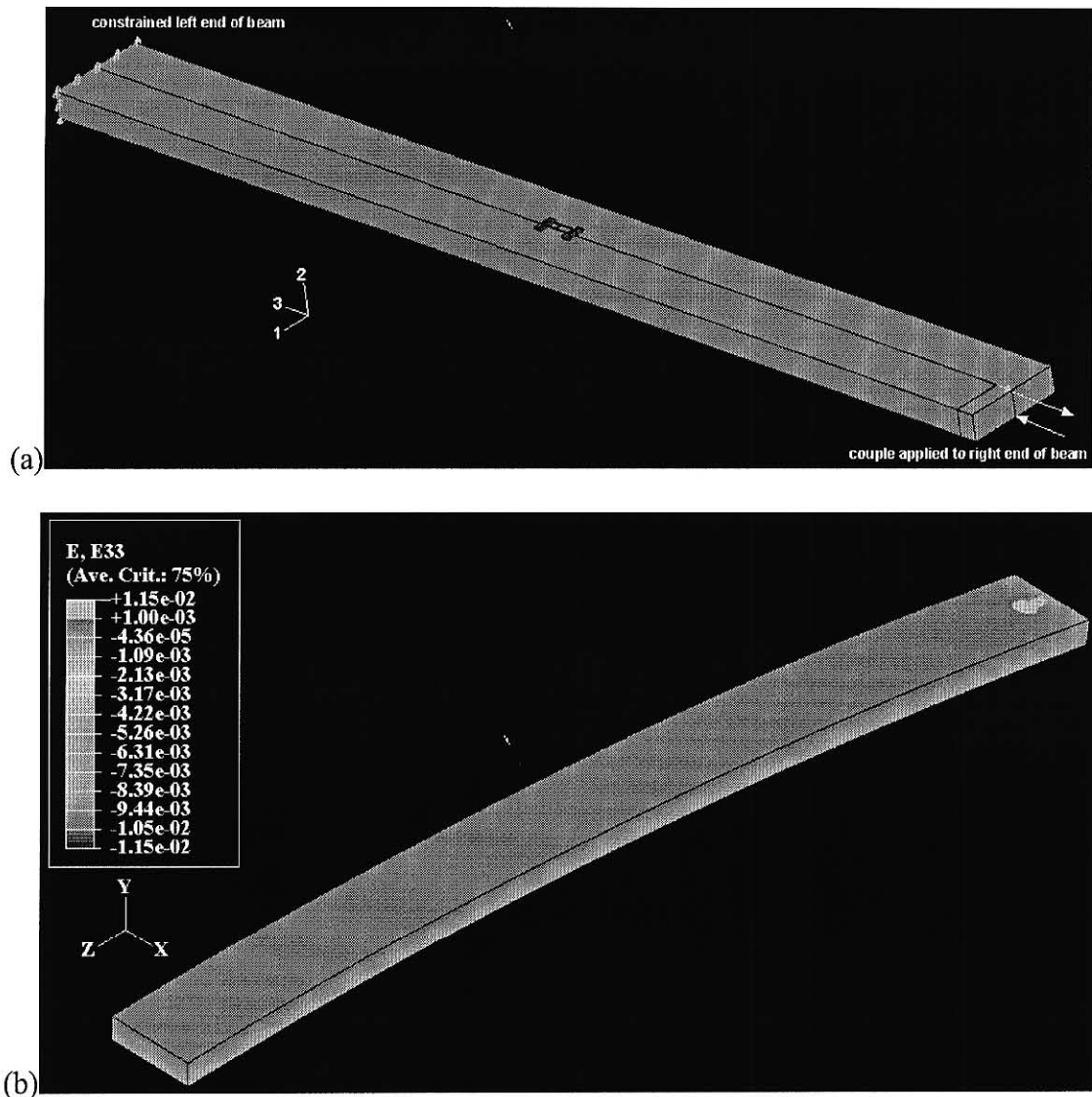


Figure 73. Illustrations of the (a) beam during loading with the left end constrained in all axial directions and a load couple applied to the right end of the beam. (b) The resulting strain profile on the beam.

Sensor 3, from Figure 71, excluding the fingers, was modeled using ABAQUS with the bottom of each anchor fixed to the top surface of the beam using tie constraints. These constraints prevented sliding or moving between the two interfacing surfaces. The beam was deformed and the principal stresses were analyzed to determine if failure would occur. Several different geometries, sensor 4 and 5, were also modeled in an attempt to use a successful two-anchor sensor, as shown in Figure 74. Figure 74a shows a geometric spring replacing the area that failed in the previous fabricated design. However, displacement of sensor 4, 9.82 mm from Figure 74b, was not sufficient to generate the required capacitance change.

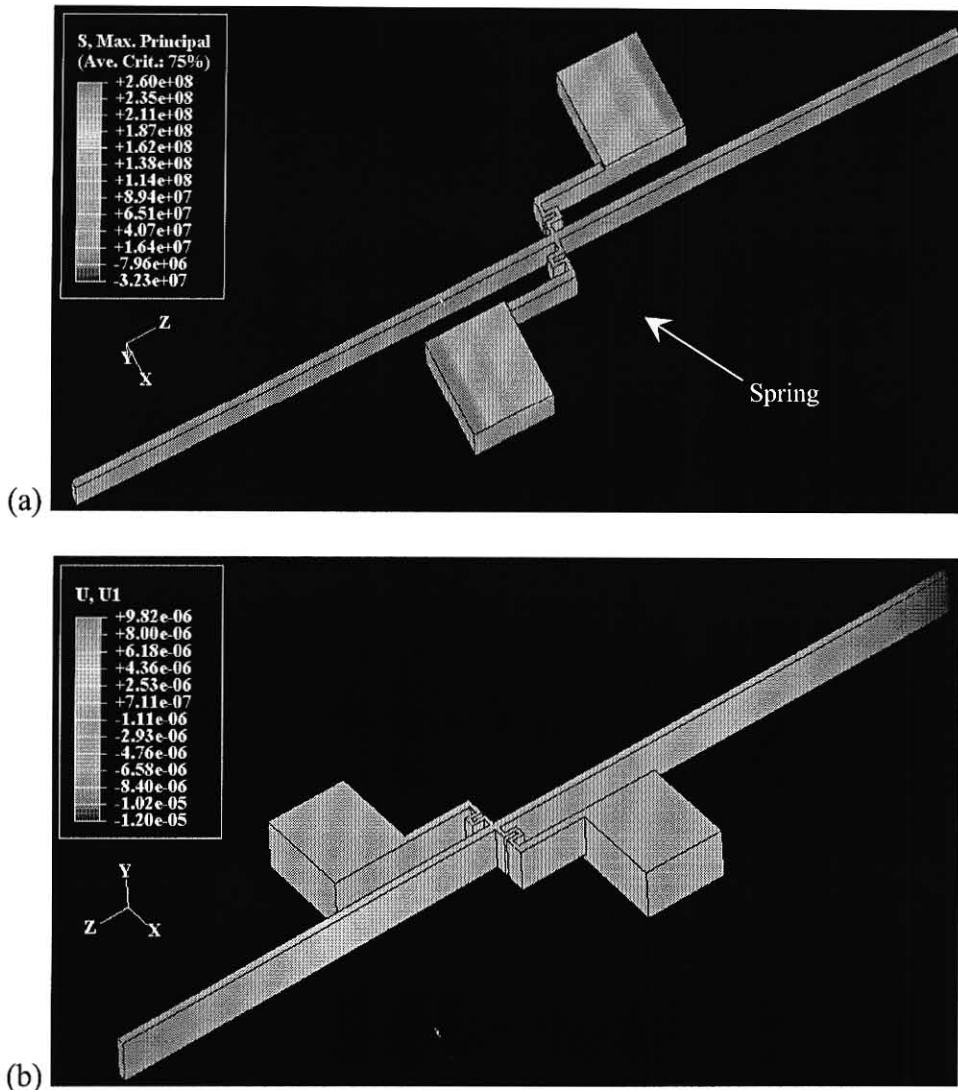


Figure 74. A model developed in ABAQUS using (a) a spring to alleviate stress concentrations with the two anchor system. (b) Displacement of the same model.

A modified version of the offset two-anchor design, sensor 5, was modeled with the anchors in line with each other, as shown in Figure 75. During bending, the anchors move away from each other straightening or increasing the angle between the attached lever arms. The resulting actuation moves the fingers closer to the anchors in the x-axial direction.

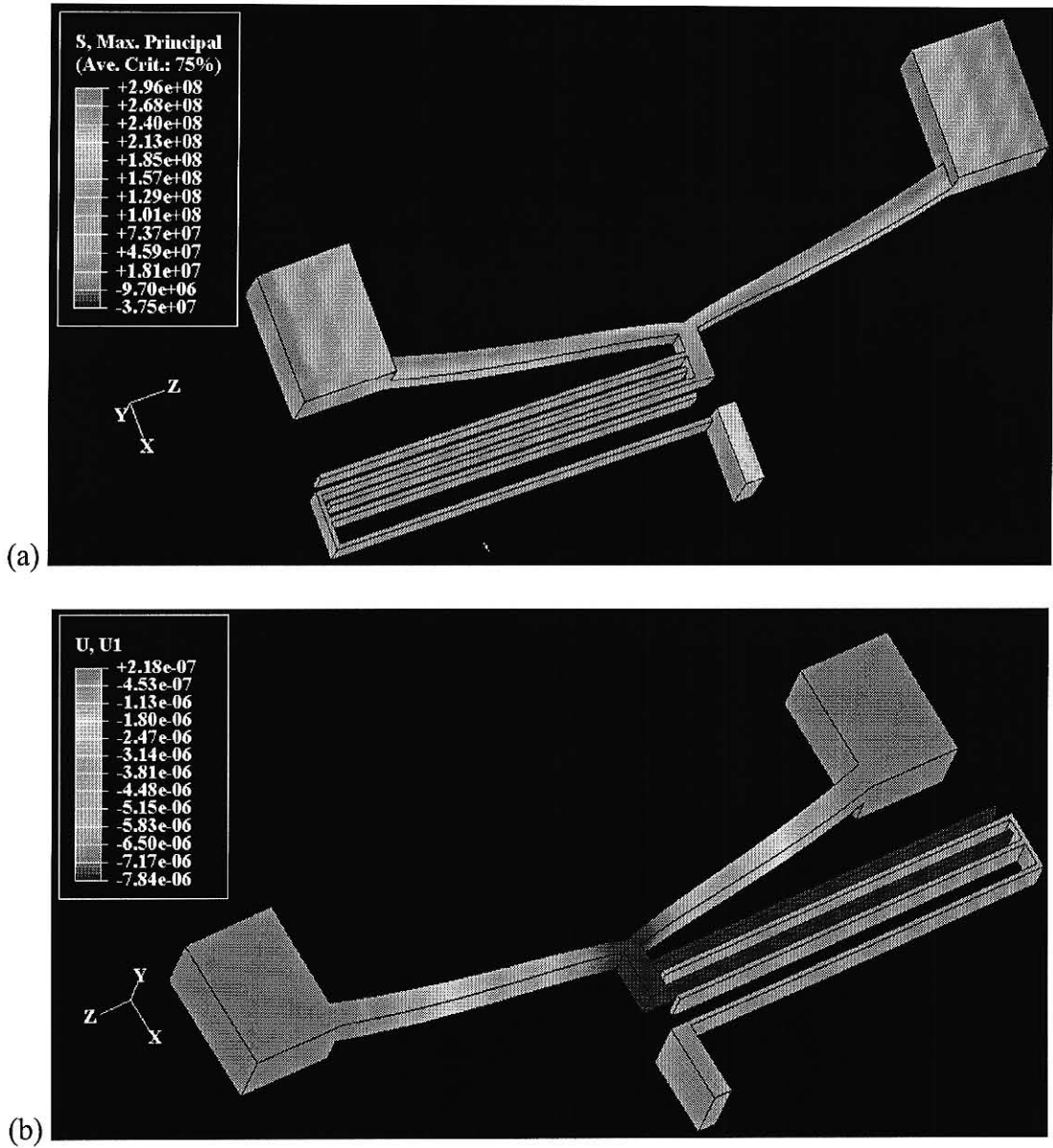


Figure 75. The second model developed in ABAQUS using (a) angled lever with the two anchor system. (b) Displacement of the same model.

3.2.1.3 Fabrication of Preliminary Sensors

Fabrication began by developing photomasks for sensor 1, which was not modeled with CoventorWare or ABAQUS and was based purely upon calculations. The

sensor's photomasks generated from AutoCAD, are shown in Figure 76. This drawing file was converted to DXF format and exported to L-Edit for review. After scrutiny in L-Edit the files were converted to GDS II format for the Laser Pattern Generator, which created two photomasks. Figure 76a was the first photomask generated to process the back side of the silicon wafer, with Figure 76b used for the front side.

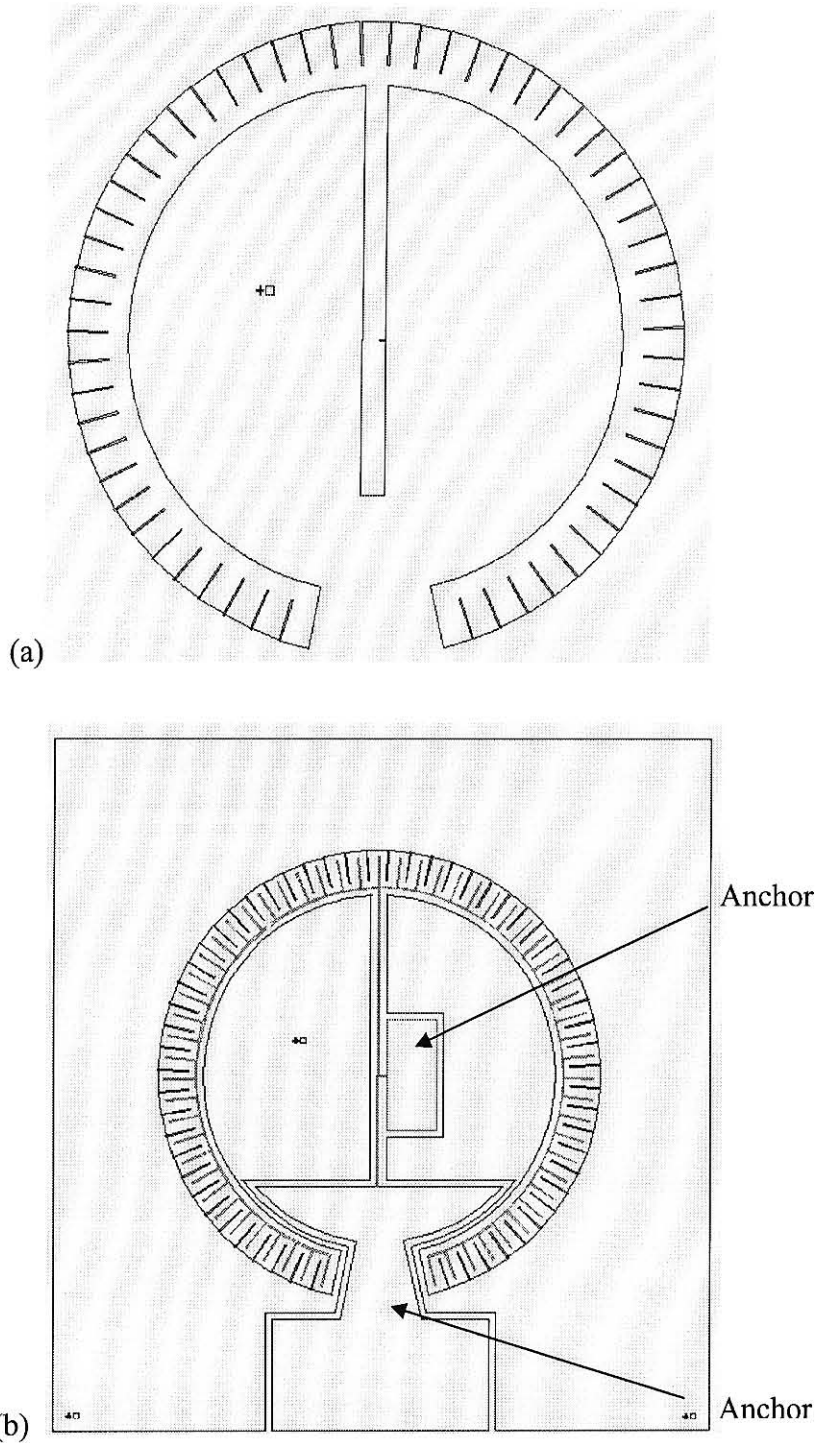


Figure 76. Photomasks created for processing the circular array of interdigitated fingers. (a) The first mask was used to create stationary fingers etched from the bottom side of the wafer. (b) The second mask etched through the remaining wafer to create the final sensor with interdigitated fingers.

Fabrication of sensor 1 began with 2” wafers of <100> orientation with both sides polished and a thickness of 300 μm . Boron doped or p-type wafers were used with a low resistivity of 0.001 – 0.005 $\Omega\cdot\text{cm}$ to replicate a metallic substrate and to avoid sputtering or electroplating a metallic layer. However, this resistivity was still several orders of magnitude higher compared to metallic substance, such as silver (1.6 $\mu\Omega\cdot\text{cm}$) or copper (1.7 $\mu\Omega\cdot\text{cm}$) [81]. Therefore, initial and final capacitance values would vary slightly from the calculated values.

The first processing step began by oxidizing the wafers to provide an adequate mask for etching the bottom of the wafer. Shipley 1813 positive photoresist was then applied to the bottom surface and patterned using the bottom side mask. Buffered Oxide Etch (BOE) was applied to the patterned surface to expose silicon in selected areas as visualized from the bottom side mask. Exposing the silicon allowed the wafer to be bulk etched using potassium hydroxide (KOH) to a depth of 50 μm . The remaining oxide layer was removed from both sides using BOE and the anchors were anodically bonded to 300 μm thick 7740 borosilicate glass. The glass was applied to act as an intermediate substrate between the sensor and the beam. With processing completed on the back of the sensor the second mask was used to pattern the outline of the sensor’s interdigitated fingers on the front with OCG-thick negative resist. This resist was selected to withstand the harsh etching process of Deep Reactive Ion Etching (DRIE) and was removed afterwards using Nano-Strip. The DRIE process etched through the remaining silicon as patterned from the front side mask and completed the sensor in its final form. Figure 77

shows sensor 1 along with a detail photo of the interdigitated fingers and the DRIE sidewall.

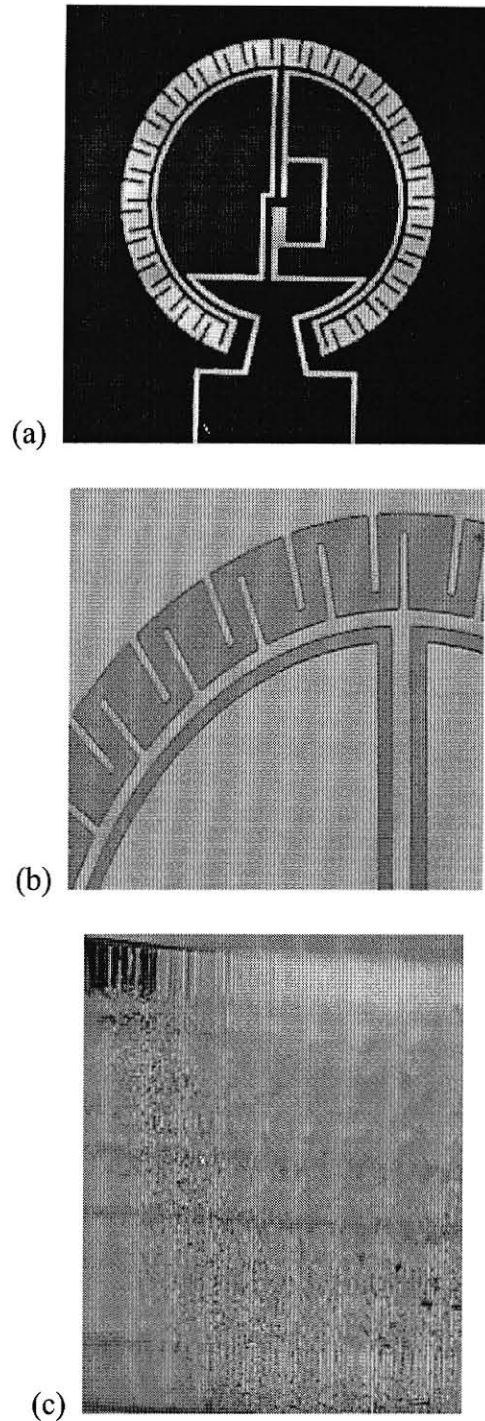


Figure 77. The fabricated sensor from (a) an overall picture and (b) a detail photo of the interdigitated fingers (c) An illustration of the side of a finger demonstrating the etch profile from the DRIE process.

Sensor 1 was attached to a flat beam and lead wires were connected to a CV analyzer meter to gather capacitance and conductance data. The sensor was placed on a cantilever beam and underwent three-point bending to actuate the sensor.

Sensor 3 was fabricated using information from the CoventorWare model and similar fabrication techniques. After application of sensor 3 to the flat beam, the central lever arm was manually probed to ensure the fingers were free from debris and could move freely. The beam was placed in three-point bending to actuate the sensor. Sensor 3 and an illustration of silicon debris remaining between the fingers after the DRIE process are shown in Figure 78.

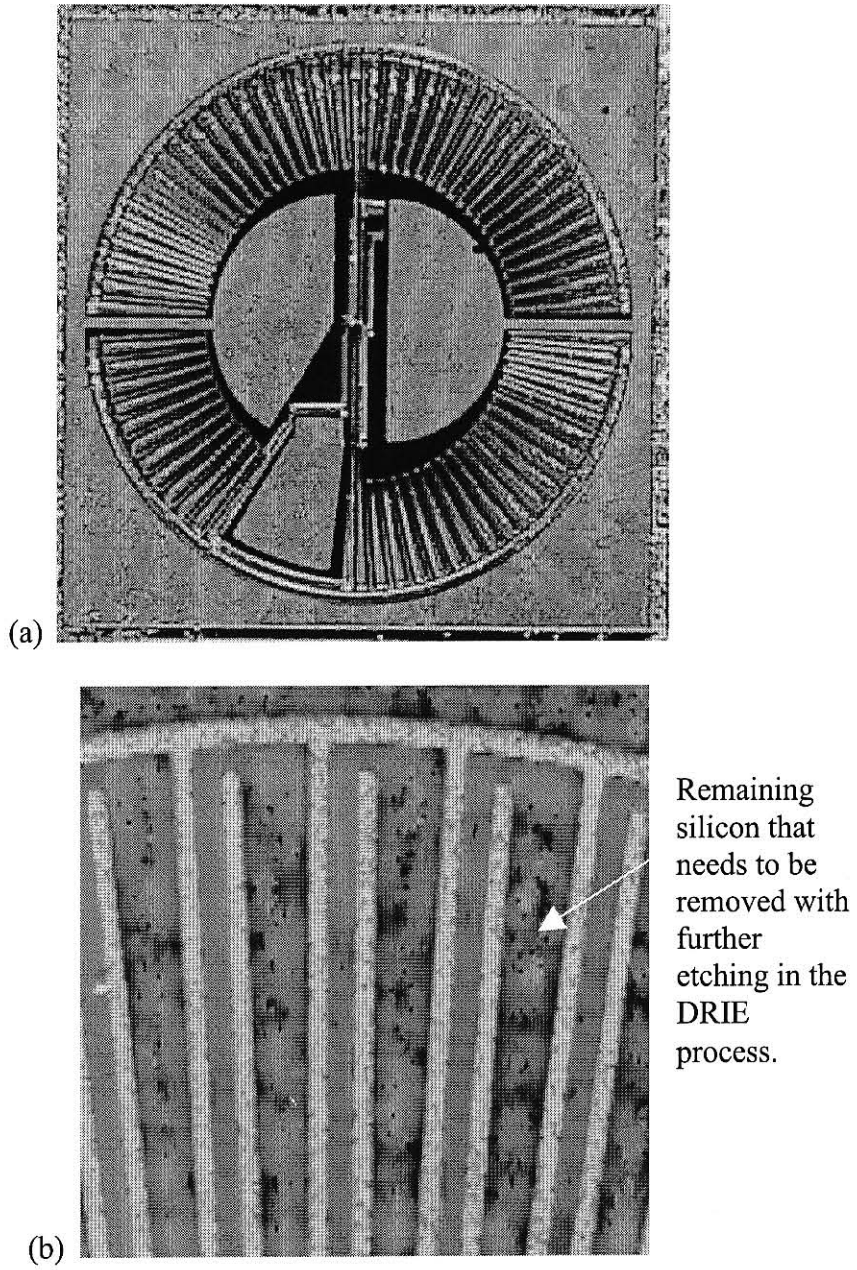


Figure 78. An illustration of (a) the fabricated sensor with a (c) detailed view of the interdigitated fingers.

3.2.2 Preliminary Sensor Results

Sensor 1 had 58 pairs of fingers, 300 μm long and 250 μm tall. Initial spacing between the fingers before actuation was 25 μm and 75 μm on either side of the moving fingers. The initial calculated capacitance before actuation was 0.81 pF. After actuation, the spacing between the fingers reduced 20 μm on one side and increased the same on the other side. This gave a capacitance of 3.21 pF with a 2.40 pF differential.

Sensor 1 was attached to a beam and placed in a cantilever beam fixture where a load was applied to the end of the beam to induce three-point bending. Lead wires from the sensor were connected to a CV analyzer to measure capacitance and conductance. High levels of conductance were used to signal when the fingers were touching during bending, however, no changes in capacitance or conductance were recorded. Additionally, sensor 1 was visually inspected and no movement of the fingers attached to the central lever arm was observed.

CoventorWare modeling results of sensor 3 calculated the initial capacitance to be 5.04 pF. After bending was induced, the model predicted a capacitance increase to 9.04 pF. Sensor 3 was placed on the cantilever beam, where a load was applied to the end to induce bending. Initially, the fingers began to move as strain was increased. At approximately 250 μe the arm extending to the upper anchor experienced material failure and the sensor broke. Figure 79 is an illustration of two examples of sensor 3 experiencing failure in the same location. The lever arm failure caused the interdigitated fingers to spring back to their original unstrained position.

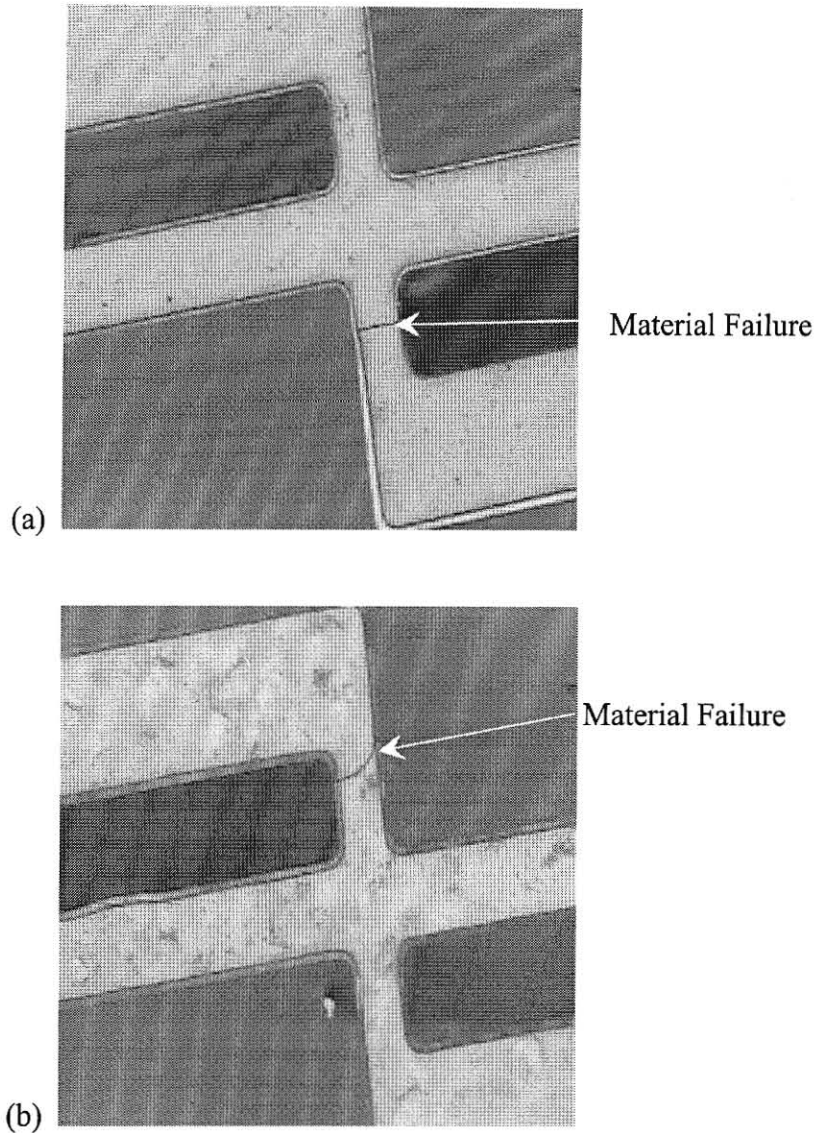


Figure 79. Illustrations of material failure occurring in sensor 3.

To understand the failure of sensor 3, it was modeled using ABAQUS with the bottom of each anchor fixed to the top surface of the beam using tie constraints. These constraints prevented sliding or moving of the two interfacing surfaces. The results revealed that stress concentrations developed in the same location where failure occurred during testing of the sensors. The level of strain exceeded the fracture strength of silicon.

3.2.3 Discussion of Preliminary Sensors

No movement of the fingers for sensor 1 may have been caused by inadequate spacing between the anchors and insufficient lever arm length. A comprehensive study and finite element analysis would need to be performed to fully determine the lack of actuation for sensor 1.

Sensor 3 was modeled using CoventorWare, where computations predicted a change of 4 pF at 1000 $\mu\epsilon$. The change in capacitance was lower than the constraint established for the telemetry system, but was deemed acceptable. The CoventorWare model identified the location where principal stresses would develop, but stress values did not exceed the fracture strength of silicon. The model error was attributed to lack of interaction between the anchors and the flat beam. The model underestimated the stress developed in the sensor during strain from the rod to the sensor.

After each of the previous design failures, several different geometries of the two-anchor system, sensors 4 and 5, were modeled using ABAQUS. Initial capacitance of each of the devices was adequate and the principal stress values for each model were well below the fracture strength of silicon. However, displacement of the models was insufficient to generate the change in capacitance needed for the telemetry system.

3.2.4 Conclusions for Preliminary Sensors

The sensor was designed to meet constraints for the telemetry housing to initially generate 5 pF of capacitance and exhibit a change of 5 pF at 1000 $\mu\epsilon$. Finite element

modeling using CoventorWare and ABAQUS, fabrication and testing of the various initial designs developed the following conclusions.

1. Sensor 1 experienced lack of movement due to insufficient geometry design of the sensor.
2. Sensor 3 experienced material failure. The location of maximum principal stress was identified by the CoventorWare model.
3. The modeling error generated stress results that were below the fracture strength of silicon and did not predict material failure.
4. Modeling the two anchor system applied to a beam did not generate a change in capacitance sufficient to meet the constraints of the telemetry system.

As a result of the experienced material failure, lack of actuation and minimal capacitance change the two anchor sensor design was abandoned.

3.3 Final Sensor Approach

Design progression of the sensor necessitated a new design that minimized stress generation regardless of the actuation of the sensor. The new sensor would still implement interdigitated fingers; however, it was paramount to untie each group of opposing fingers so that they move independently to avoid stress generation.

Finite element modeling techniques were used during development. The sensor was applied to a beam using tie constraints and would undergo four-point bending. An assortment of anchor designs were considered to allow independent movement of the interdigitated fingers. Sensor displacement and generated stress were scrutinized to decide upon the geometry of the anchor's footprint. Ideal conditions would offer maximum displacement to create a maximum change in capacitance with minimal stress.

Previous fabrication techniques were used and the sensor attached to a beam while undergoing four-point bending. Testing protocol used for the housing was applied to the sensor to gather behavioral characteristics. Response of the sensor was measured to make sure it met constraints of the telemetry system and to determine sensitivity.

3.3.1 Materials & Methods

Comb drives or systems using interdigitated fingers for variable capacitors, electrostatic actuation and frequency tuning have become integral parts of microelectromechanical system (MEMS) devices in an emerging technology for RF and wireless communications. From these sources, an initial design without dimensional data was conceived, as shown in Figure 80.

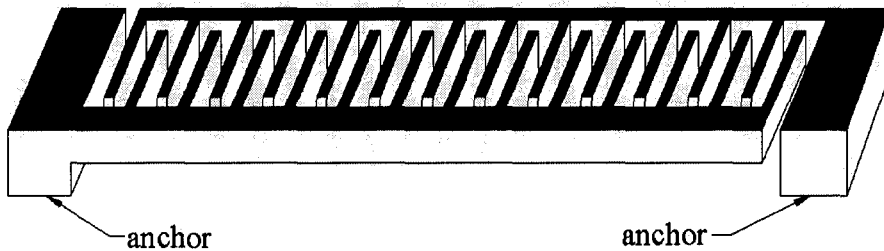


Figure 80. An illustration of the comb drive or interdigitated finger design with two independent anchors.

Amplification of the sensor's actuation was important. This was achieved by increasing the height of the anchors, which increased the distance from the neutral axis of the rod to the fingers.

The telemetry system required an initial sensor capacitance of 5 pF due to parasitic capacitance. Based upon the calculated 10 μm change in the sensor's length, the initial gap, finger sidewall height, length and the number of fingers were determined. Anchor height was changed by adding a glass pad to achieve larger actuation, higher sensitivity and to provide a large surface area to attach the sensor to the rod. The final design included an array of 98 interdigitated fingers that were 25 μm wide, 150 μm tall and 1950 μm long, with a spacing of 25 μm to the adjacent finger. The large gap

between the fingers was required to maintain a 10:1 aspect ratio needed for the DRIE process to create the interdigitated array. Due to vibration and impact loads from the human body during walking and daily activities the finger width was intentionally wide to add robustness. Based upon dimensional information, the initial capacitance was calculated to be 10.15 pF, which was acceptable for the telemetry system.

While undergoing bending, the sensor exhibited a parabolic increase in capacitance due to its transverse actuation. The narrow gap developed on one side of the interdigitated fingers dominated the sensor's net capacitance. However, the sensor also exhibited a vertical actuation resulting in a reduction of the overlapping surface area. The model was examined in the transverse and vertical directions using an applied strain of $1000 \mu\epsilon$. Transverse travel or reduction of the finger spacing was $12.60 \mu\text{m}$ with a vertical actuation of $1.16 \mu\text{m}$ to give a final calculated capacitance of 13.35 pF at $1000 \mu\epsilon$. Figure 81 shows a front view of how the sensor attaches to the beam and the vertical actuation. Transverse actuation is not seen in this view.

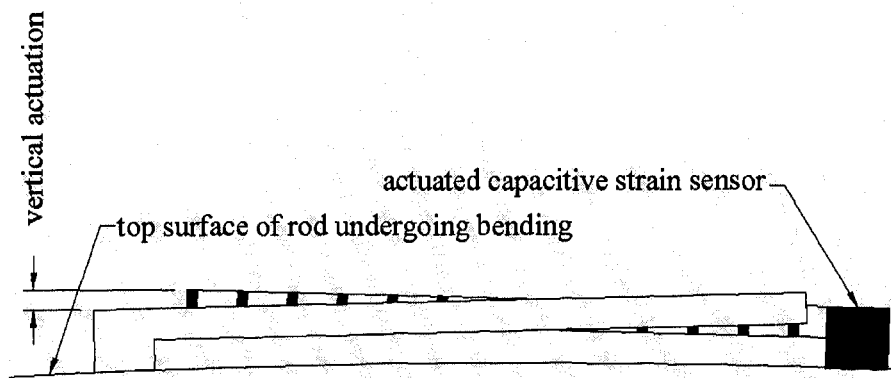


Figure 81. Front view of the capacitive strain sensor actuated from the rod undergoing bending.

A model was generated using ABAQUS finite element modeling software. A large number of anchor configurations were analyzed to evaluate stress concentration.

The beam was placed in bending to actuate the sensor and tie constraints kept the sensor affixed to the beam. The anchor configuration which developed the largest displacement, yet, the lowest principal stress was selected for fabrication.

Fabrication techniques used for the new design were replicated from sensor 1 and 3. The sensor was affixed to a beam and placed in four-point bending in the MTS where cycle, static and maximum load testing occurred. Capacitance, conductance, MTS load and displacement data were recorded using customized LabView virtual instruments. Conductance was recorded to verify when the fingers had reached their maximum displacement, so that further loads were not placed on the sensor to cause failure.

3.3.1.1 ABAQUS Finite Element Modeling of the Final Sensor

The sensor was modeled by affixing Borosilicate (7740) glass to the bottom of the anchors and attaching the assembly to a beam using tie constraints. This was performed to reduce stress concentrations and to provide ample area to apply adhesive. To reduce computational time, the model was simplified to include fingers only in the middle and end sections, as seen in Figure 82.

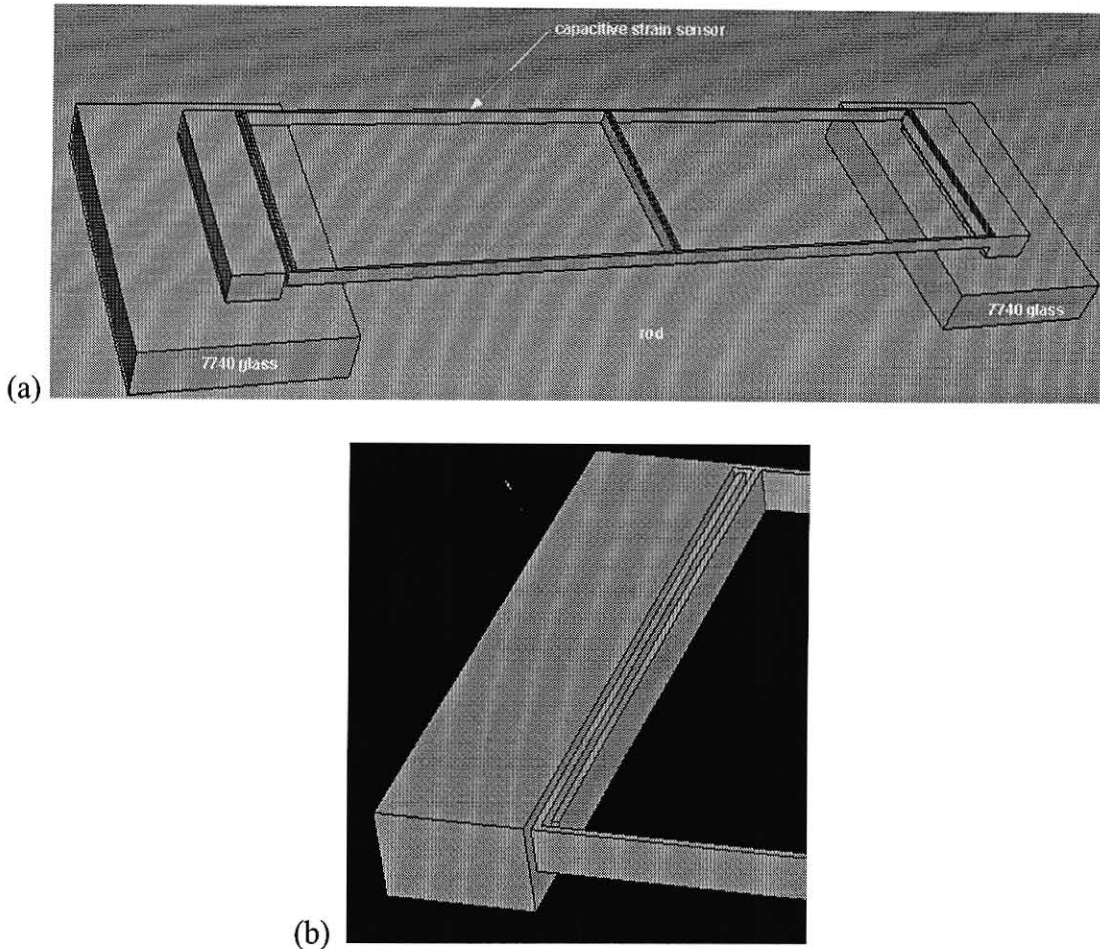


Figure 82. FEA model illustrations from the ABAQUS FEA model before bending (a) Overall view of the sensor model attached to the rod. (b) Close up view of the end of the sensor demonstrating the fingers and anchor.

The beam was modeled with 316L stainless steel properties. The glass was represented as an isotropic material with a Young's modulus of 63 GPa, tensile strength of 6.8 MPa and a Poisson's ratio of 0.2. Silicon was represented as an isotropic material with a Young's modulus of 150 GPa and a Poisson's ratio of 0.17. The beam was meshed with 750 μm , 20 node quadratic node bricks with reduced integration or C3D20R elements. The glass pads were meshed with similar elements as the beam, but were 150 μm in size. The sensor was modeled as 100 μm , 10 node modified quadratic tetrahedrons or C3D10M elements. Brick elements were considered for the sensor geometry, but

exceptionally long finger lengths as compared to the finger width would have created an unreasonably number of small elements and extended computational time. Figure 83 shows the meshed model of the sensor and beam.

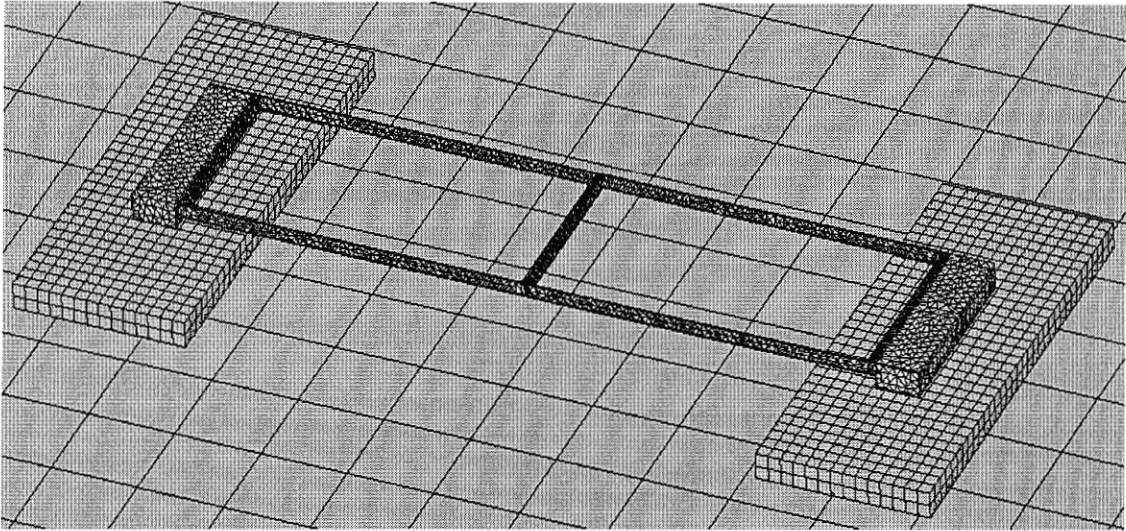
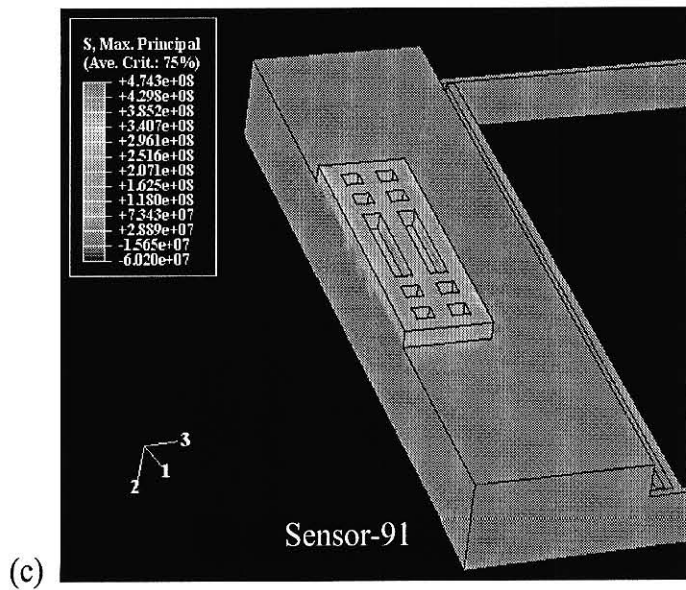
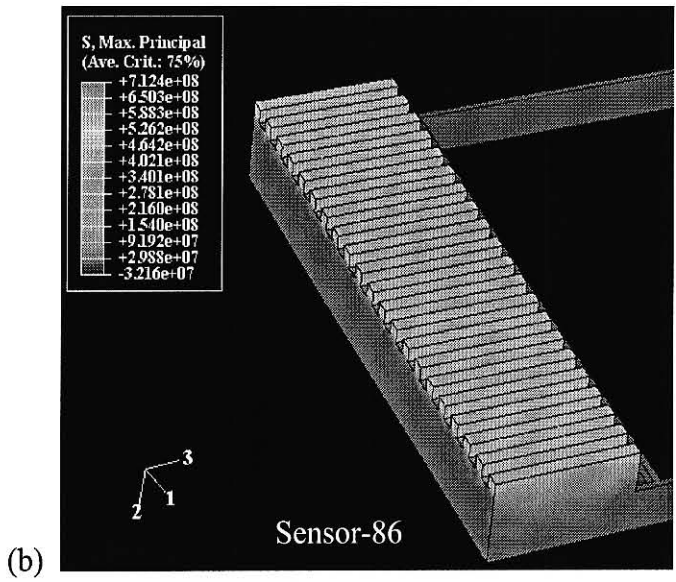
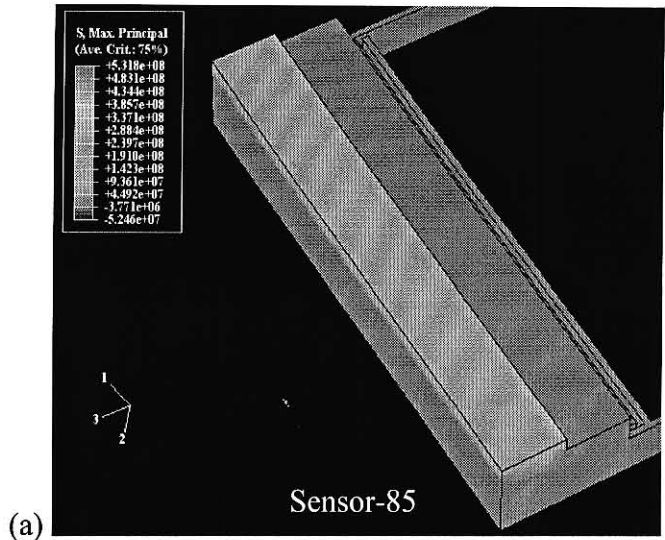
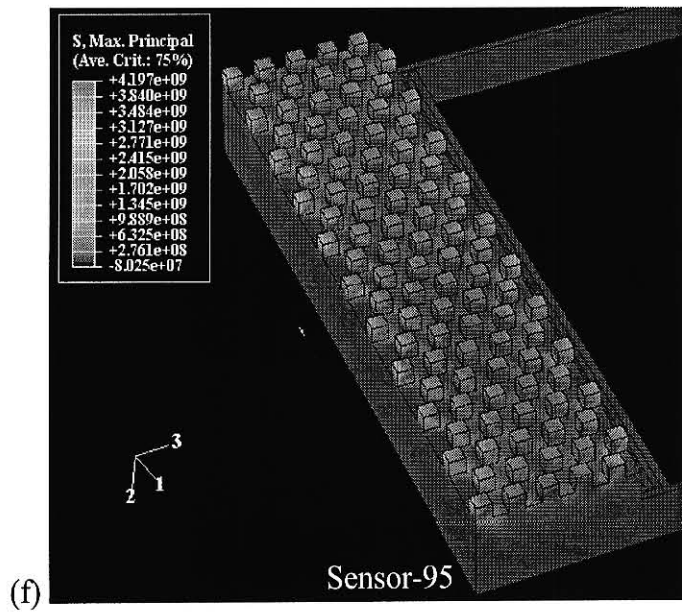
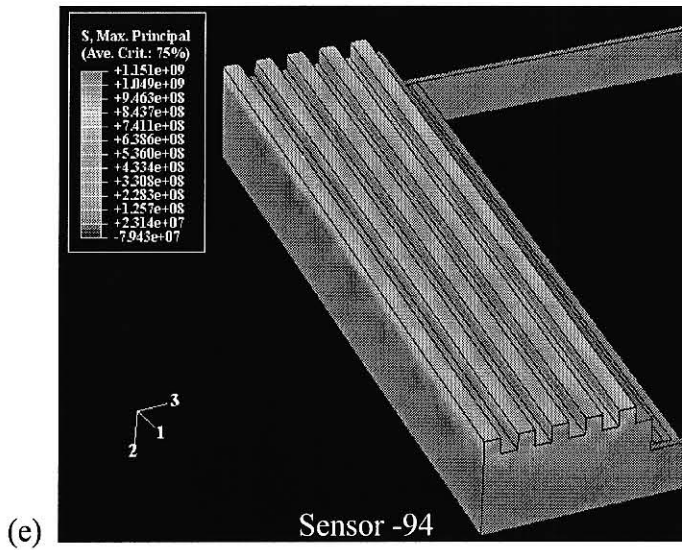
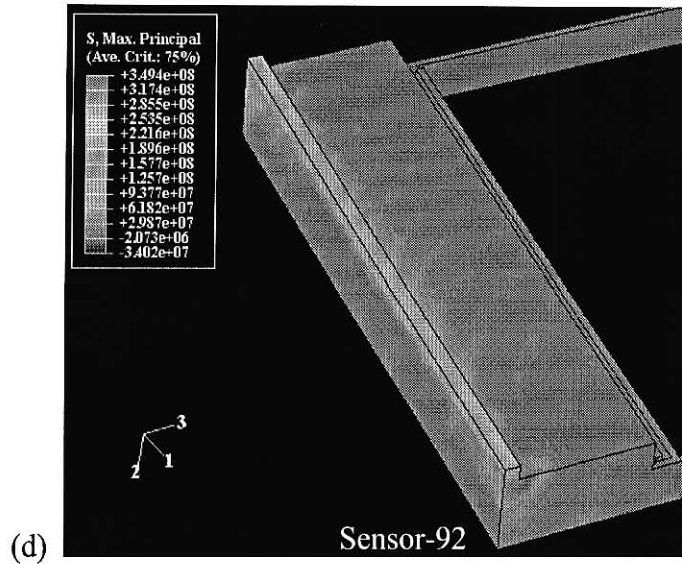
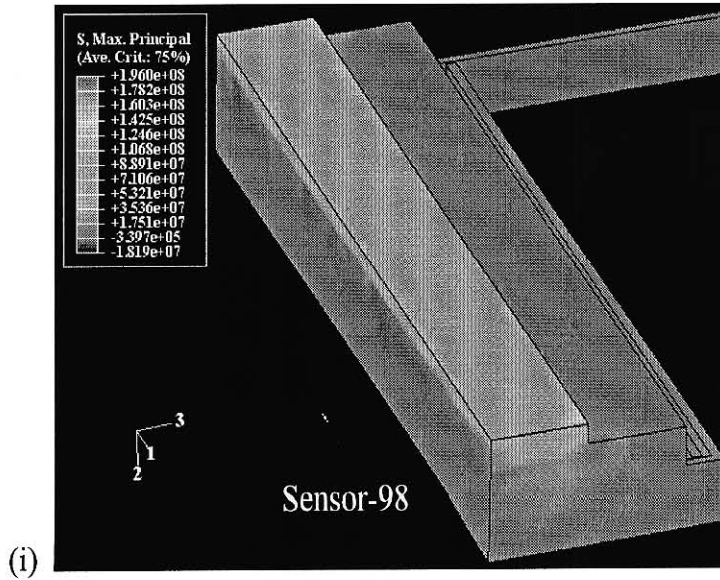
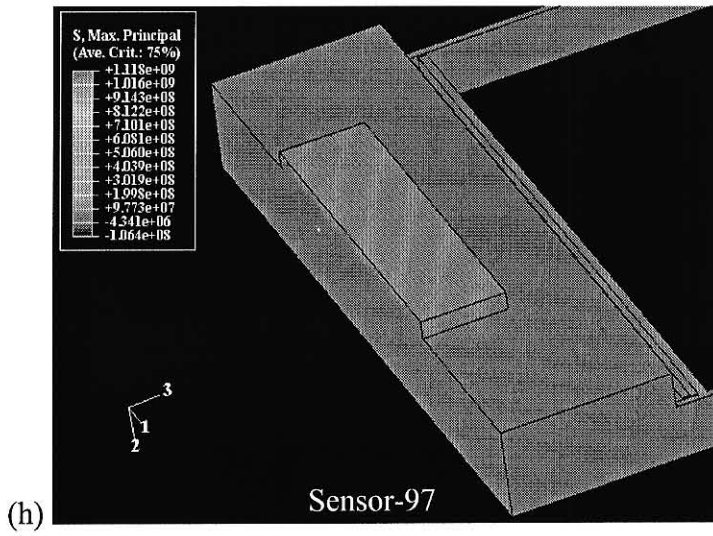
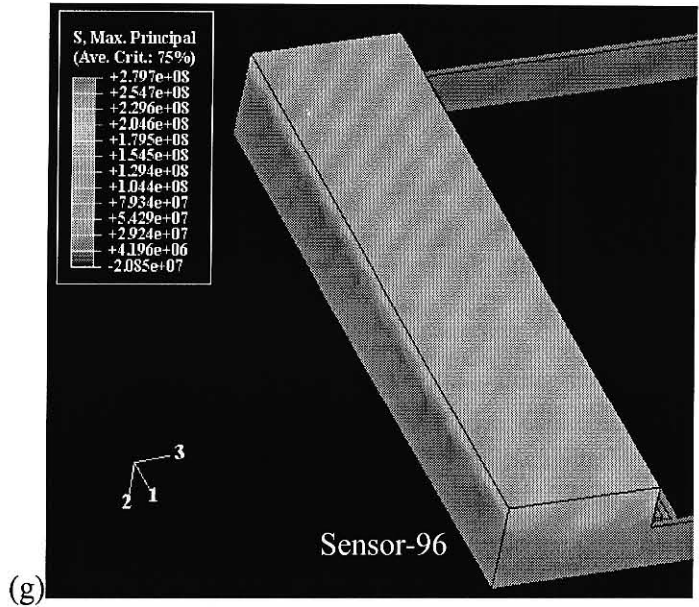


Figure 83. Illustration of the meshed assembly from ABAQUS.

Different anchor configurations were modeled to determine which would develop the largest amount of finger displacement with the least amount of maximum principal stress. A variety of designs were considered that attached the sensor to a glass pad or directly to the beam. The height of the glass pad was also increased from 300 μm to 500 μm , in model Sensor-99, to confirm whether the sensor would actuate further. Figure 84 (a-k) shows the bottom of each anchor considered.







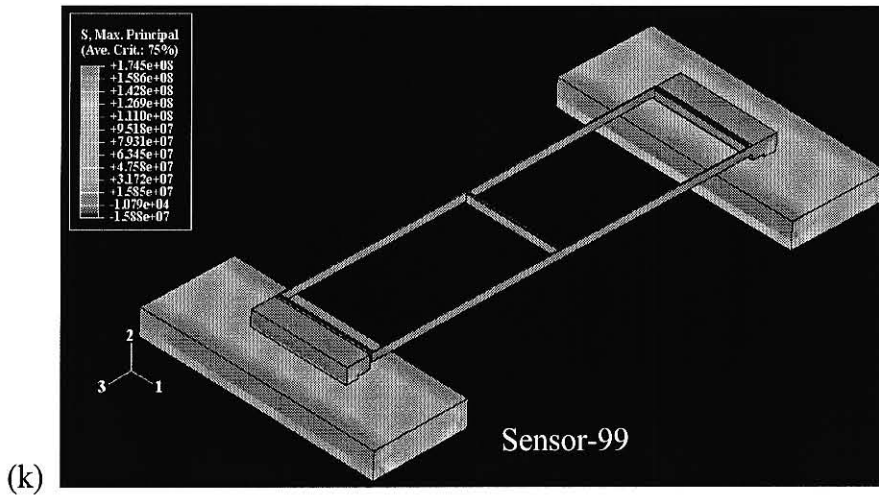
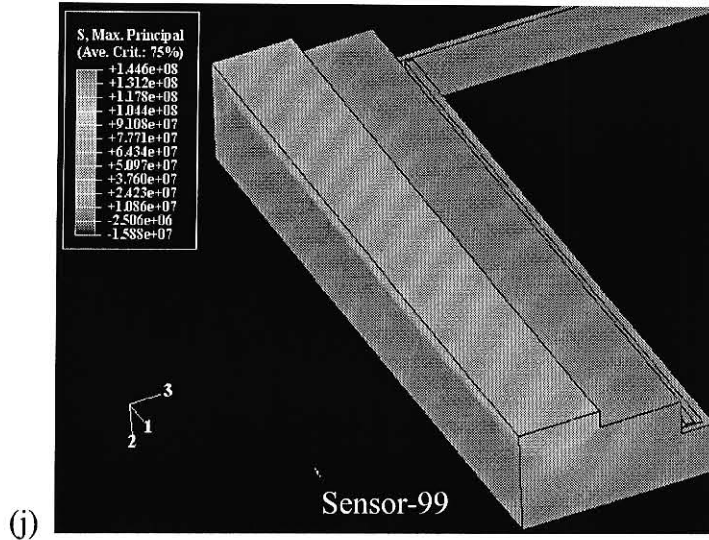


Figure 84. Modeling results from ABAQUS (a - k) showing the maximum principal stress developed in each anchor design. Illustration (j) shows results from using a pad that was 500 μm tall rather than 300 μm considered for all other modeling results.

3.3.1.2 Fabrication of the Final Sensor

The fabrication process used 2" wafers with $\langle 100 \rangle$ orientation with both sides polished and a thickness of 300 μm . Boron doped or p-type wafers were used with a low

resistivity of 0.001 – 0.005 $\Omega\cdot\text{cm}$ to replicate a metallic substrate and to avoid sputtering or electroplating a metallic layer. Processing began with a base cleaning process to remove organic materials and wet oxidation to develop an oxide thickness layer approximately 1 μm thick. One side of the wafer patterned the oxide using a buffered oxide etching (BOE) solution to create the sensor's anchors. The oxide was removed on the other side of the wafer and wet etched using Potassium Hydroxide (KOH) until the overall thickness of the wafer was 150 μm .

The wafer was wet oxidized again to an oxide thickness of 1 μm , which would serve as a mask for the deep reactive ion etching (DRIE) process on the front of the wafer. The front of the oxide layer was patterned and the wafer was cleaved into four sections. Cleaving of the wafer was necessary to avoid excessive heat generation in the wafer, which would carbonize the masking photoresist during the DRIE process. Glass pads were anodically bonded to the anchors and the top of the wafer was patterned using front to back alignment.

The assembly was etched in a Surface Technology System's Multiplex Advanced Silicon Etcher DRIE (Imperial Park, Newport, UK) system until the elevated interdigitated fingers were free. This particular etching process used radio frequency inductively coupled plasma operating at 13.56 MHz with an electron density that exceeded 10^{12} electrons per cm^3 . Using fluorine gases, sulphurhexafluoride (SF_6) and carbontetrafluoride (CF_4), the selectivity of etching silicon to silicon-oxide was better than 150:1 [82]. However, photoresist materials were also used to provide an additional masking barrier. Once inside the ICP chamber, the wafer was placed on a liquid nitrogen cooled chuck and helium was used to provide direct heat transfer from the wafer.

Sulphurhexafluoride was introduced and etched the desired areas followed with a polymerization process from the carbontetrafluoride. As a result of the cryogenic cooling, condensation developed from the reactant gases and protected the sidewalls from etching, which helped the anisotropic etching process. This process was repeated until the desired depth was obtained.

However, limitations occur with this process, particularly when characteristics from the photolithography masks that require etching aspect ratios that exceed 10:1. Vertical sidewalls are normally desired from this process and were used for sensor fabrication; however, the etching process can be modified to deliver sidewalls of varying angles. These angles can be characterized by gas flow rates, duration of etch and passivation cycles, and wattage of the platen. Figure 85 demonstrates the fabrication process with an illustration of the sensor after fabrication.

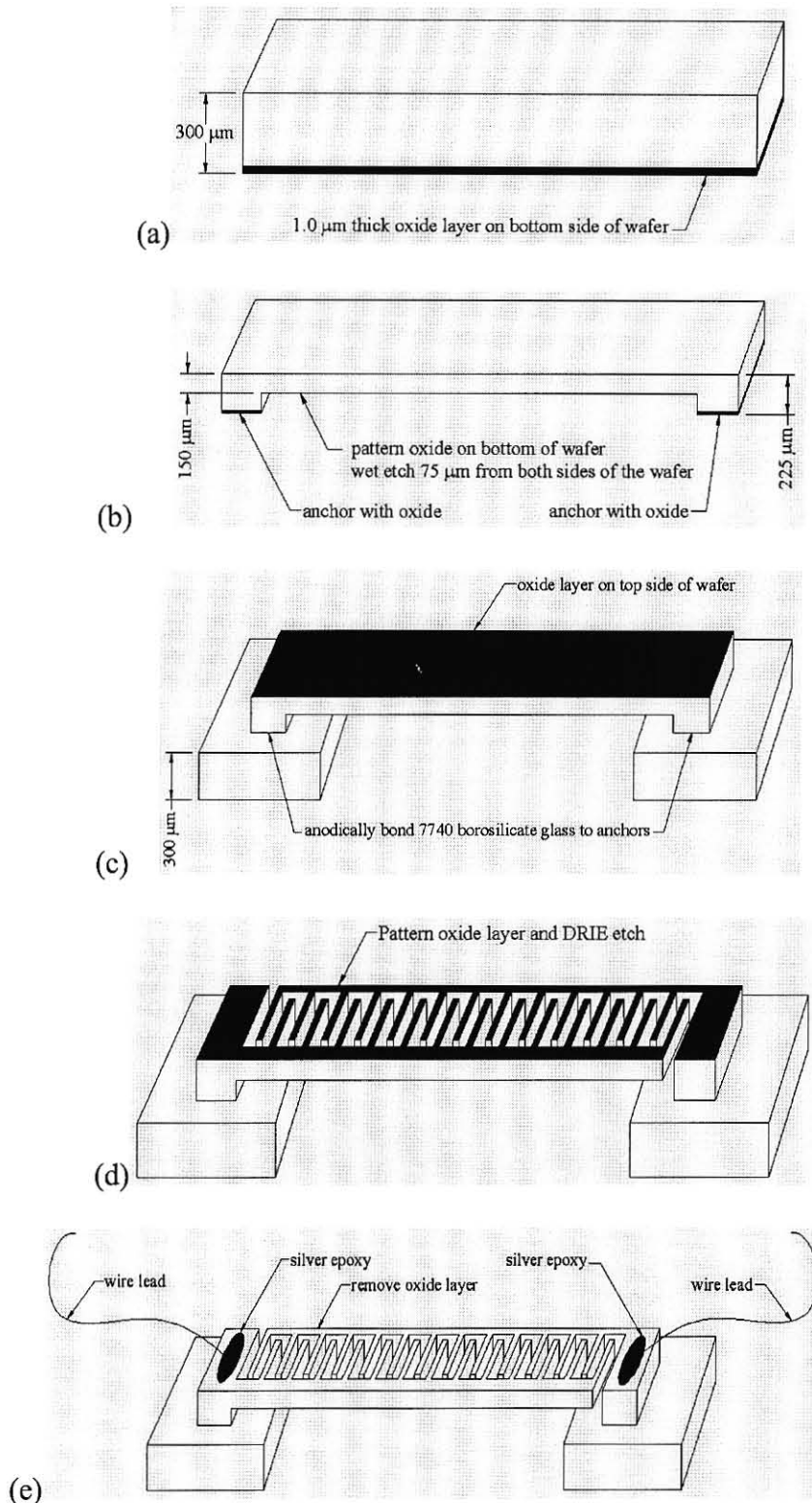


Figure 85. Fabrication process of the capacitive bending strain sensor. (a) Oxidation (b) Wet etching the bottom of the wafer to form anchors (c) Anodic bonding glass pads to the anchors (d) Deep reactive ion etching the interdigitated fingers. (e) Application of the wire leads.

Figure 86 shows the two photomasks used to fabricate the devices. The first mask was used to pattern the oxide layer on the bottom of the wafer and to expose silicon that would be etched to form the anchors. The second mask was used to pattern oxide on the top of the wafer that exposed silicon for the DRIE process to develop the interdigitated fingers. Figure 86c illustrates the completed sensor after fabrication.

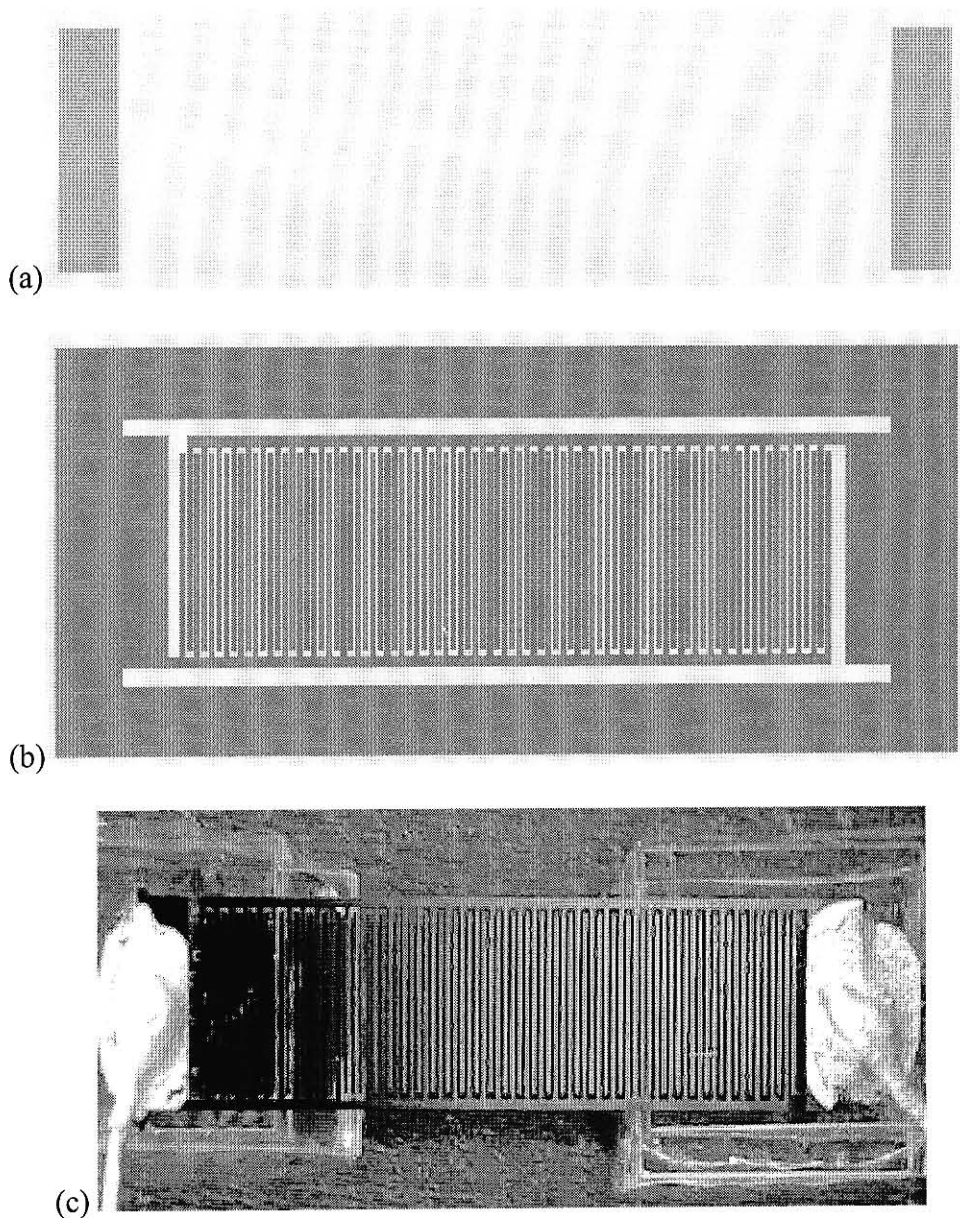


Figure 86. Illustrations of the photomasks and the completed sensor (a) The first photomask was used to develop the anchors. (b) The second photomask formed the interdigitated fingers. (c) The completed sensor after fabrication.

3.3.1.3 MTS Testing of the Final Sensor

The sensors were attached to a steel beam using a cyanoacrylate adhesive and tested for a capacitance change in four-point bending. Conductance and capacitance of the sensor was measured using a Keithley 590 CV Analyzer. If conductance was less than $2 \mu\text{S}$ then all silicon material was clear between the fingers and a change in capacitance could be measured. Figure 87 shows the MTS applying bending strain and a sketch of the load diagram. The sensor was placed between the loading points of the MTS fixture, where bending strain was constant.

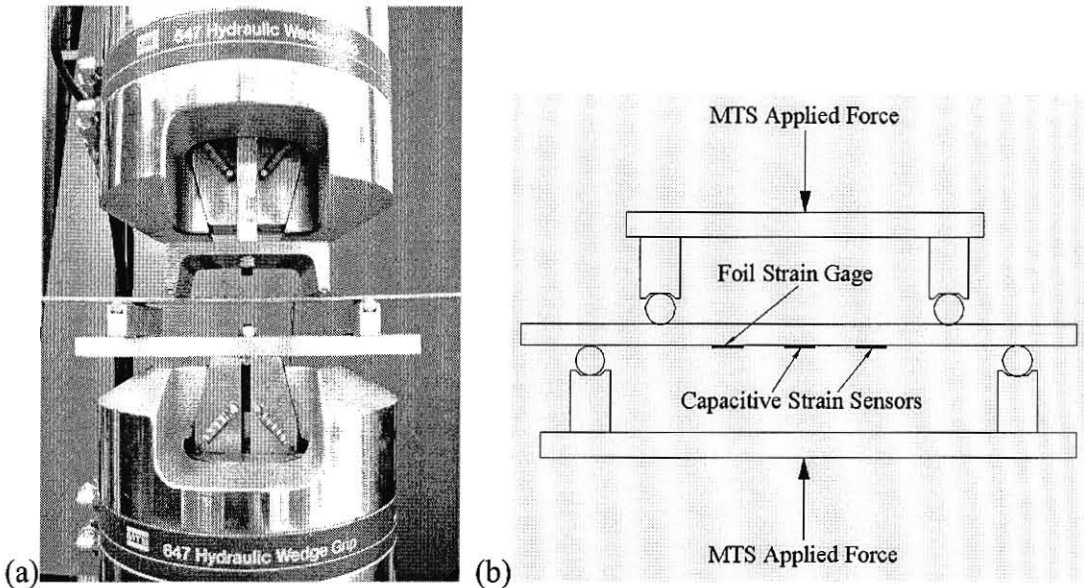


Figure 87. Four point bending in the (a) MTS fixture applying an equal strain magnitude across the surface of the beam. (b) Illustration of the loads applied by the MTS and placement of the sensors and strain gage on the bar.

Strain gages were mounted on the beam and configured in a one-half Wheatstone bridge for temperature compensation. The gages were connected to a 2120A Measurements Groups strain gage conditioning unit. Following shunt calibration, the strain analog signal and load cell output from the MTS were recorded using a custom

virtual instrument developed using LabView version 6.1 and a National Instruments 6024 data acquisition card with a sampling rate of 6.3 samples per second. The capacitance sensor was connected to the Keithley CV Analyzer where the GPIB output was recorded with the same virtual instrument and collection rate.

A series of tests were developed to characterize the behavioral response of the sensor. The first test applied a cyclical load to generate 200 to 1010 $\mu\epsilon$ at a frequency of 0.0083 Hz for five hours to determine if hysteresis was present. Application of a zero load was not selected due to a possibility of the beam slipping in the MTS fixture.

The second test statically loaded the sensor for an extended period of time to see if capacitive output of the sensor would drift over time. The final test recorded the initial capacitance of the sensor with no load on the beam. Gradually, the beam was loaded until the sensor achieved its maximum capacitance and could not actuate further without risking failure. The sensor was unloaded in the same manner to determine if the response was reliable. Figures 88-92 show the virtual instruments developed in LabView to capture strain, load cell and capacitance data from each test.

Strain Monitoring System for MTS Four Point Bending

by: Julia Aebersold

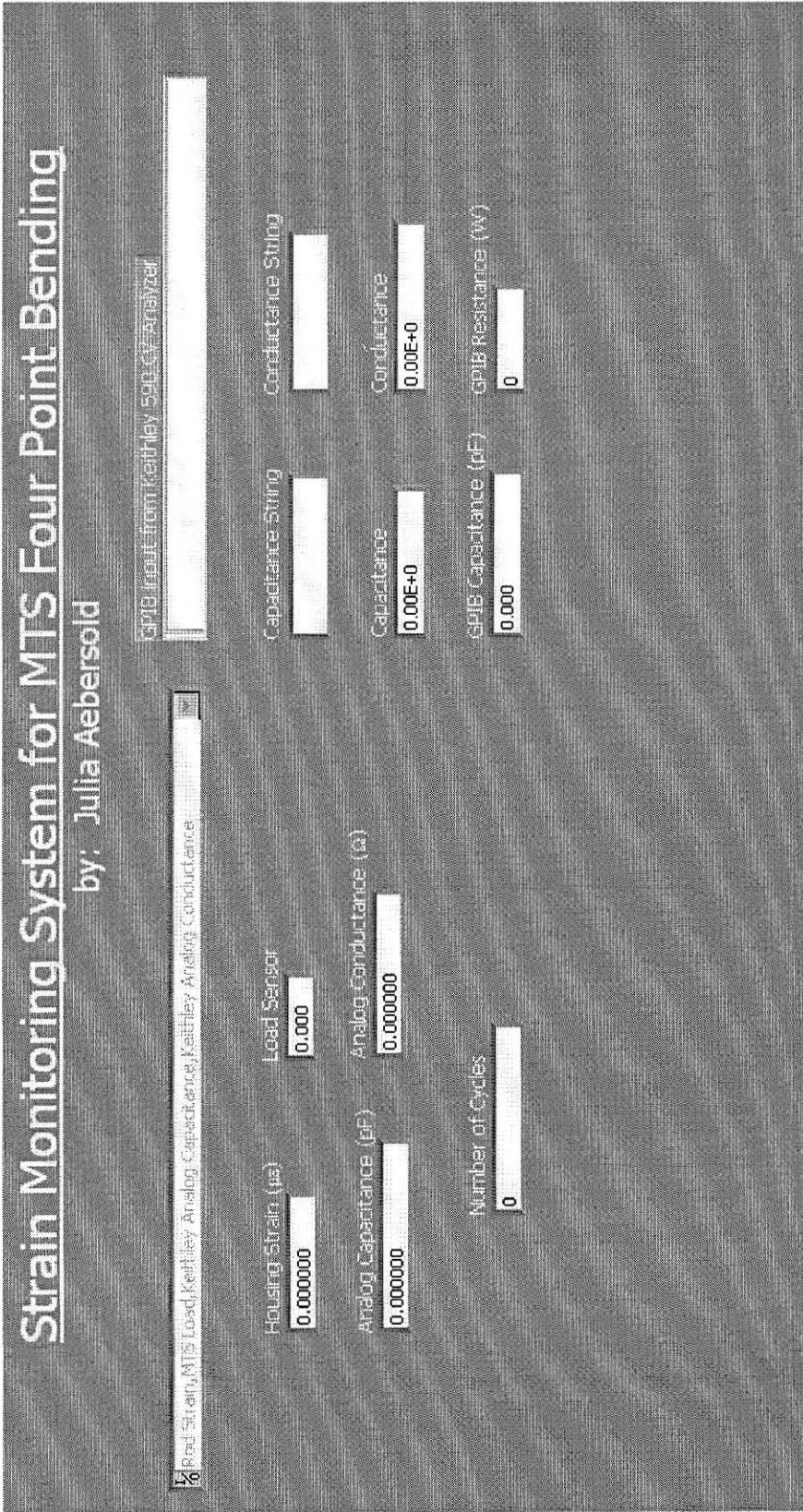


Figure 88. Illustration of the front panel for the LabView data collection program.

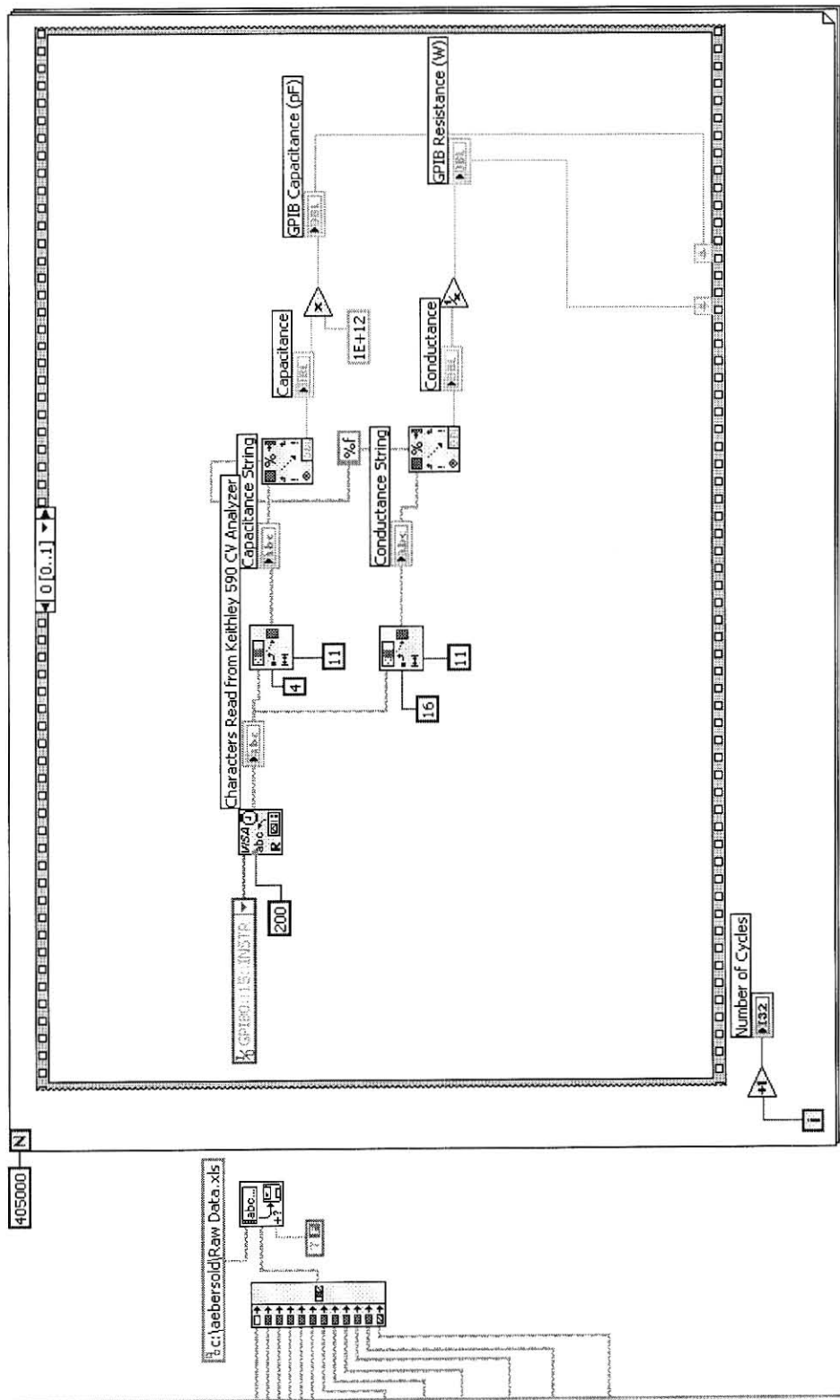


Figure 89. Illustration of frame 1 from the LabView diagram used to collect data from the capacitance bending strain sensor and strain gages.

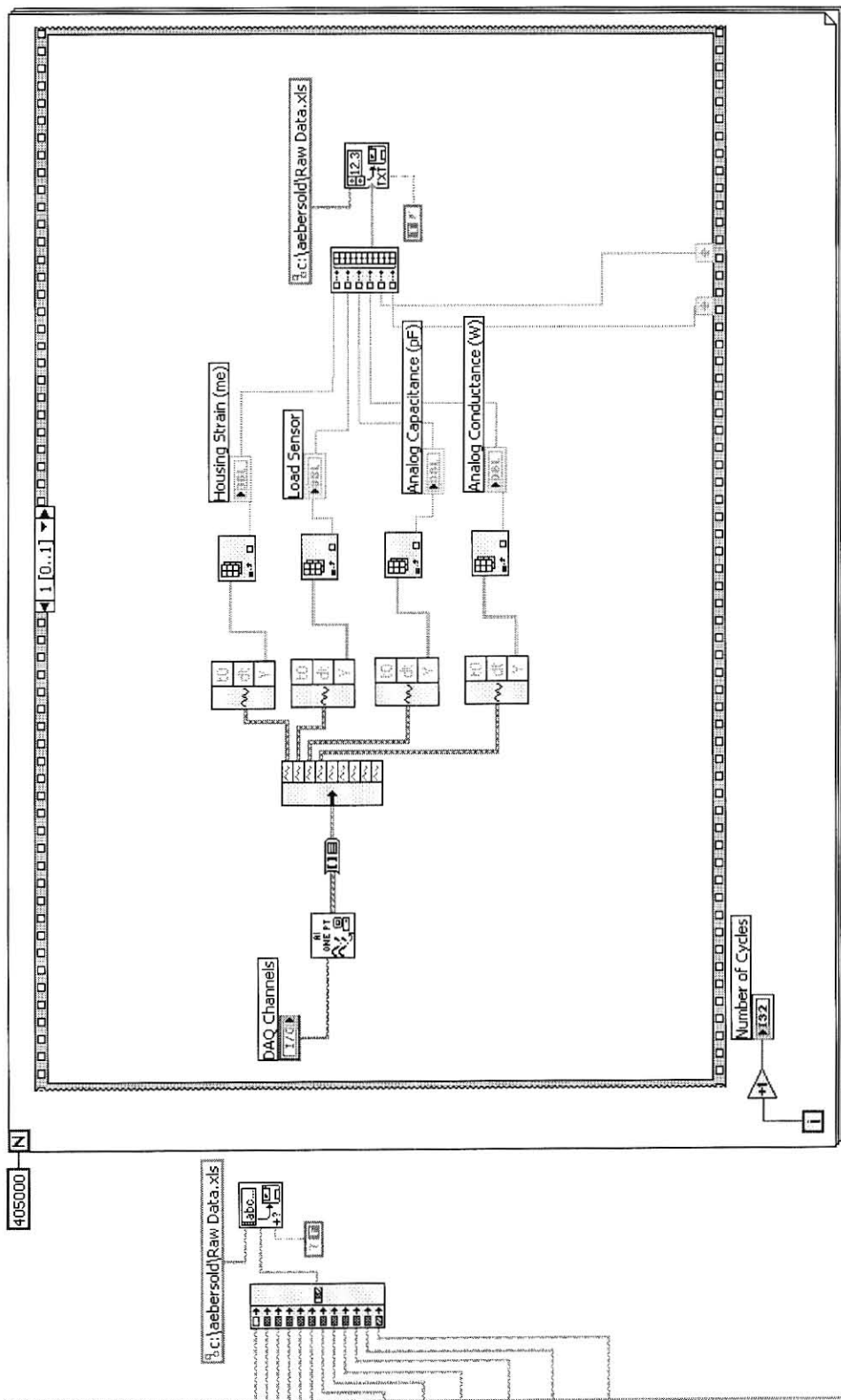


Figure 90. Illustration of frame 2 from the LabView program used to collect data from the capacitance bending strain sensor and strain gages.

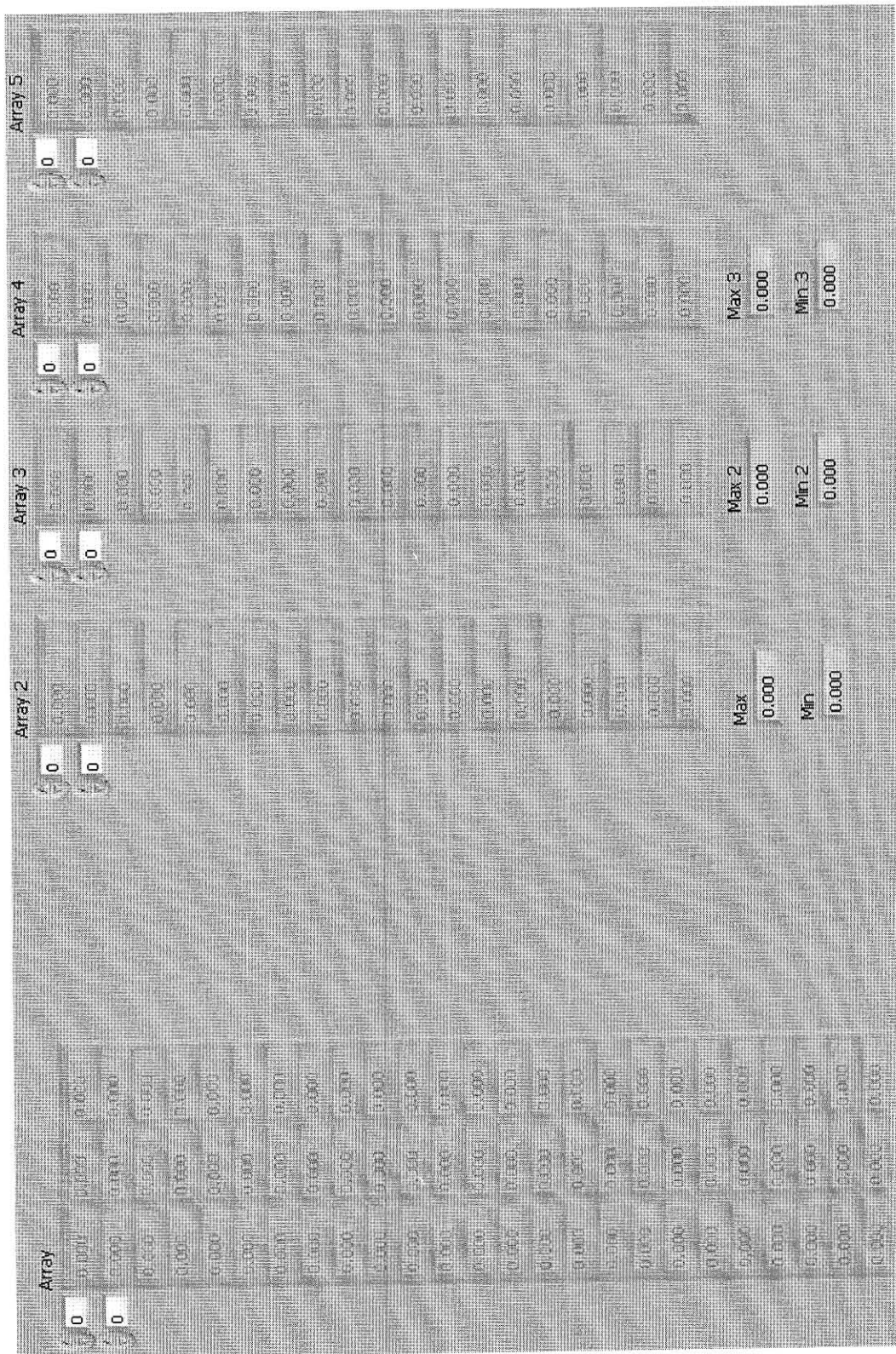


Figure 91. Front panel of the LabView program that retrieved the maximum and minimum data values from each cycle.

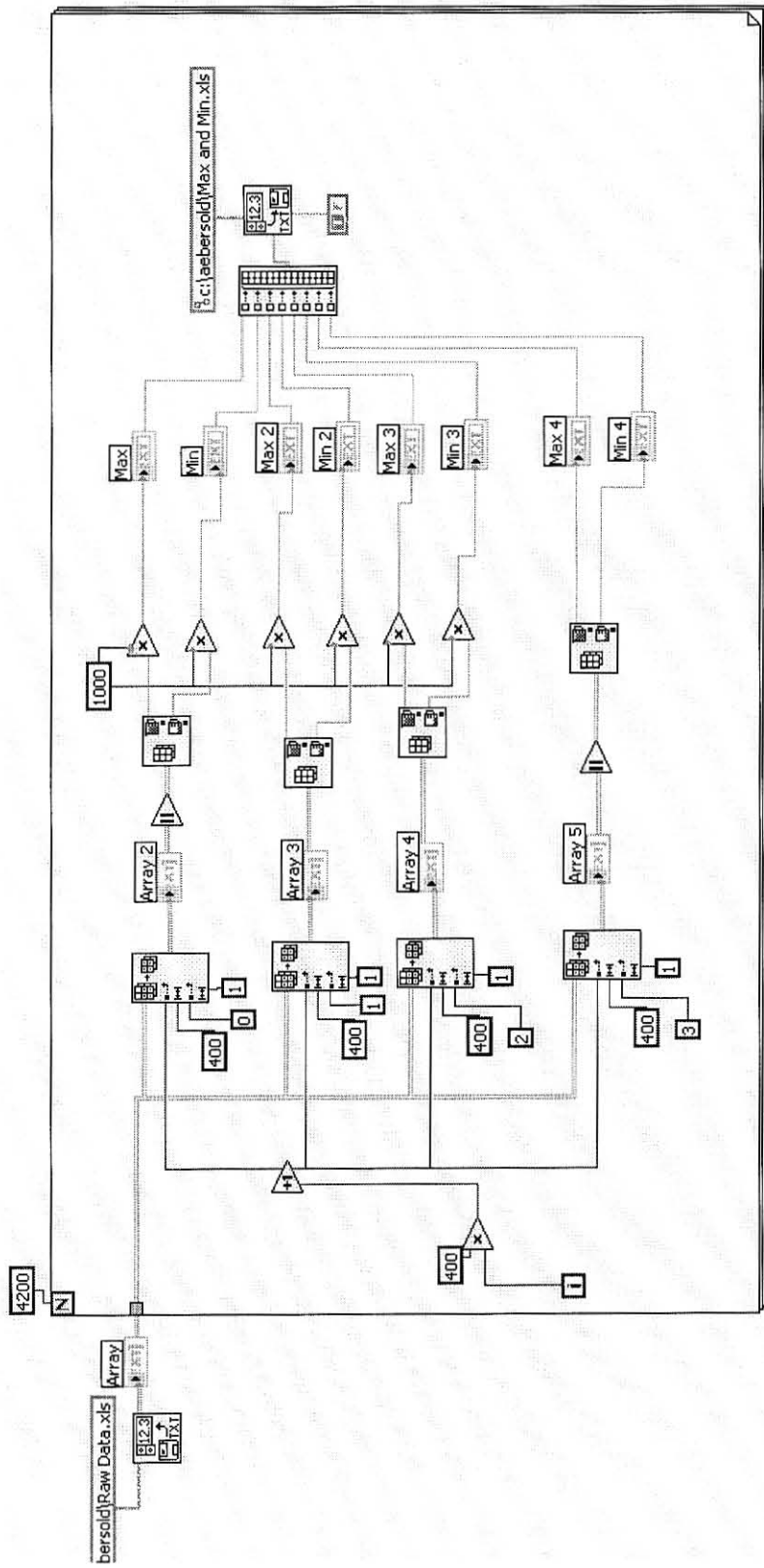


Figure 92. Diagram of the program used to retrieve maximum and minimum values from each data cycle

3.3.2 Results

Presented in this section are results gathered from the ABAQUS finite element model and the MTS testing results. The ABAQUS model specifically tested a variety of anchor geometries for the sensor, where the selected anchor design was determined by a ratio analysis of beam strain versus stress.

The sensor was fabricated and tested in four-point bending in the MTS to understand immediate and long term behavioral characteristics. The first derivative was performed on each sensor's capacitive response to determine which device was most sensitive and in what part of the strain range.

3.3.2.1 ABAQUS Finite Element Modeling Results of the Final Sensor

Analysis of the borosilicate glass became important to ensure that generated principal stresses did not exceed its tensile strength. Figure 93 shows the top of a single glass pad with stress concentrations developed at the bottom edge of the pad. A stress gradient is apparent on the vertical sidewall of the pad, where the greatest magnitude of stress occurred at the interface between the glass pad and the bottom of the anchor. Increasing the height of the pad also directly affected the amount of actuation experienced by the sensor by further displacing the fingers. This was attributed to an increase in the distance from the neutral axis of the rod to the plane of actuation, which provided a higher capacitance for given bending strain. Figure 93 shows that the

maximum principal stress developed in the pad was well below the tensile strength of 6.8 MPa.

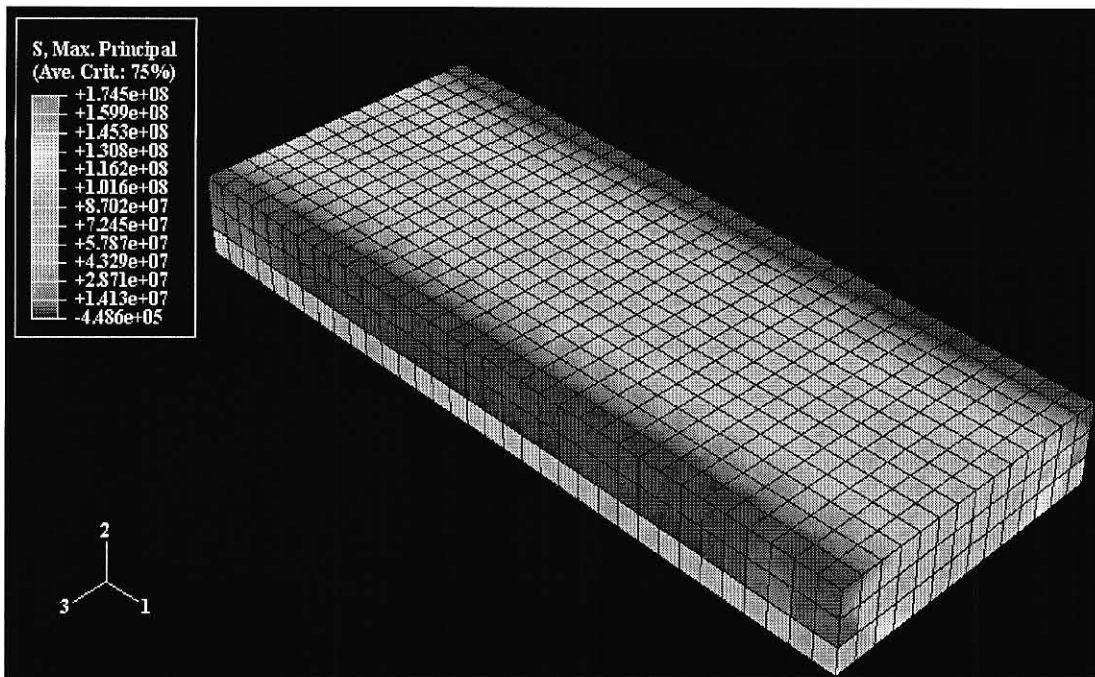


Figure 93. Max principal stress of a single glass pad attached to the beam. Stress along the sidewall reduces from the beam to the top of the glass pad.

Modeling data was collected and tabulated to review the amount of actuation, generated stress and the change in capacitance. The maximum principal stress from each model did not exceed the fracture strength of silicon of 7 GPa, which would result in material failure. Different anchor configurations were compiled by calculating the ratio of beam strain versus the generated maximum principal stress, as shown in Table III.

Model Name	Initial Capacitance (pF)	Initial Spacing Between Fingers	Substrate (glass or beam)	Final Beam Strain ($\mu\epsilon$)	Maximum Principal Stress (MPa)
Sensor-85	10.15	25 μm	Beam	766	532
Sensor-86	10.15	25 μm	Beam	766	712
Sensor-91	10.15	25 μm	Beam	766	474
Sensor-92	10.15	25 μm	Beam	766	349
Sensor-94	10.15	25 μm	Beam	766	1151
Sensor-95	10.15	25 μm	Beam	766	4197
Sensor-96	10.15	25 μm	Glass	890	279
Sensor-97	10.15	25 μm	Glass	890	1118
Sensor-98	10.15	25 μm	Glass	890	196
Sensor-99	10.15	25 μm	Glass	890	144

Model Name	Strain ($\mu\epsilon$) Stress (MPa)	Final Small Spacing Between Fingers (μm)	End Vertical Displacement (μm)	Final Capacitance	$\Delta C/C$
Sensor-85	1.44	10.5	13	13.95	37.43%
Sensor-86	1.08	10.7	15	13.55	33.54%
Sensor-91	1.62	11.1	13	13.40	32.01%
Sensor-92	2.19	10.9	12	13.67	34.74%
Sensor-94	0.67	10.7	15	13.55	33.54%
Sensor-95	0.18	10.7	14	13.65	34.54%
Sensor-96	3.19	10.6	12	13.95	37.49%
Sensor-97	0.80	10.7	11	13.96	37.56%
Sensor-98	4.54	10.7	12	13.86	36.56%
Sensor-99	6.18	11.2	11	13.51	33.11%

Table III. Information collected from each of the ABAQUS models.

Figure 94 demonstrates the resulting actuation of the device with displacement in the 2 and 3 axial directions for the Sensor-96 ABAQUS model.

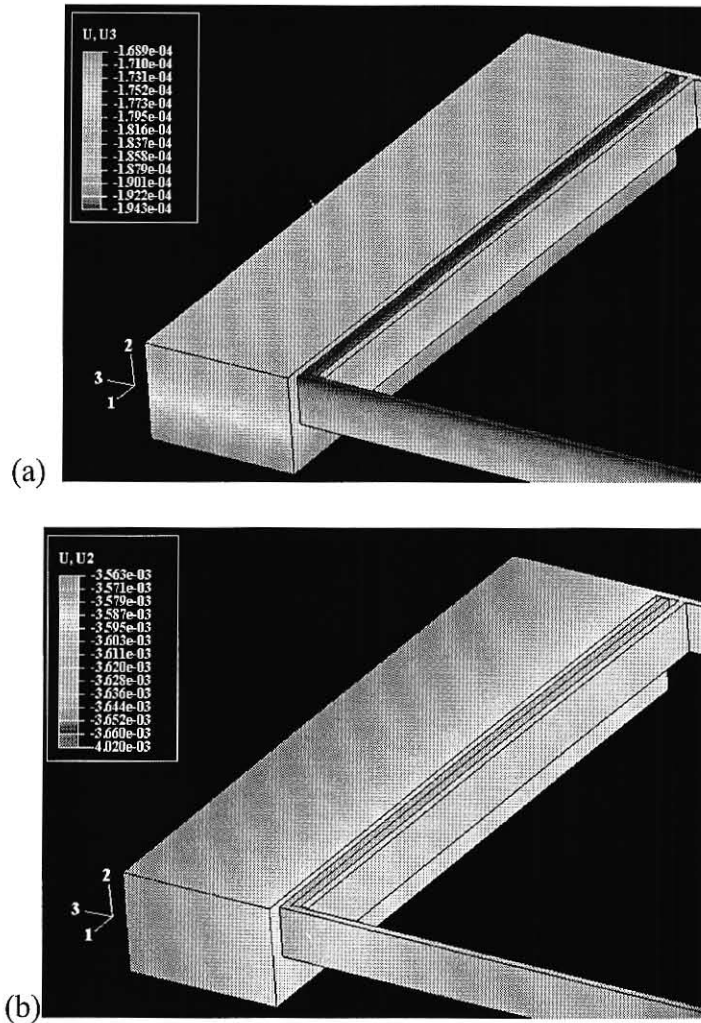


Figure 94. Actuation of the sensor from the ABAQUS model Sensor-96 (a) transverse actuation of the model with a $10.6 \mu\text{m}$ final narrow gap (b) $12 \mu\text{m}$ vertical displacement of the sensor.

3.3.2.2 MTS Testing Results of the Final Sensor

Visual observations of the sensor are shown in Figure 95. The first photograph, Figure 95a, shows equal spacing of the fingers before actuation. Figure 95b shows movement of the interdigitated fingers after a load was applied to the beam. Figures 95c and 95d show vertical displacement of the fingers as predicted in Figure 81.

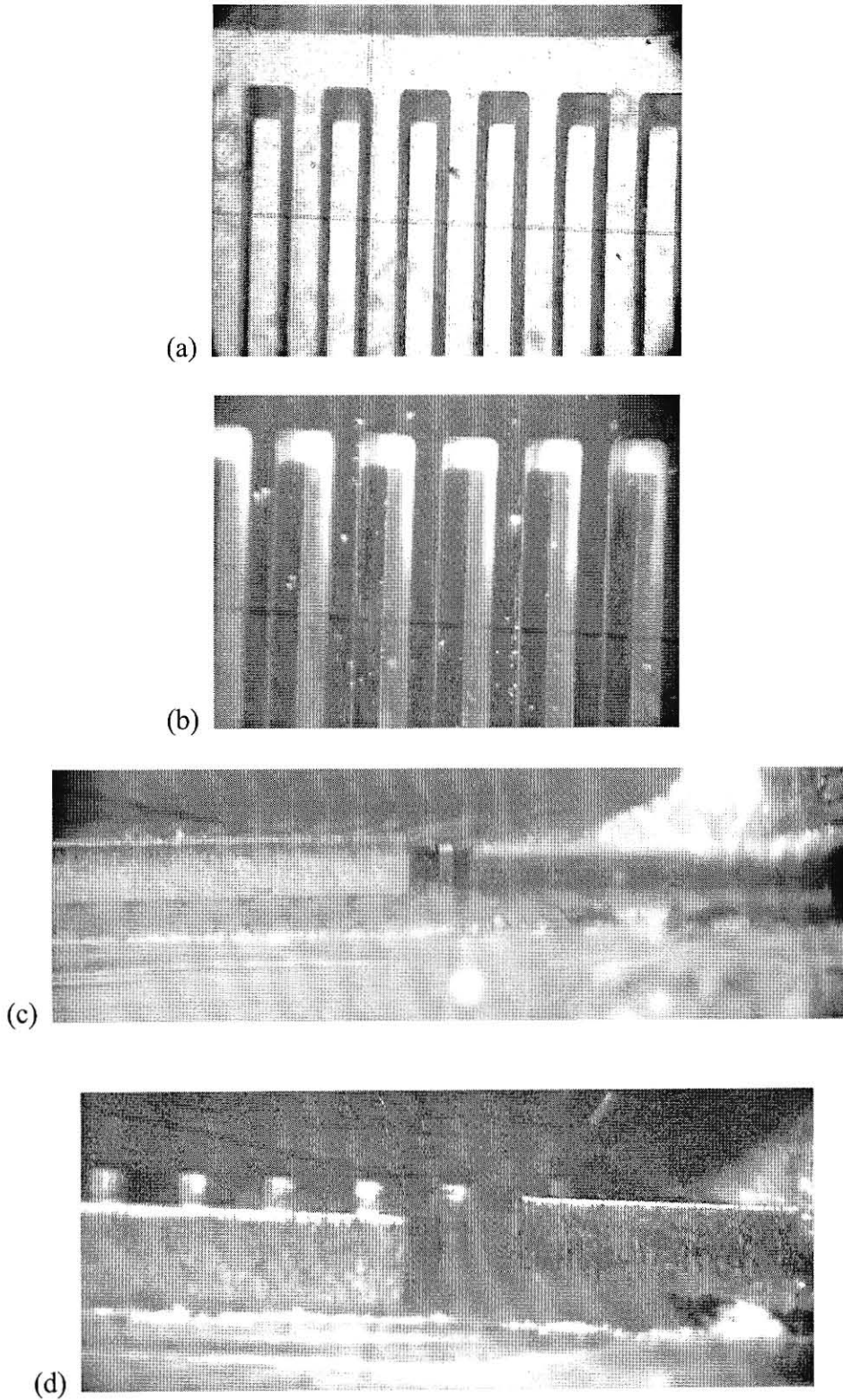


Figure 95. A graphical illustration of the interdigitated fingers of the sensor (a) before bending strain is applied. (b) After bending strain is applied the spacing between the fingers has changed considerably. (c) & (d) Vertical actuation of the sensor.

After confirmation the sensor would actuate as desired, it was connected to a CV analyzer to record capacitance and conductance data. Four sensors were tested under cycle loading with the results shown in Figures 96 through 98.

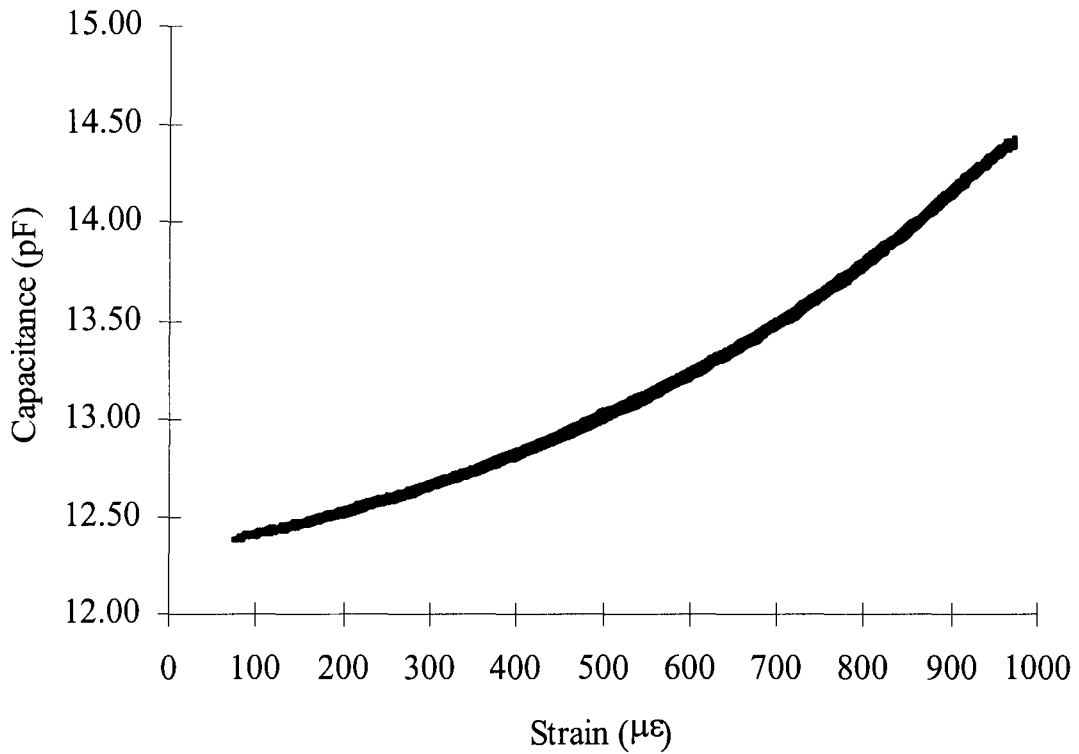
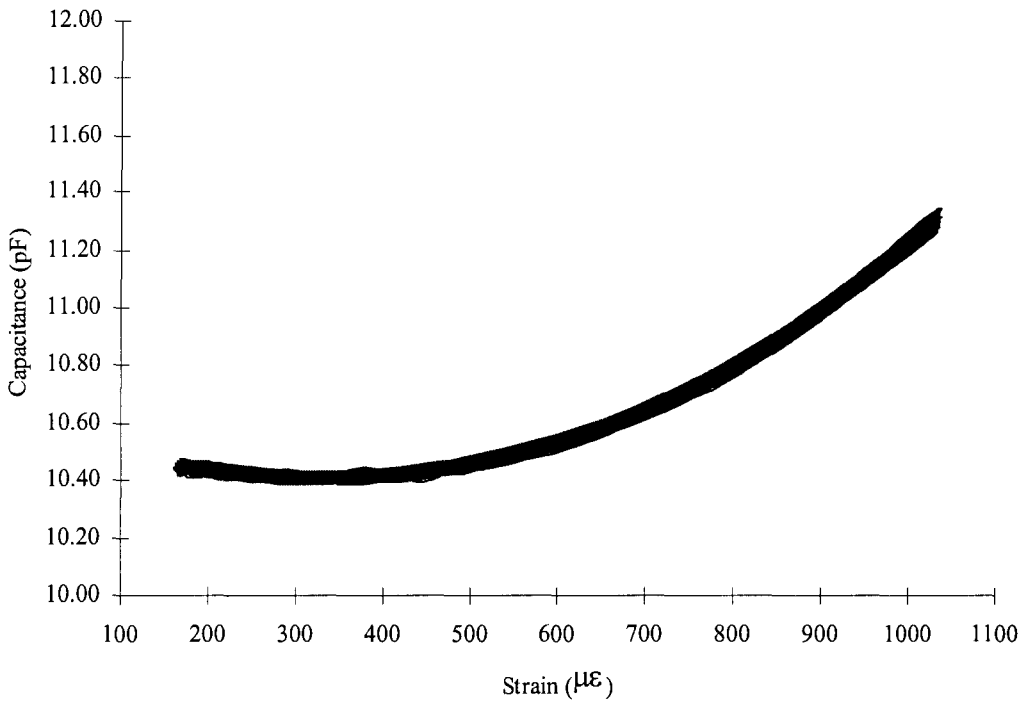
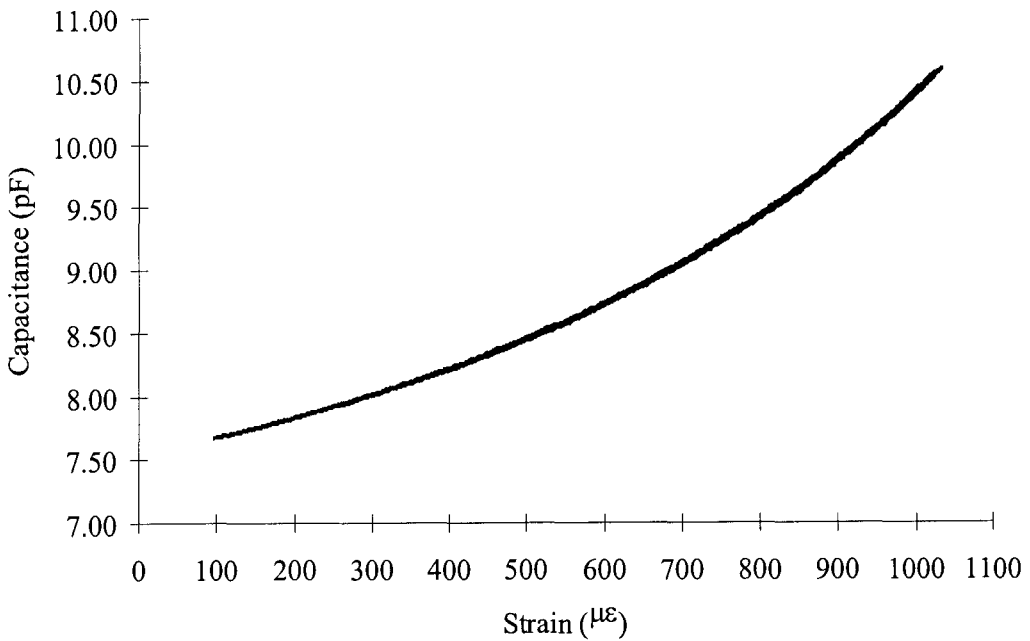


Figure 96. Graphical results of cyclical load testing for sensor 1.



(a)



(b)

Figure 97. Graphical results of cyclical load testing for (a) sensor 2 and (b) sensor 3.

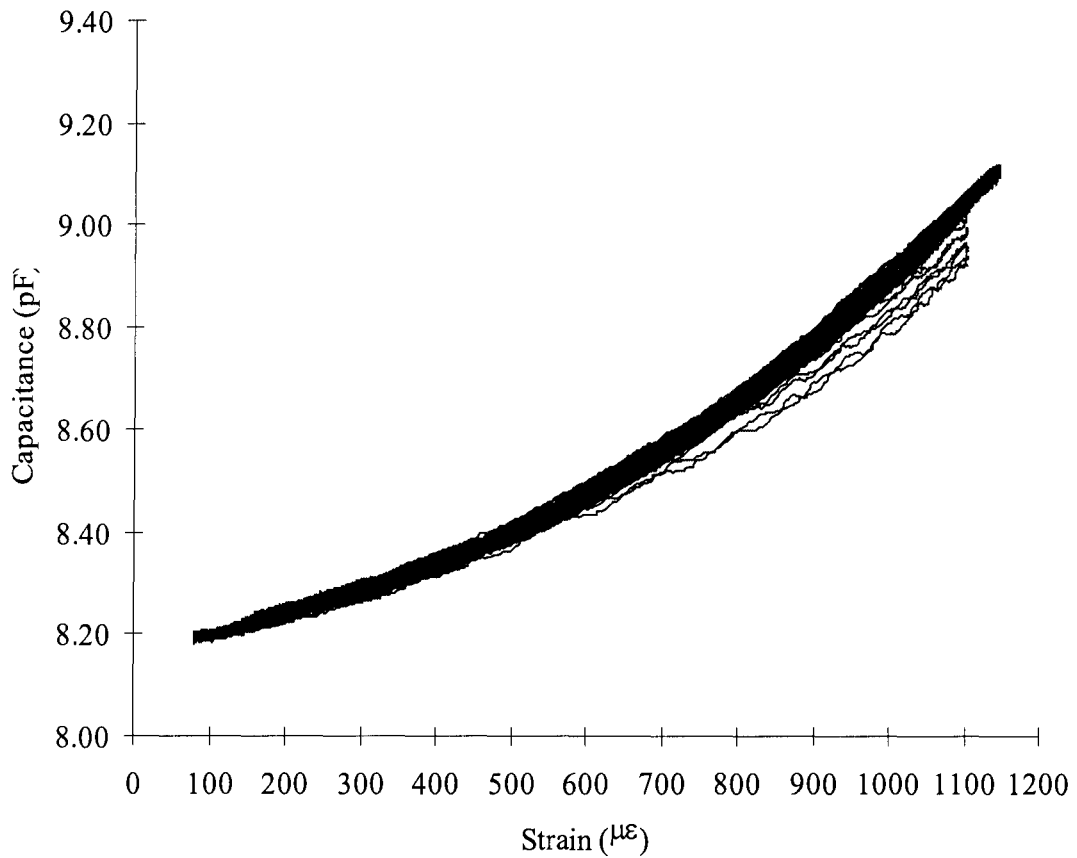
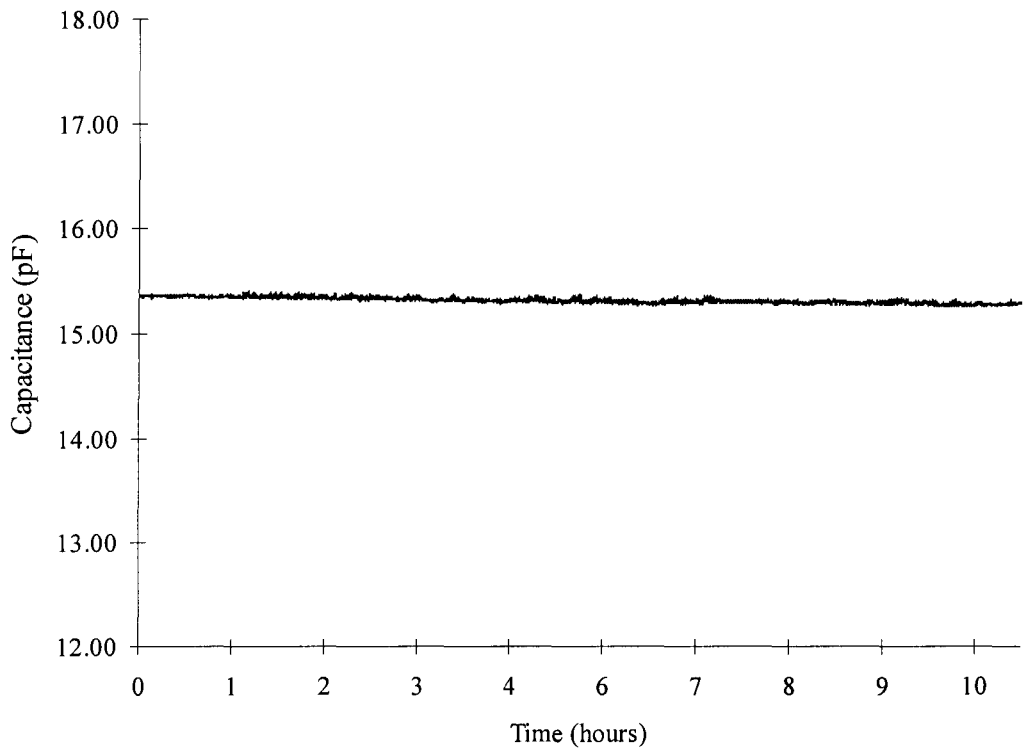
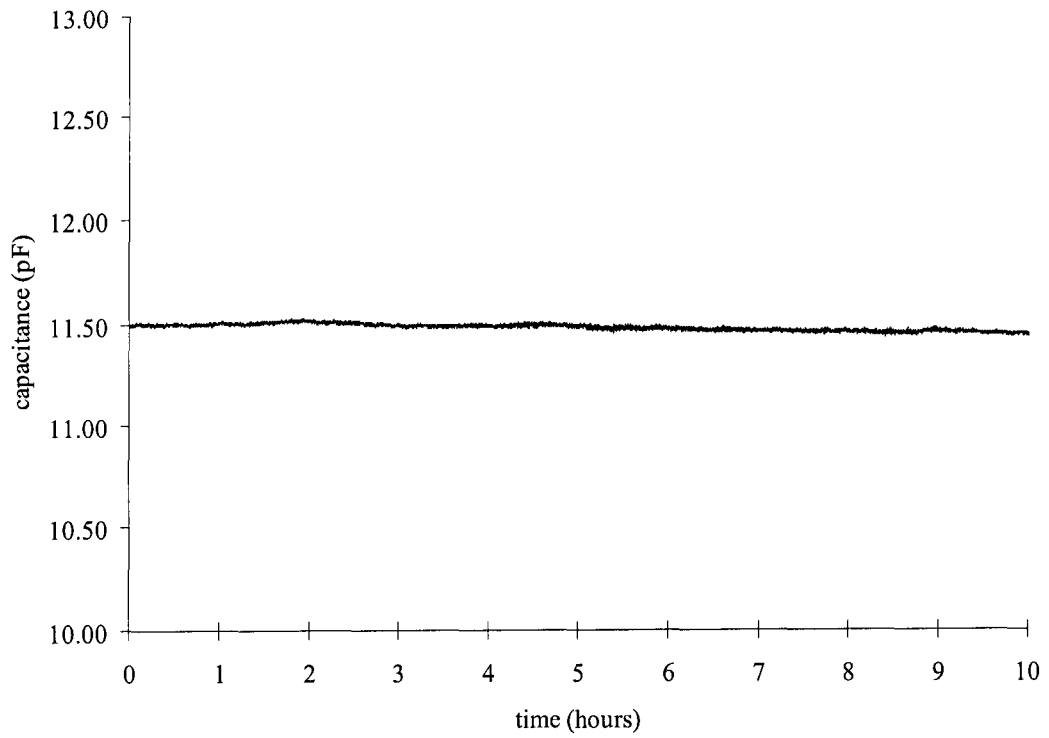


Figure 98. Graphical results of cyclical load testing for sensor 4.

Sensor drift was evaluated by applying a constant load to the beam from the MTS. Data was recorded in a similar manner as the cyclical test, but for durations of 9 hours or more. The results for the four sensors are shown in Figures 99 and 100.

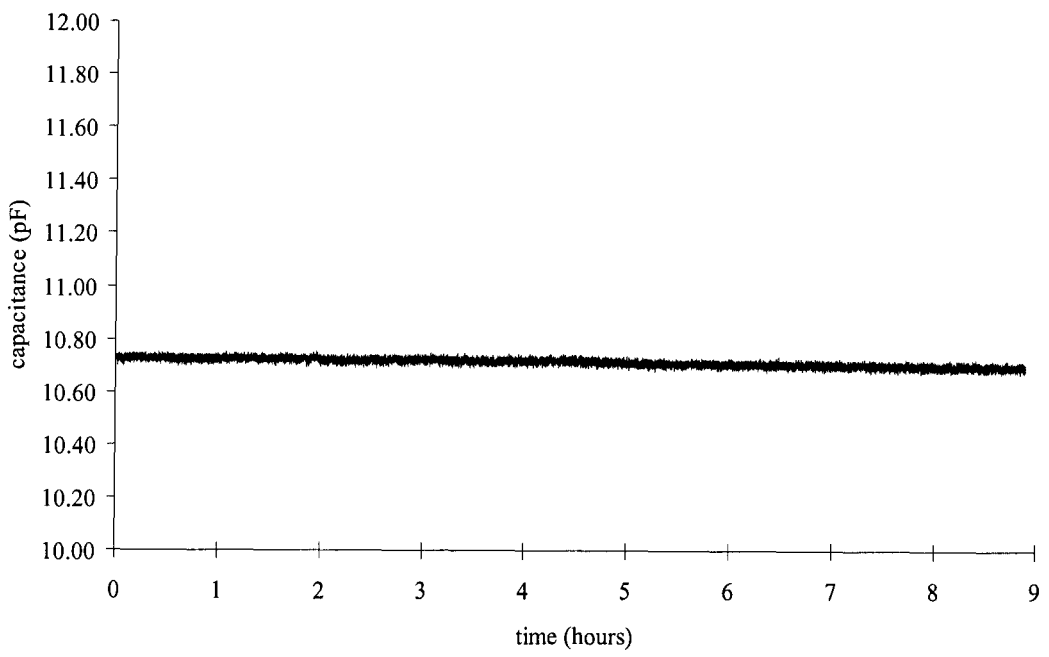


(a)

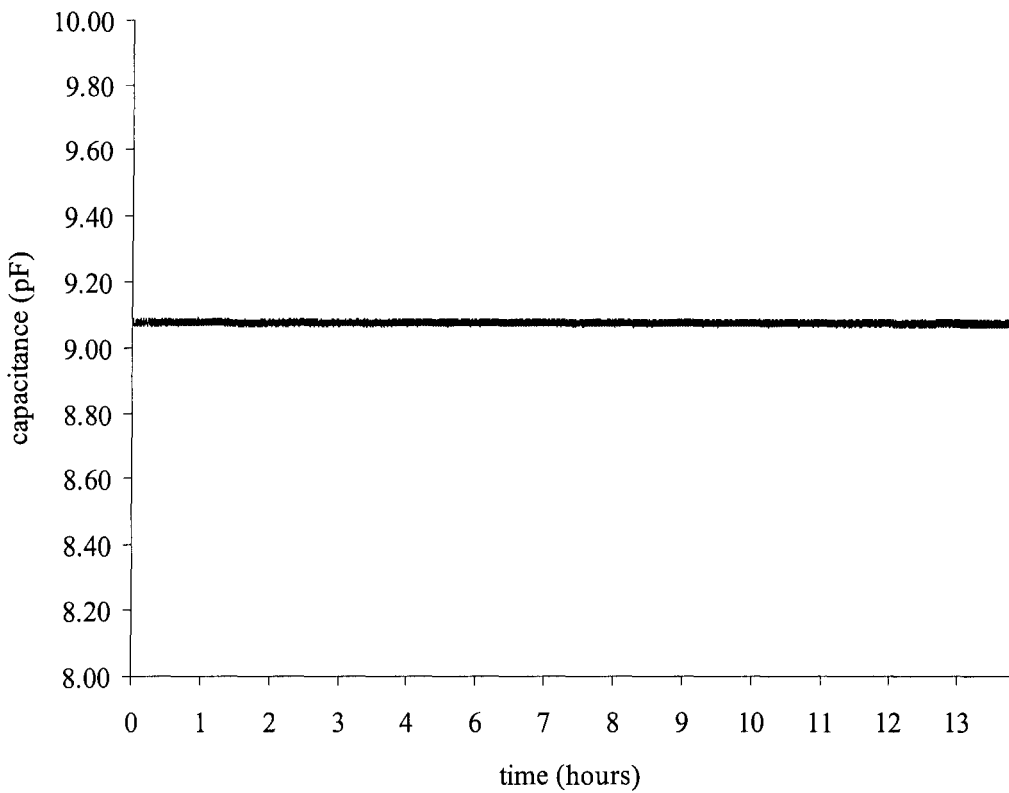


(b)

Figure 99. Graphical results of static testing from (a) sensor 1 and (b) sensor 2.



(a)



(b)

Figure 100. Graphical results of static testing from (a) sensor 3 and (b) sensor 4.

To determine maximum range of the sensor, an increasing load from the MTS was applied until maximum capacitance was achieved or conductance began to exponentially increase. This indicated that the fingers were in contact with each other and no further actuation could be achieved. Figures 101 to 103 show the capacitance versus strain response for each sensor. Response of each sensor was also measured during unloading.

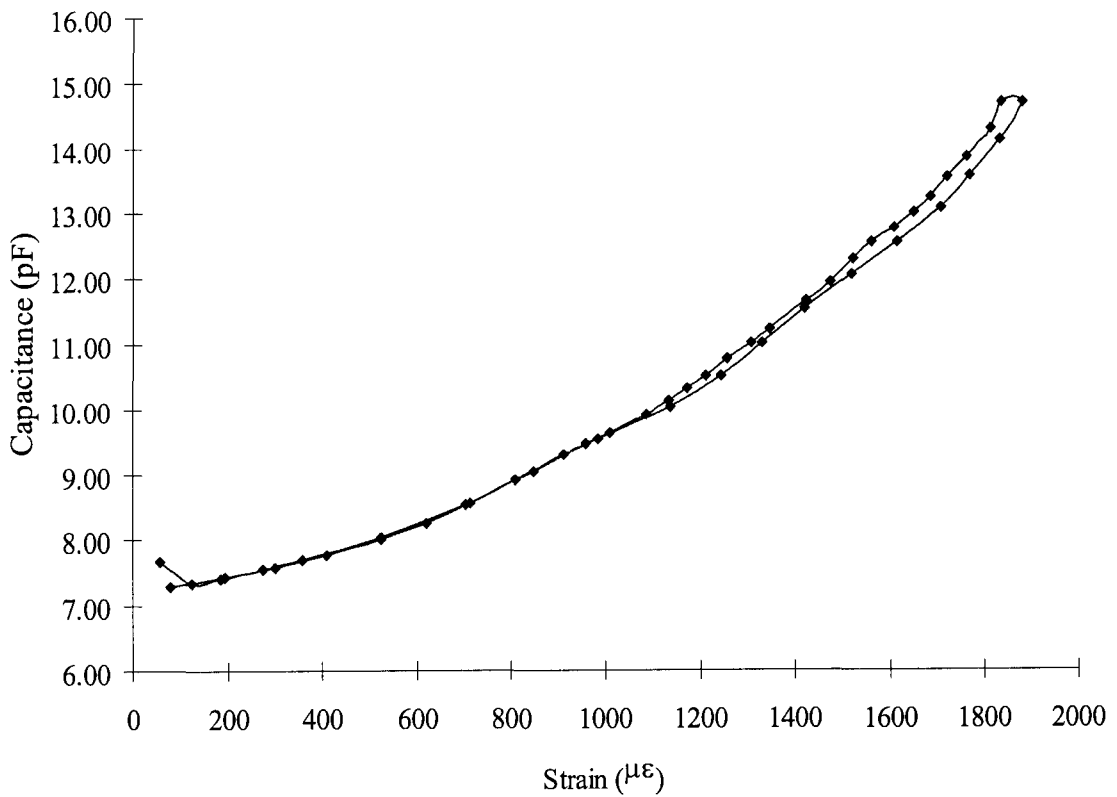
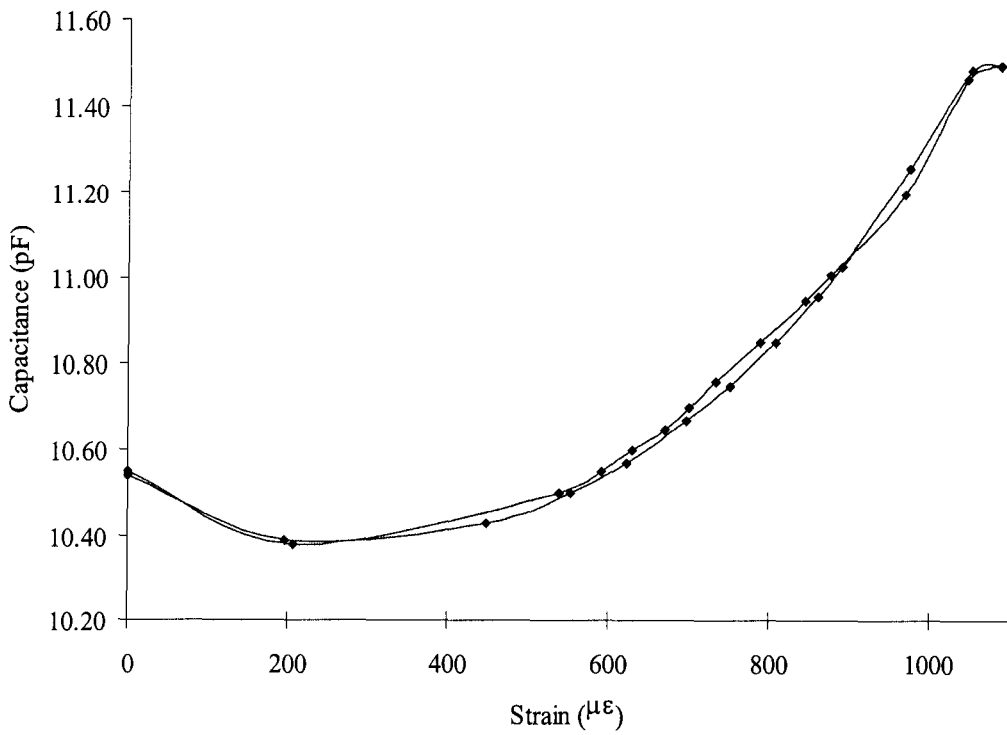
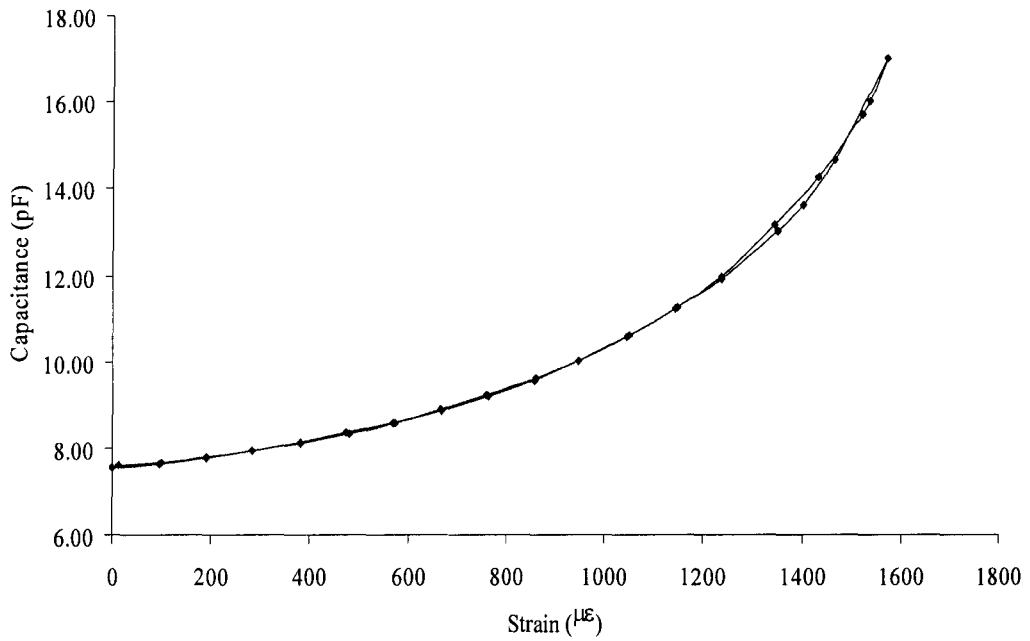


Figure 101. Graphical results of the entire capacitance range for sensor 1.



(a)



(b)

Figure 102. Graphical results of the entire capacitance range for (a) sensor 2 (b) and sensor 3.

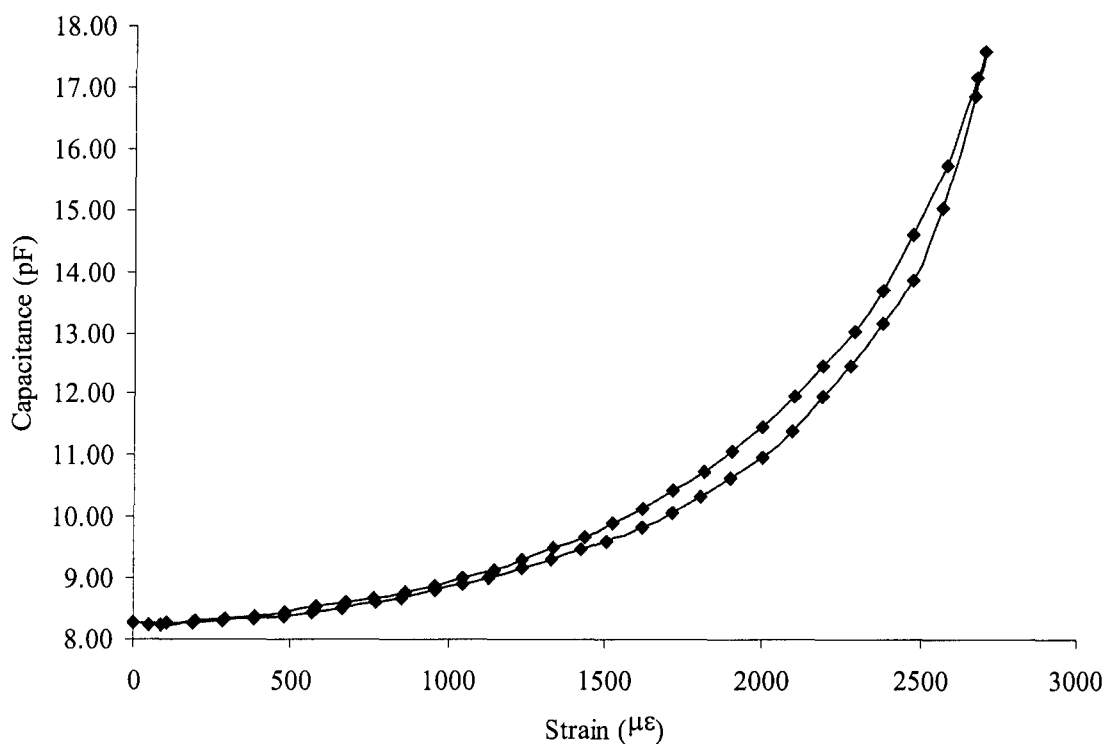


Figure 103. Graphical results of the entire capacitance range of sensor 4.

Conductance values were recorded for each sensor at zero strain and maximum strain during the maximum capacitance test and are shown in Table V.

	Initial Conductance (μS)	Final Conductance (μS)
Sensor 1	1.85	13.78
Sensor 2	4.80	22.00
Sensor 3	1.28	25.00
Sensor 4	0.85	11.30

Table IV. Initial and final conductance values from each of the sensors.

The greatest change in capacitance occurred in different regions of the strain range for each sensor. Sensor sensitivity, S , was determined using the first derivative of the sensor response given by

$$S = \frac{dy}{dx} = \frac{dc}{d\epsilon} \quad (13)$$

where c is capacitance and ϵ is strain.. TableCurve (Jandel, ver. 3.1.0) was used to curve fit the response data assuming a parabolic shape, with the results shown in Figures 104 to 106.

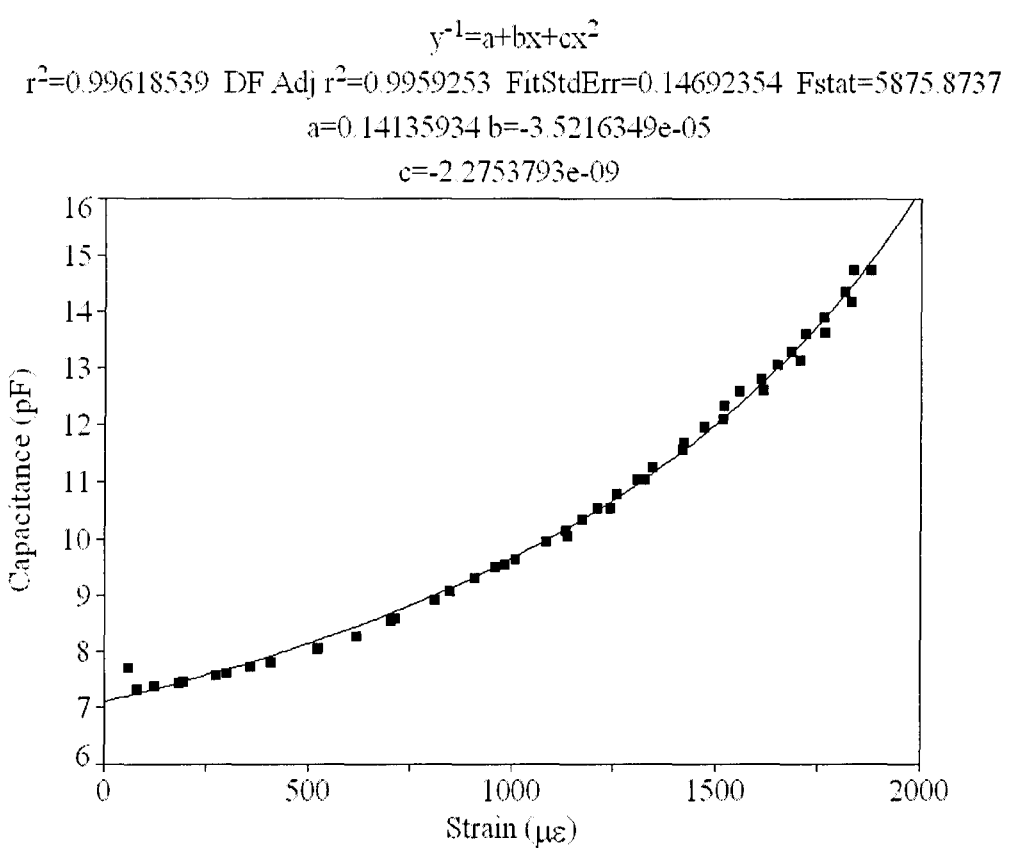
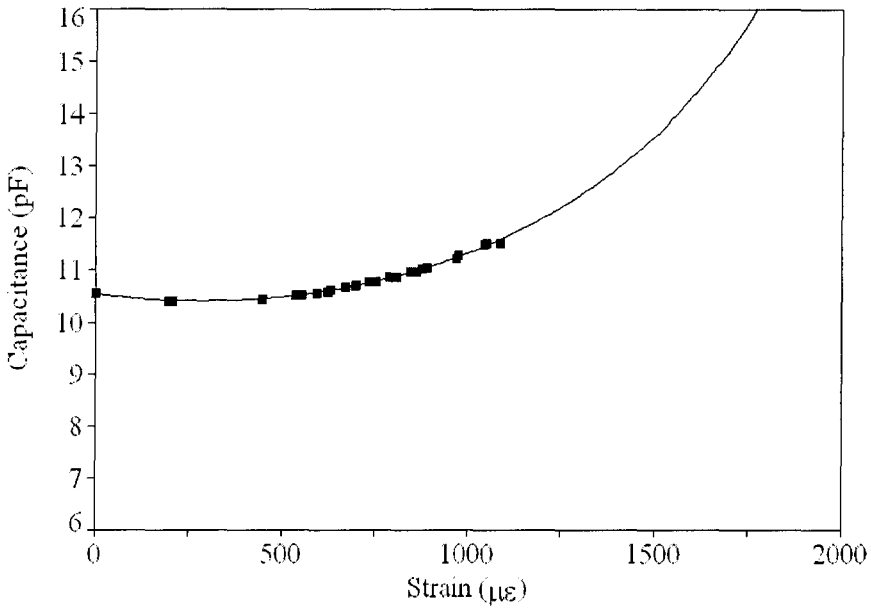


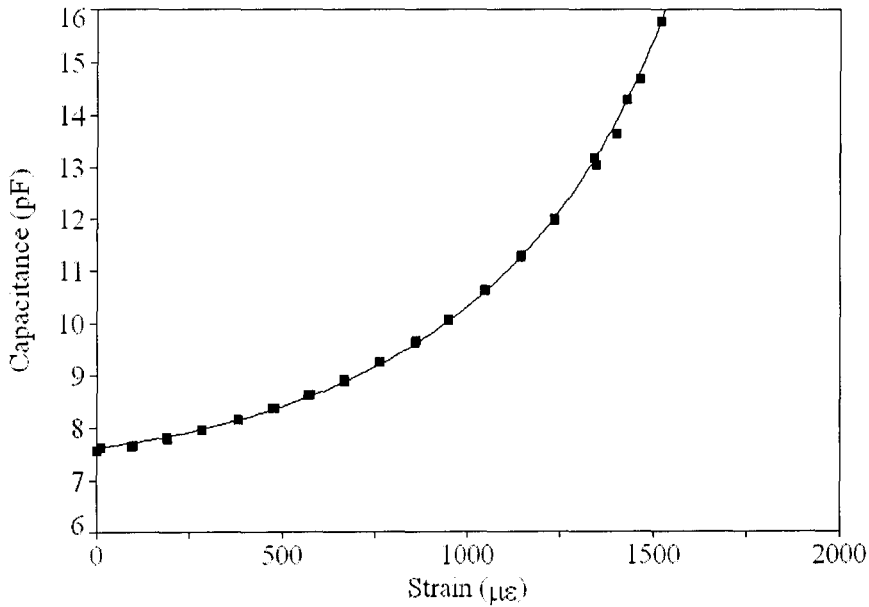
Figure 104. Curve fit graphs generated for each sensor from the maximum capacitance test from the MTS for sensor 1.

$y^{-1}=a+bx+cx^2$
 $r^2=0.99579856$ DF Adj $r^2=0.99522563$ FitStdErr=0.023148411 Fstat=2725.6557
 $a=0.094962098$ $b=8.7206544e-06$
 $c=-1.5240208e-08$



(a)

$y^{-1}=a+bx+cx^2$
 $r^2=0.999213$ DF Adj $r^2=0.99913922$ FitStdErr=0.078735474 Fstat=20949.226
 $a=0.13143581$ $b=-1.4155983e-05$
 $c=-2.0118255e-08$



(b)

Figure 105. Curve fit graphs generated for each sensor from the maximum capacitance test from the MTS for (a) sensor 2 (b) and sensor 3.

$$y^{-1}=a+bx+cx^2$$

$r^2=0.99318105$ DF Adj $r^2=0.99280911$ FitStdErr=0.21016415 Fstat=4078.2043
 $a=0.11888353$ $b=5.3849652e-06$
 $c=-1.0370947e-08$

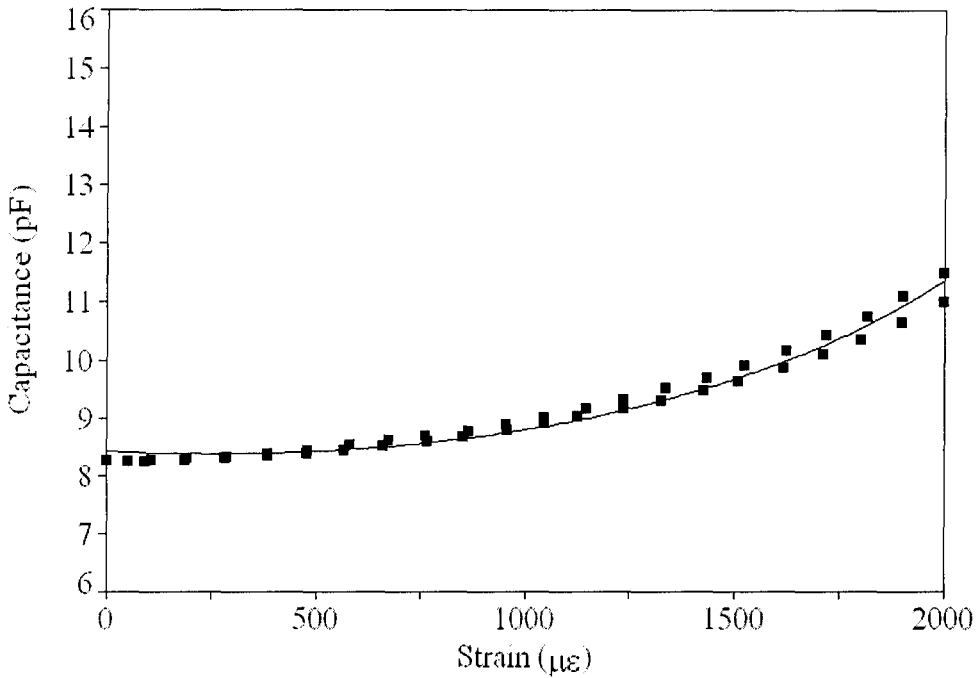


Figure 106. Curve fit graphs generated for each sensor from the maximum capacitance test from the MTS for sensor 4.

The response for each sensor was given by

$$y_1 = \frac{1}{0.14135934 - 3.5216349e-05x - 2.2753793e-09x^2} \quad (14)$$

$$y_2 = \frac{1}{0.094962098 + 8.7206544e-06x - 1.5240208e-08x^2} \quad (15)$$

$$y_3 = \frac{1}{0.13143581 - 1.4155983e-05x - 2.0118255e-08x^2} \quad (16)$$

$$y_4 = \frac{1}{0.11888353 - 5.3849652e-06x - 1.0370947e-08x^2} \quad (17)$$

where y is the capacitance in pF and x is strain in microstrain. The correlation coefficient for each curve fit was greater than 0.99.

Figure 107 shows the sensitivity for the measured strain range and Figure 108 for the 0 to 1200 $\mu\epsilon$ range.

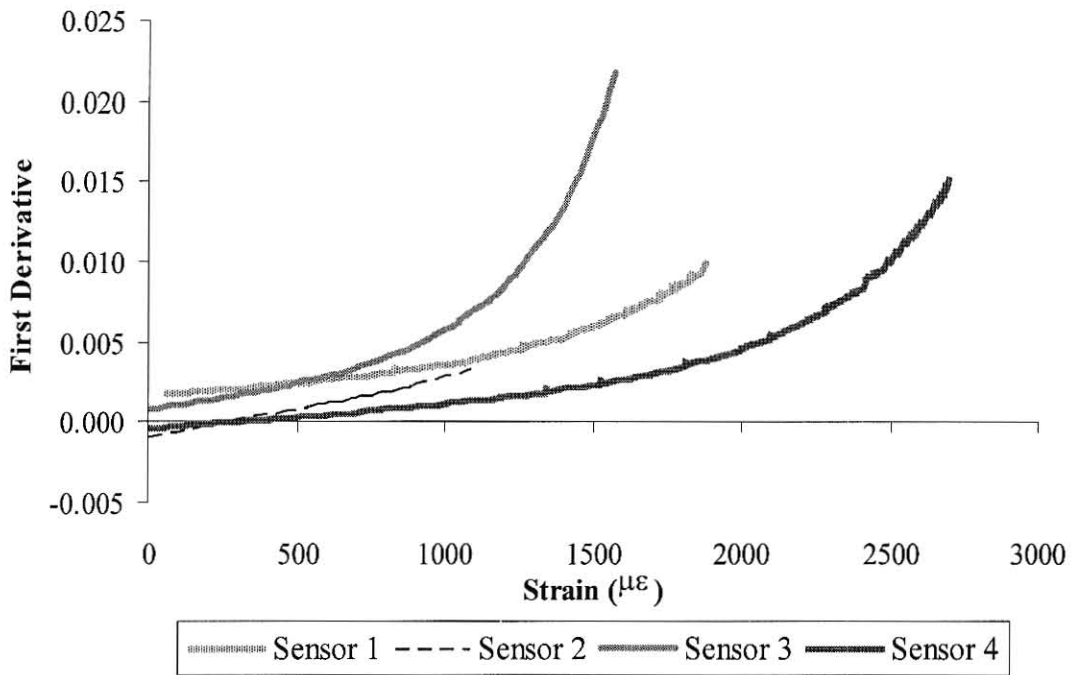


Figure 107. Sensitivity for each sensor over the measured strain range.

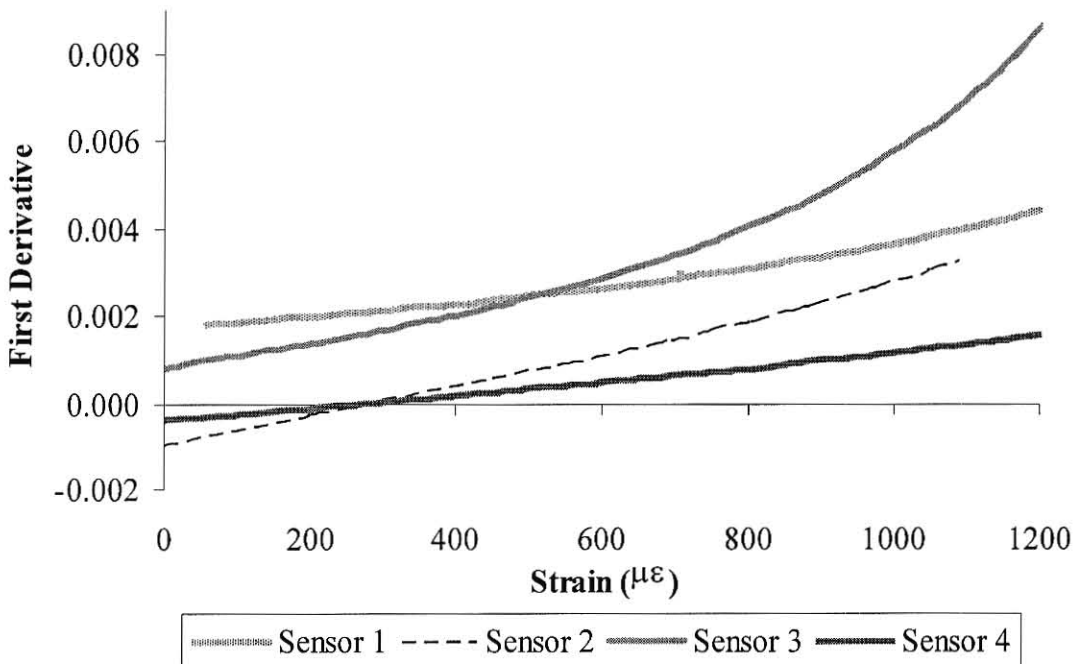


Figure 108. Sensitivity over the 0 to 1200 $\mu\epsilon$ range.

3.3.3 Discussion

ABAQUS modeling, MTS testing and curve fit data was collected and presented in the previous section. Modeling results were used to determine which of the designs was selected for fabrication. MTS testing results showed the range of response, whether hysteresis was present and if the fingers were equidistant from each other prior to sensor actuation. Curve fit data was used to determine which sensor was most sensitive and in what region of the strain range.

ABAQUS models were used to develop and design the sensor. Results from the model produced a ratio of strain compared to generated stress. A resulting higher ratio indicated a design that generated a low amount of stress for large amount strain at the anchor beam to sensor interface.

The sensor was fabricated in a class 100/1000 clean room from the results of the ABAQUS generated ratio. Previously established testing protocol performed on the housing was used similarly on the sensor to give cycle, static and maximum MTS loading test results. These results were scrutinized for hysteresis, drift and range of response.

Data from the maximum loading test gave graphical information that was used to develop parabolic equations to match the data to a level that was consistent for each sensor. From these developed equations, the first derivative was taken to determine which device was most sensitive and where in the strain range. Not one sensor dominated sensitivity over the entire strain range. This is one area that requires improvement to produce sensors with similar sensitivities.

3.3.3.1 Discussion of the ABAQUS Finite Element Model of the Final Sensor

Model results for the different anchor designs from Table III were encouraging since none of the designs developed a maximum principal stress that exceeded the fracture strength of silicon. Also, the ratio of strain versus stress showed how application of a glass pad to the bottom of the anchor reduced the maximum principal stress developed in the sensor. The glass pad also helped during attachment of the sensor to the bar by providing adequate surface area to apply an adhesive. The amount of surface area of the anchor and its direction also directly correlated to the level of stress developed in the anchor.

The array of small blocks in Sensor-95 developed a high level of stress in each block. The anchor area was doubled for Sensor-96, however, the half anchor of Sensor-98 proved to be a more efficient sensor as shown by the strain to stress ratio of 4.54. The reduction of area in the longitudinal direction also increased this ratio. This is also supported by results from Sensor-94 and Sensor-98. Therefore, the most efficient strain versus stress configuration was Sensor-98. However, Sensor-96 produced a higher change in capacitance with only a slightly lower strain to stress ratio and was selected for fabrication.

Sensor-98 and 99 are similar designs with the exception that the glass pad thickness was increased to 500 μm from 300 μm . Results of these two designs show that the thicker pad is more beneficial due to further actuation or displacement of the sensor. Increasing the distance from the neutral axis to the plane of actuation will result in a higher amount of bending strain.

For each sensor mounted to the glass pad, the amount of vertical actuation was comparable to calculations, yet, had a relatively small effect on the final capacitance. However, when consideration was given to the strain to stress ratio and ease of fabrication, the final model selected was Sensor-96 with a glass pad 500 μm thick applied to the bottom of the anchor.

Analytical results were compared with the ABAQUS FEA model to validate accuracy of the modeling results, short of fabricating the device. Table IV shows a comparison of both results with a difference of 0.60 pF for the final capacitance.

	Final Narrow Gap	Height Actuation	Initial Capacitance	Final Capacitance	$\Delta C/C$
Analytical Calculations	12.40 μm	1.16 μm	10.15 pF	13.35 pF	31.53%
Sensor-96	10.60 μm	12.00 μm	10.15 pF	13.95 pF	37.44%

Table V. Analytical and ABAQUS modeling results of Sensor-96.

3.3.3.2 Discussion of the MTS Testing Results of the Final Sensor

The response for each sensor showed little variation between loading and unloading in the MTS. One exception was sensor 4 where artifacts appeared near the end of the test. It is surmised that this was attributed to a small degree of movement of the bar in the MTS fixture where an uneven load was applied to the beam. This created a strain differential experienced by the sensor and strain gages recorded by LabView.

A minimal amount of change was seen during the static load test. However, the small fluctuations were not attributed to drift, but to small changes in the load applied by

the MTS. This was evident from the load cell and strain gage data recorded simultaneously when compared to the sensor's output. As a result, each of the sensors did not exhibit drift.

Each of the sensors exhibited a repeatable capacitive response as the MTS load was reduced, with exception to sensor 4. Slight variations were noticed that may have been attributed to high loads applied to the fixture where the yield point of the beam or of the fixture was exceeded. All of the other sensors returned to their original capacitance levels at a zero load.

Sensor 1 was the most sensitive device for 0 to 500 $\mu\epsilon$ for the magnitude of the slope was greatest. However, at 500 $\mu\epsilon$ the most sensitive device was sensor 3 for 500 to 1200 $\mu\epsilon$. Discrepancies for the response and sensitivity of each sensor were attributed to minute differences during the fabrication process. As a result, the initial spacing between the fingers of each sensor was different and accounted for a different initial capacitance. Also, the beginning of actuation for each sensor was different along the capacitive profile. Sensor 2, from Figure 97a, shows what occurs when spacing on either side of the interdigitated fingers was not equal. During initial loading, capacitance values decrease and increase again after the finger spacing becomes equal. Unequal spacing of the fingers developed after the sensor was applied to the beam.

Tethers were used to attach both anchors until the sensor was adhered to the steel beam. After curing the adhesive, residual stress developed in the sensor until the tethers were broken and allowing free and independent movement of the fingers. However, on a few occasions the spacing between the fingers was not uniform once the tethers were

broken. This led to a change in the response of the sensor and was attributed to accidentally over-etching the bottom of the wafer while creating the anchors.

The oxide used as a mask layer for the bottom of anchors was removed by KOH by leaving the wafer in the solution too long. As a result, the bottom of the anchors was etched creating a non-uniform surface. During anodic bonding, the glass pads became non-parallel to the longitudinal axis of the sensor. When the sensor was applied to the beam, the glass pads were forced to conform to the shape of the flat beam and created residual stress in the device. After breaking the tethers the residual stress caused the independent sides of the sensor to move changing the spacing on either side of the fingers. This error can be avoided by not etching beyond the oxide layer and gaining further experience by fabricating more devices.

This would yield a sensitive curve similar in shape and magnitude for each sensor. To accurately compare each sensor requires similar spacing between the interdigitated fingers. However, non-equivalent spacing could be beneficial to the development of the sensor to indicate whether positive or negative bending strain was occurring. If spacing between the fingers is uniform before bending strain is applied then direction of the bending strain could not be determined.

4.0 CONCLUSIONS AND RECCOMENDATIONS

A housing and sensor were successfully developed for use with a telemetric strain monitoring system to assist orthopaedic surgeons with objective data to determine the presence of spinal fusion. The following are conclusions achieved from the design, modeling, fabrication and testing of the housing.

1. The housing model developed in ABAQUS amplified rod strains on the sensor surface.
2. The loading and boundary conditions applied to the ABAQUS model successfully developed a constant magnitude of strain on the surface of the rod.
3. The housing design met the established design criteria of biocompatibility, size, material properties and ease of installation.
4. Four-point bending in the MTS was an effective method of emulating rod loading in the lumbar spine.
5. The housing transferred and amplified rod strains to the sensor surface.
6. The housing did not exhibit any long-term behavioral problems of creep or hysteresis.

Recommendations for the housing include alternative methods of clamping for cost reductions. The Atlas Cable System manufactured by Medtronic Sofamor Danek could be replaced with cheaper mechanisms. These would need to be suitable for

implantation and apply at least 20 MPa of uniform pressure to the cable guides.

Specialized tooling to secure a different mechanism may also be required.

For complete implantation of the system a cover must to be designed to protect and hermetically seal the sensor and telemetry circuitry. One technique that has been investigated on a limited basis is ultrasonic welding. This application applies a high frequency, yet low amplitude oscillations and pressure on two contacting components causing them to fuse at their interface [83, 84]. However, humidity testing must be investigated and whether the frequency applied by the welding process would be detrimental to the internal components to cause failure.

The following conclusions were derived from development of the sensor.

1. The sensor model developed in ABAQUS emulated longitudinal and vertical actuation of the fabricated sensor.
2. The loading and boundary conditions applied to the ABAQUS model successfully developed a constant magnitude of strain on the surface of the beam.
3. The sensor design met the size constraints and initial capacitance requirements of the telemetry circuitry.
4. Response for each sensor was below the change in capacitance criteria for the telemetry circuitry.
5. Each sensor did not exhibit any drift characteristics during static testing.
6. Each sensor did not exhibit any hysteresis during cycle testing.
7. Each of the sensors exhibited a response of similar shape, but of different magnitudes in the measured strain range.

The primary problem of the sensor was a lack of comparable response.

Recommendations to avoid and isolate this problem are to form a thicker oxide during wafer oxidation. The beam substrate could be prepared using blanchard grinding or milling techniques to ensure variations did not exist on the surface. The bottom of the sensor could also be visually observed to determine if the glass pads were in plane with each other. Otherwise, calibration data may need to accompany each device.

The lack of capacitance change was an additional problem. This can be addressed by modifying the design to incorporate more interdigitated fingers and changing the surface area by increasing the vertical height of each finger. This would deliver a higher initial capacitance and a larger capacitance differential throughout the strain range. Finally, the type of bending strain, tensile or compressive, needs to be identified by the sensor. Intentionally offsetting the fingers will develop spacing between the fingers that will identify the type of strain depending upon capacitance values.

5.0 REFERENCES

- [1] DePuy Gets First-Mover Advantage in Artificial Disk Market
November/December 2004, MX Business Strategies for Medical Technology
Executives. Canon Communications, LLC. Los Angeles
- [2] Hanley, E. N. Jr., David, S. M. Lumbar Arthrodesis for the Treatment of Back
Pain. *Journal of Bone and Joint Surgery*. 1999. 81-A(5). 716-730.
- [3] <http://www.castleortho.com/group/back/fusion.gif>
- [4] <http://www.spineuniverse.com/displayarticle.php/article1551.html>
- [5] Gibson, H., Measurement and Finite Element Modeling of Spinal Rod Strain.
M.Eng. Thesis. University of Louisville. 2002.
- [6] Kanayama, M., Cunningham, B.W., Weis, J.C., Parker, L.M., Kanoda, K., and
McAfee, P.C. Maturation of the posterolateral fusion and its effect on load-
sharing of spinal instrumentation. *Journal Bone and Joint Surgery Am*. 1997.
79 (11). 1710-1720.
- [7] Zogbi, S.W., Canady, L.D., Honeyager, K.S., Helffrich, J.A. Development of a
Diagnostic Method for Spinal Fusion. Southwest Research Institute. 2001.
- [8] <http://www.swri.edu/3pubs/IRD2001/10-9177.htm>
- [9] Rohlmann, A., Bergmann, G., and Graichen, F. A spinal fixation device for in
vivo load measurement. *Journal of Biomechanics*. 1994. 27 (7). 961-967.
- [10] Rohlmann, A., Riley, L.H., Bergmann, G., Graichen, F. In vitro load
measurement using an instrumented spinal fixation device. *Medical Engineering
& Physics*. 1996. 18 (6). 485-488.
- [11] Rohlmann, A., Bergmann, G., Graichen, F., Mayer, H. Telemeterized load
measurement using instrumented spinal internal fixators in a patient with
degenerative instability. *Spine*. 1995. 20, 2683-2689
- [12] Rohlmann, A., Bergmann, G., Graichen, F., Loads on an internal spinal fixation
device during walking. *Journal of Biomechanics*. 1997. 30 (1). 41-47.

- [13] Rohlmann, A., Graichen, F., Weber, U., Bergmann, G., Monitoring in vivo implant loads with a telemeterized internal spinal fixation device. *Spine*. 2000. 25 (23). 2981-2986.
- [14] Rohlmann, A., Bergmann, G., Graichen, F., Weber, U., Comparison of loads on internal spatial fixation devices measured in vitro and in vivo. *Med. Eng. Phys.* 1997. 19 (6). 539-46.
- [15] Graichen, F., Bergmann, G., and Rohlmann, A. 1996. Patient monitoring system for load measurement with spinal fixation devices. *Med. Eng. Phys.*, 18(2). 167-174.
- [16] Graichen, F., Bergmann, G., Rohlmann, A., Dual 8 channel telemetry system for in vivo load measurements with two instrumented implants. *Implantable Telemetry in Orthopaedics*, 1990. 153–162.
- [17] Calisse, J., Rohlmann, A., Bergmann, G., 1999. Estimation of trunk muscle forces using the finite element method and in vivo loads measured by telemeterized internal spine fixation devices. *Journal of Biomechanics*. 32. 727-731.
- [18] Vamvanij, V., Fredrickson, B.E., Thorpe, J.M., Stadnick, M.E, and Yuan, H.A. Surgical treatment of internal disc disruption: an outcome study of four fusion techniques. *Journal of Spinal Disorders*. 1998. 11 (5). 375-382.
- [19] Lee, S., Harris, K., Nassif, J., Goel, V., and Clark, C., In vivo kinematics of the cervical spine. Part I: Development of a roentgen stereophotogrammetric technique using metallic markers and assessment of its accuracy. *Journal of Spinal Disorders*. 1993. 6. 522-534.
- [20] Harris, K.G., Lee, S.J., Goel, V.K., and Clark, C.R., Spinal motion following cervical fusion – in vivo assessment with roentgen stereophotogrammetry. *Spine*. 1994. 19. 2336-2342.
- [21] Perusek, Gail P., Davis, Brian L., Sferra, James J., Courtney, Amy C., D’Andrea, Susan E. An extensometer for global measurement of bone strain suitable for use in vivo in humans. *Journal of Biomechanics*. 2001. 34. 385-391.
- [22] Ledet, E. H., Tymeson, M. P., DiRisio, D. J., Cohen, B., Uhl, R., 2005, Direct real-time measurement of in vivo forces in the lumbar spine. *The Spine Journal*. 2005. 5. 85-94.
- [23] Ledet, E., Sachs, B., Brunski, J., Gatto, C., Donzelli, P., Real time in vivo loading in the lumbar spine. Part 1: interbody implant load cell design and preliminary data. *Spine*. 2000. 25 (20). 2595-2600.

- [24] Taylor, S., Walker, P., Forces and moments telemetered from two distal femoral replacements during various activities. *Journal of Biomechanics*. 2001. 34. 839-848.
- [25] Taylor, S., Perry, J., Meswania, J., Donaldson, N., Cannon, S., Walker, P., Telemetry of forces from proximal femoral replacements and relevance to fixation. *Journal of Biomechanics*. 1997. 30 (3). 225-234
- [26] Taylor, S., Walker, P., Perry, J., Cannon, S. The forces in the distal femur and the knee during walking and other activities measured by telemetry. *Journal of Arthroplasty*. 1998. 13 (4). 428-437.
- [27] Swafford, R., Joseph, H., Vaganov, V. Implementing MEMS Technology in Today's Medical Electronics. *Medical Electronics Manufacturing*. 1997. Fall. 24.
- [28] Loeb, G., Peck, R., Morre, W., Hood, K., BION™ system for distributed neural prosthetic. *Medical Engineering & Physics*. 2001. 23 (1). 9-18.
- [29] D'Lima, D., Townsend, P., Ars, S., Morris, B., Colwell, C., An implantable telemetry device to measure intra-articular tibial forces. *Journal of Biomechanics*. 2005. 38 (2). 299-304.
- [30] Cosofret, V., Erdosy, M., Johnson, T., Bellinger, D., Buck, R., Ash, R., Neuman, M., Electroanalytical and surface characterization of encapsulated implantable membrane planar microsensors. *Analytica Chimica Acta*. 1995. 314. 1-11.
- [31] Ko, W., Implantable sensors for Closed-Loop Prosthetic Systems. Futura Publ. Mount Kisco, NY. 1985. 259-304.
- [32] Morissey, A., Alderman, J., Kelly, G., Kohári, Zs., Páhi, A., Rencz, M., Packaging and thermal evaluation of thermally operated intelligent micropump unit. *Microelectronics Journal*. 1999. 30. 1109-1114.
- [33] Dowling, R., Gray, L., Etoch, S., Laks, H., Marelli, D., Samuels, L., Entwistle, J., Couper, G., Vlahakes, G., Frazier, O. Initial experience with the AbioCor implantable replacement heart system. *Journal of Thoracic and Cardiovascular Surgery*. 2004. 127 (1). 131-141.
- [34] http://www.piresearch.com/sub_page.cfm/section/products/editID/29
- [35] Black, J., *Orthopaedic Biomaterials In Research And Practice*. Churchill Livingstone. New York. 1988. 136.
- [36] Ratner, Buddy D., Hoffman, Allan S., Schoen, Frederick J., Lemons, Jack E., *Biomaterials Science: An Introduction to Materials in Medicine*. Academic Press. San Diego. 1996. 57.

- [37] Greco, R.S., *Implantation Biology, The Host Response and Biomedical Devices*. CRC Press. Boca Raton. 1994. 169-170.
- [38] Khorasani, M., Zaghiyan, M., Mirzadeh, H., Ultra high molecular weight polyethylene and polydimethylsiloxane blend as acetabular cup material. *Colloids and Surfaces B: Biointerfaces*. 2005. 41 (2-3). 169-174.
- [39] Bergström, J., Rimnac, C., Kurtz, S., An augmented hybrid constitutive model for simulation of unloading and cyclic loading behavior of conventional and highly crosslinked UHMWPE. *Biomaterials*. 2004. 25 (11). 2171-2178.
- [40] Edidin, A., Kurtz, S., Influence of mechanical behavior on the wear of 4 clinically relevant polymeric biomaterials in a hip simulator. *The Journal of Arthroplasty*. 2000. 15 (3). 321-331.
- [41] Kurtz, S., Muratoglu, O., Evans, M., Edidin, A., Advances in the processing, sterilization, and crosslinking of ultra-high molecular weight polyethylene for total joint arthroplasty. *Biomaterials*. 1999. 20 (18). 1659-1688.
- [42] Abu Bakar, M., Cheng, M., Tang, S., Yu, S., Liao, K., Tan, C., Khor, K., Cheang, P., Tensile properties, tension–tension fatigue and biological response of polyetheretherketone–hydroxyapatite composites for load-bearing orthopedic implants. *Biomaterials*. 2003. 24 (13), 2245-2250.
- [43] Eschbach, L., Nonresorbable polymers in bone surgery. *Injury*. 2000. 31 (4). D22-D27.
- [44] Morrison, C., Macnair, R., MacDonald, C., Wykman, A., Goldie, I., Grant, M., In vitro biocompatibility testing of polymers for orthopaedic implants using cultured fibroblasts and osteoblasts. *Biomaterials*. 1995. 16 (13). 987-992.
- [45] Abu Bakar, M., Cheang, P., Khor, K., Tensile properties and microstructural analysis of spheroidized hydroxyapatite–poly (etheretherketone) biocomposites *Materials Science and Engineering A*. 2003. 345 (1-2). 55-63.
- [46] Affatato, S., Bordini, B., Fagnano, C., Taddei, P., Tinti, A., Toni, A., Effects of the sterilisation method on the wear of UHMWPE acetabular cups tested in a hip joint simulator. *Biomaterials*. 2002. 23 (6). 1439-1446.
- [47] Lewis, G., Properties of crosslinked ultra-high-molecular-weight polyethylene. *Biomaterials*. 2001. 22 (4). 371-401.
- [48] Kotzar, G., Freas, M., Abel, P., Fleischman, A., Roy, S., Zorman, C., Moran, J., Melzak, J., Evaluation of MEMS materials of construction for implantable medical devices. *Biomaterials*. 2002. 23 (13). 2737-2750.

- [49] Lamba, N.M.K., Woodhouse, K.A., Cooper, S.L., Polyurethanes in Biomedical Applications. CRC Press. Boca Raton. 1998. 2, 38.
- [50] <http://www.invibio.com/products/peekOptima/default.aspx>
- [51] <http://www.invibio.com/products/peekOptima/applications.aspx>
- [52] Smith, S.W., The Scientist and Engineer's Guide to Digital Signal Processing. California Technical Publishing. San Diego. 1997. 40.
- [53] <http://www.memsnet.org/mems/what-is.html>
- [54] Chatzandroulis, Stavros, et. al. A Miniature Pressure System with a Capacitive Sensor and Passive Telemetry Link for Use in Implantable Applications. Journal of Microelectromechanical Systems. 2000. 9 (1). 18-23.
- [55] Huang, Q., Oberle, M., A 0.5-mW Passive Telemetry IC for Biomedical Applications. IEEE J. Solid State Circuits. 1998. 33 (7). 937-946.
- [56] Schnakenberg, U., Krüger, C., Pfeffer, J., Mokwa, vom Bögel, G., Günther, R., Schmitz-Rode, T., Intravascular pressure monitoring system, Sensors & Actuators A, Physical. 2004. 110. 61-67.
- [57] Akin, T., Najafi, K., Bradley, R., A Wireless Implantable Multichannel Digital Neural Recording System for a Micromachined Sieve Electrode, IEEE J. Solid State Circuits 33. 1998. 1. 109-118.
- [58] Coosemans, J., Catrysse, M., Puers, R., A readout circuit for an intra-ocular pressure sensor, Sensors & Actuators A, Physical. 2004. 110. 432-438.
- [59] Swafford, R., Joseph, H., Vaganov, V., Implementing MEMS Technology in Today's Medical Electronics. Medical Electronics Manufacturing. Fall 1997.
- [60] Teymoori, M., Abbaspour-Sani, E., Design and simulation of a novel electrostatic peristaltic micromachined pump for drug delivery applications Sensors and Actuators A: Physical. 2005. 117 (2). 222-229.
- [61] Yeow, J., Yang, V., Chahwan, A., Gordon, M., Qi, B., Vitkin, I., Wilson, B., Goldenberg, A., Micromachined 2-D scanner for 3-D optical coherence tomography. Sensors and Actuators A: Physical. 2005. 117 (2). 331-340.
- [62] Thielicke, E., Obermeier, E., Microactuators and their technologies. Mechatronics. 2000. 10 (4-5). 431-455.
- [63] Xie, H., Fedder, G., Vertical comb-finger capacitive actuation and sensing for CMOS-MEMS, Sensors & Actuators A, Physical. 2002. 95. 212-221.

- [64] Xiao, Z., Peng, W., Wolffenbuttel, W.F., Farmer, K.R., Micromachined variable capacitors with wide tuning range, *Sensors & Actuators A, Physical*. 2003. 104. 299-305.
- [65] Sun, Y., Piyabongkarn, D., Sezen, A., Nelson, B.J., Rajamani, R., A high aspect ratio two-axis electrostatic microactuator with extended travel range, *Sensors & Actuators A, Physical*. 2002. 102. 49-60.
- [66] Xie, H., Pan, Y., Fedder, G., A CMOS-MEMS Mirror With Curled-Hinge Comb Drives, *J. Microelectromechanical Systems*. 2003. 12 (4). 450-457.
- [67] Nguyen, H., Hah, D., Patterson, P., Chao, R., Piyawattanametha, W., Lau, E., Wu, M.C., Angular Vertical Comb-Driven Tunable Capacitor With High-Tuning Capabilities, *J. Microelectromechanical Systems*. 2004. 13 (3). 406-413.
- [68] Garcia, E., Sniegowski, J., Surface micromachined microengine, *Sensors & Actuators A, Physical*. 1995. 48. 203-214.
- [69] Huang, C., Christophorou, C., Najafi, K., Naguib, A., Nagib, H., An Electrostatic Microactuator System for Application in High-Speed Jets. *Journal of Microelectromechanical Systems*. 2002. 11 (3). 222-235.
- [70] Wang, Z.F., Cao, W., Shan, X.C., Xu, J.F., Lim, S.P., Noell, W., de Rooij, N.F., Development of a 1 x 4 MEMS-based optical switch. *Sensors & Actuators A, Physical*. 2004. 114 (1). 80-87.
- [71] Rajendran, S., Liew, K., Design and simulation of an angular-rate vibrating microgyroscope. *Sensors and Actuators A, Physical*. 2004. 116 (2). 241-256.
- [72] Chu, L., Que, L., Gianchandani, Y., Measurements of Material Properties Using Differential Capacitive Strain Sensors, *Journal of Microelectromechanical Systems*. 2002. 11 (5). 489-498.
- [73] Chengkuo, L., Design and fabrication of epitaxial silicon micromirror devices. *Sensors and Actuators A, Physical*. 2004. 115 (2-3). 581-590.
- [74] Tilleman, M., Analysis of electrostatic comb-driven actuators in linear and nonlinear regions. *International Journal of Solids and Structures*. 2004. 41 (18-19). 4889-4898.
- [75] Huang, W., Lu, G., Analysis of lateral instability of in-plane comb drive MEMS actuators based on a two-dimensional model. *Sensors and Actuators A: Physical*. 2004, 113 (15). 78-85.
- [76] Chen, C., Kuo, W., Squeeze and viscous dampings in micro electrostatic comb drives. *Sensors and Actuators A: Physical*. 2003. 107 (2). 193-203.

- [77] Higdon, A., Ohlsen, E.H., Stiles, W.B., Weese, J.A., Riley, W.F. Mechanics of Materials, Fourth Edition. John Wiley & Sons. 1985. 488.
- [78] Hsu, Tai-Ran. MEMS & MICROSYSTEMS: Design and Manufacture. McGraw-Hill. New York. 2002. 246.
- [79] Kovacs, Gregory T. A., Micromachined Transducers Sourcebook. McGraw-Hill, New York. 1998. 219-220.
- [80] Lin, Liwei, et. al. A Micro Strain Gauge with Mechanical Amplifier. Journal of Microelectromechanical Systems. 1997. 6 (4). 313-322.
- [81] Jaeger, R.C., Introduction To Microelectronic Fabrication, Second Edition, Prentice Hall, Upper Saddle River, New Jersey, 2002, 153.
- [82] Madou, M.J., Fundamentals of Microfabrication – The Science of Miniaturization, 2nd Edition, CRC Press, Boca Raton, Florida. 2002. 104, 198-200.
- [83] Avallone, E.A., Baumeister III, T., Marks' Standard Handbook for Mechanical Engineers, Tenth Edition. McGraw-Hill. New York. 13-67.
- [84] <http://www.dow.com/webapps/lit/litorder.asp?filepath=engineeringplastics/pdfs/noreg/301-02702.pdf&pdf=true>

6.0 CURRICULUM VITAE

NAME: Julia Marie Weyer Aebersold

ADDRESS: Department of Mechanical Engineering
Sackett Hall
Speed School of Engineering
University of Louisville
Belknap Campus
Louisville, KY 40292

DOB: Jasper, Indiana – February 6, 1969

EDUCATION

& TRAINING: B.S.E.S., Mechanical Engineering
University of Louisville
1987-92

M. Eng., Mechanical Engineering
University of Louisville
1992-94

NATIONAL MEETING PRESENTATIONS

Development of a long term implantable sensor housing for a telemetric strain monitoring system to assist the detection of spinal lumbar arthrodesis, Orthopaedic Research Society, 5th Combined Meeting of Canada, USA, Japan and Europe, Banff, Alberta, Canada, October 10-13, 2004

INVITED PRESENTATIONS:

Design and Development of a MEMS-based Capacitive Bending Strain Sensor,
Research! Louisville, Louisville, Kentucky, November 8-12, 2004.